Synthesis, Characterisation and Antifungal Activity of Copper(II)-Functionalised Silicone Polymers and Silicone-Coated Magnetic Nanoparticles

A thesis presented to the National University of Ireland

for the award of

Master of Science

Collette Regina Reynolds B.Sc.

Department of Chemistry,
Maynooth University,
Maynooth,
Co Kildare.

Research Supervisors: Dr. Malachy McCann, Dr. John McGinley

Head of Department: Dr. John Stephens

August 2015

Contents

CHAPTER 2: Experimental

Declaration

This thesis has not been submitted in part or in full to any other University or College and is, except where otherwise stated, the original work of the author.

_____

Collette Reynolds

Acknowledgements

I wish to thank my supervisors Dr. Malachy McCann and Dr. John McGinley for taking me on and giving me the opportunity to do this work. I am very grateful to you both for your help and guidance. Thank you to Dr. John C. Stephens for allowing me to carry out this research at Maynooth University. Many thanks to Dr. Kevin Kavanagh for allowing me use the facilities in the Medical Mycology Laboratory. I am also grateful to all the academic staff in the Chemistry Department.

Thanks to Ollie, Barbra, Ria and Maryanne R. for all the technical support. Noel, genius of the department, from mechanical stirrers and magnets, to helicopters and computers; no job was too big or too small, thank you for your help, and thanks also for keeping my old laptop going. Maryanne Dalton, thanks for all your encouragement and help throughout undergrad and post-grad. Donna, Carol and Niamh thank you for all your help on many occasions.

Thank you to everybody in the Synthesis Laboratory, and all the postgrads and postdocs from whom I have learned so much, especially Trish demonstrator extraordinaire, and Laura, thanks for all you've done for me. Niamh and Niall M., thank you for all your help with all my questions. Alice, thank you for all the gifts you gave my children through the years, they have enjoyed them very much. Also, Michelle D., your help and kindness are much appreciated, my children and I thank you. Ula, thank you for taking time to keep in touch, I appreciate it and I am grateful to you. Keeley and Andy, thanks for helping me format this document. Justine, thanks for running NMRs and Andrew, thanks for all the IR help. Saidhbhe, thanks for taking the time to listen, and David, thanks for taking time to help me with TEM. Karen, thanks for the many times you have helped me out. Susan, Barry, Ross and Chiggy thanks for the banter in the write-up room, and the proof-reading ☺. Muhib, I wish you the best of luck with your studies, I hope all your research goes really well for you, and if I ever run out of phendione I will give you a shout. To the visitors we have

had in our group, Amanda K., Livia, Amandine, Amada D., Michelle K. and Stephen it was a pleasure working with you all. I wish you guys all the best for the future.

Gráinne Roche, your encouragement and help are much appreciated. Louise Geraghty and Michael, thanks for all the tea and sympathy, I'll still call for tea, and hopefully I won't need the sympathy any more. Thanks also to Dr Angela Rickard for your comments and advice.

Mary Mc., Carina, Sinéad, and Bernie O'R., thank you for always being there to take care of my children, and sometimes to take care of me too, I am grateful to you all for your help and understanding and also for the many lovely dinners. It's my turn to cook now, I should have some time now that this *magnum opus* is out of the way! Fiona, I wish you the best of luck in your studies, you will make a fantastic paediatric nurse. Marina, your amazing gifts have sustained me on many occasions. I appreciate you, and I thank you. Pamela, for all the times you took my girls for a week during school holidays to allow me study and revise, and for everything else you do, you are fantastic, thank you. Dr. Ciara Crawford, for your understanding and encouragement, you are an inspiration. Yvonne and Brenda thanks for always being there for me and for all your support and for being such good listeners.

Valerie Kenny C.P.A., I know it was tough but we finally did it! I could not have continued without your help. Words simply cannot express my gratitude. I thank you for everything you have done.

So many people have helped and supported me since I began studying, I hope I have not left anyone out. There were many occasions when it would have been easy to give up, however, the support and encouragement I received from my many friends made it impossible to turn back. I am grateful to you all. I promise to never mention nanoparticles again. Ever!

Finally, my three beautiful daughters, I am so proud of you. Through every step of this journey you have been wonderful and have shown wisdom beyond your years. Thank you for everything. You are my joy.

For my daughters

JoJo, Ailíse and Caoimhe.

Abstract

Two families of amine-functionalised silicone polymers were prepared using monomeric (3-aminopropyl)triethoxysilane (APTES) and (3-trimethoxysilylpropyl)diethylene triamine (TMSPDT). Schiff base derivatives of these polymers were synthesised using salicylaldehyde. The same suite of polymers were also formed as a surface coating on magnetite nanoparticles (Fe_3O_4-MNPs). Copper(II) ions were coordinated to the pendant amine groups of all of the polymers. *In vitro* tests using the fungal pathogen, *Candida albicans*, revealed that the silicone polymers, their Cu(II) complexes and the Schiff base salicylate derivatives inhibited cell growth. None of the silicone-coated Fe_3O_4-MNPs were bioactive.

Abbreviations

AFM	Atomic force microscopy
AgNPs	Silver nanoparticles
AIDS	Acquired immune deficiency syndrome
APTES	(3-aminopropyl)triethoxysilane mw = 221.37 g/mol; Density = 0.946 g/cm^3
bipy	2,2′-bipyridine
BBB	Blood-brain barrier
C. albicans	*Candida albicans*
CD	Cyclodextrin
CHN	Carbon, hydrogen and nitrogen
°C	Degrees Celsius
[Cu-Sal-pAPTES-Fe_3O_4-MNPs]	Fe_3O_4 magnetic nanoparticles modified with polymerised (3-aminopropyl)triethoxysilane, salicylaldeyde, and copper.
[Cu-Sal-pTMSPDT-Fe_3O_4-MNPs]	Fe_3O_4 magnetic nanoparticles modified with polymerised (3-trimethoxysilylpropyl) diethylene-triamine, salicylaldeyde, and copper
DCM	Dicholoromethane
DMF	Dimethylformamide
DMSO	Dimethylsulfoxide
DNA	Deoxyribonucleic acid
EDX	Energy dispersive x-ray
EtOH	Ethanol
FCC	Face-centred cubic
Fe_3O_4-MNPs	Magnetite magnetic nanoparticles
g	Gravitational constant
h	Hour/hours
HIV	Human immunodeficiency virus
Hz	Hertz
IR	Infra-red
IUPAC	International Union of Pure and Applied Chemistry
J	Coupling constant
KBr	Potassium bromide
MeOH	Methanol
min	minutes
mmoles	millimoles
MNPs	Magnetic nanoparticles
MRI	Magnetic resonance imaging
[$(NO_3)_2$Cu-pAPTES]	Copper(II) coordinated to polymerised (3-aminopropyl)triethoxysilane)

$[(NO_3)_2Cu\text{-}pTMSPDT]$	Copper(II) coordinated to polymerised (3-trimethoxysilylproply)diethylene triamine)
NMR	Nuclear magnetic resonance
NMR multiplicity	t = triplet m = multiplet
NPs	nanoparticles
$[(OAc)_2Cu\text{-}pAPTES\text{-}Fe_3O_4\text{-}MNPs]$	Copper(II) coordinated to polymerised (3-aminopropyl)triethoxysilane) modified magnetite magnetic nanoparticles
$[(OAc)_2Cu\text{-}pTMSPDT\text{-}Fe_3O_4\text{-}MNPs]$	Copper(II) coordinated to polymerised modified (3-trimethoxysilylproply)diethylene triamine) magnetite magnetic nanoparticles
pAPTES	Polymerised (3-aminopropyl)triethoxysilane)
$pAPTES\text{-}Fe_3O_4\text{-}MNPs$	Polymerised (3-aminopropyl)triethoxysilane Modified magnetite magnetic nanoparticles
phen	1,10-phenanthroline
$pTMSPDT\text{-}Fe_3O_4\text{-}MNPs$	Polymerised (3-trimethoxysilylpropyl)diethylene triamine modified Fe_3O_4 magnetic nanoparticles
pKa	Acid dissociation constant
ppm	Parts per million
pTMSPDT	Polymerised (3-trimethoxysilylproply)diethylene triamine)
rl	Lattice relaxivity
RNA	Ribonucleic acid
ROS	Reactive oxygen species
RPM	Revolutions per minute
SAED	Selected Area Electron Diffraction
Sal	Deprotonated salicylaldehyde
SalH	Salicylaldehyde mw = 122.12 g/mol; Density = 1.15 g/cm^3
SalH-pAPTES	Polymerised (3-aminopropyl)triethoxysilane modified with salicylaldehyde
$SalH\text{-}pAPTES\text{-}Fe_3O_4\text{-}MNPs$	Magnetite magnetic nanoparticles modified with polymerised (3-aminopropyl)triethoxysilane) and saliclyaldehyde
SalH-pTMSPDT	Polymerised (3-trimethoxysilylpropyl)diethylene triamine modified with salicylaldehyde
$SalH\text{-}pTMSPDT\text{-}Fe_3O_4\text{-}MNPs$	Magnetite magnetic nanoparticles modified with polymerised (3-trimethoxysilylpropyl)diethylene triamine and saliclyaldehyde
SEM	Scanning electron microscopy

STM	Scanning tunnelling microscopy
TEM	Transmission electron microscopy
TMSPDT	(3-trimethoxysilylpropyl)diethylene triamine mw = 265.43 g/mol; Density = 1.03 g/cm^3
VTMS	Vinyltrimethoxysilane
v/v	Volume per volume
YEPD	Yeast extract peptone dextrose

Chapter 1

Project Aims

and

Introduction

1.1 Project Aims

The central aims of this project were (i) to synthesise and characterise water-insoluble, functionalised silicone polymers and silicone-coated magnetic nanoparticles (MNPs), with each having bioactive copper(II) ions anchored to their outer surface and, (ii) to assess the ability of these metal-complexed polymeric materials to inhibit the growth of a fungal pathogen through the slow, sustained release of the bio-destructive copper(II) ion. It is envisaged that such polymeric materials could be added to a medium containing actively growing microbial cells, perform their fungistatic/fungicidal duty, be recovered (by filtration or using a magnet) from the medium and be recycled. Such materials could find utility in drug delivery, personal care compositions, surface cleaners, swimming pool water disinfection systems, etc. Additionally, the bioactive polymers could be blended into paints and other solid surface polymer materials to provide a dynamic barrier to microbial growth.

Introduction

This Introduction section is configured to give the reader a general overview of functionalised silicone polymers, nanoparticles and the problems associated with microbial pathogens. Particular attention is given to the fungal species, *Candida albicans*, as this was the test organism used in the current study. The antimicrobial activity of the copper(II) ion is reviewed as this was the metal ion employed in the present work.

1.2 Polysiloxanes

1.2.1 Polysiloxanes

Polysiloxanes are inorganic polymers which contain a repeating backbone unit of O-Si-O bonds. In the medicinal context, polysiloxanes have been successfully utilised in short-term and long-term in-dwelling catheters, drains, shunts and contact lenses[1]. Two examples of these polymers that are used in a medicinal context are shown in Figure 1.

(a)

(b)

Figure 1. Examples of polysiloxanes used for medicinal purposes: (a) irrigation catheter[2] and (b) silicone gel-sheet for scar/burn treatment[3].

The siloxane linkage (Si-O-Si) in the backbone is characteristic of most silicone polymers. Whilst polysilanes have Si-Si bonds and polycarbosilanes contain Si-C linkages, neither have the siloxane linkage[4].

Although silicon is immediately below carbon in Group 14 of the Periodic Table, the elements exhibit very different chemical properties. Carbon and silicon both have a

normal oxidation state of 4, but silicon can expand its valence shell by using low-lying 3*d* orbitals for bonding[5]. Silanes are less stable than their alkane counterparts due to the fact that the Si-Si bond energy is considerably weaker (*ca.* 170 kJ mol^{-1}) than that of the C-C bond[5]. However, Si-O bonds are noticeably stronger (*ca.* 88 kJ mol^{-1}) than C-O bonds. The Si-O bond distance (1.64 Å) is shorter than the sum of the covalent radii (1.76 Å), implying a partial double bond character in the Si-O bond[6]. The double bond character is also due to the partial overlap of the empty, low energy Si 3*d* orbitals with the populated *p* orbitals of oxygen. The large electronegativity differences between silicon and oxygen atoms (1.8 and 3.5, respectively) causes partial ionic character[6]. The large bond angles (140-180°) in the Si-O-Si backbone allows for a high degree of flexibility, in contrast to the tighter angles in vinyl polymers and polyethers[5]. It is this flexibility of the polysiloxanes which imparts the characteristic low glass-transition temperature, melting temperatures and liquid crystalline behaviours[6]. The high thermal stability of the polysiloxanes is due to the inherent strength of the Si-O bond and the flexibility of the O-Si-O segments of the whole polymer.

The silicon atom in a polyorganosiloxane can be bonded to one, two or three organic groups, with oxygen in the remaining valencies. M, D, T and Q shorthand notations are used to indicate mono-, di-, tri- and quaternary-functionality, respectively[7] (Table 1). Depending on monomer composition, polysiloxanes can have linear, branched or cross-linked structures.

Table 1. Polyorganosilane structural units.

Structural composition	Formula	Functionality	Symbol
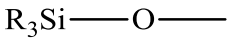	$R_3SiO_{1/2}$	Monofunctional	M
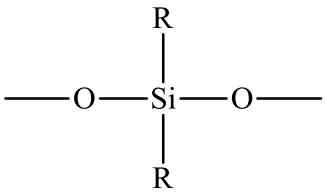	$R_2SiO_{2/2}$	Difunctional	D
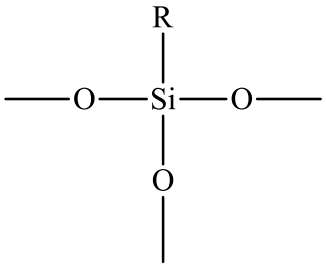	$RSiO_{3/2}$	Trifunctional	T
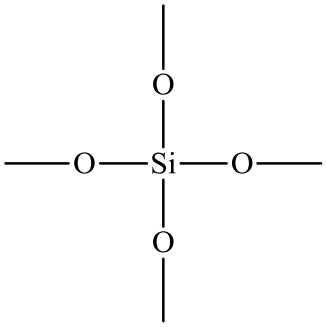	$SiO_{4/2}$	Quatrafunctional	Q

Silicone polymers, having specific physical properties, can be produced by varying the nature of the R substituent, e.g. vinyl, trifluoropropyl, alkyl amines. Such silicones are used as fluids, emulsions, resins and elastomers[8]. Silicones are renowned for their

biocompatibility and biodurability, and both of these features have been attributed to the inherent chemical and thermal stability of the polymers, their low surface tension and hydrophobicity[1]. Polysiloxanes have been shown to be suitable hosts for holding metal nanoparticles and also metal ions[9] and this has been attributed to the unusual freedom of rotation around the Si-O bond which allows the polymers a high degree of flexibility while maintaining their integrity.

The use of polysiloxanes in breast implants was linked to rheumatoid arthritis and other diffuse connective tissue diseases in the 1980s. However, there has been no clear scientific evidence to substantiate the claims[10]. Implants manufactured by the French company, Poly Implant Prothese (PIP), were banned for use in 2010 due to concerns about their safety. It was found that the manufacturers used inferior grade polydimethylsiloxane which did not reach the high standards required for use in medical products[11].

1.2.2 Synthesis of Silicone Polymers

The polymerisation of alkoxysiloxanes (Figure 2) involves a bimolecular nucleophilic substitution reaction (S_N2) in which the alkoxy groups are hydrolysed to give silanols (Si-OH)[12]. Concomitant loss of a water molecule from two silanols leads to the formation of siloxanes (Si-O-Si) in a condensation-dehydration reaction.

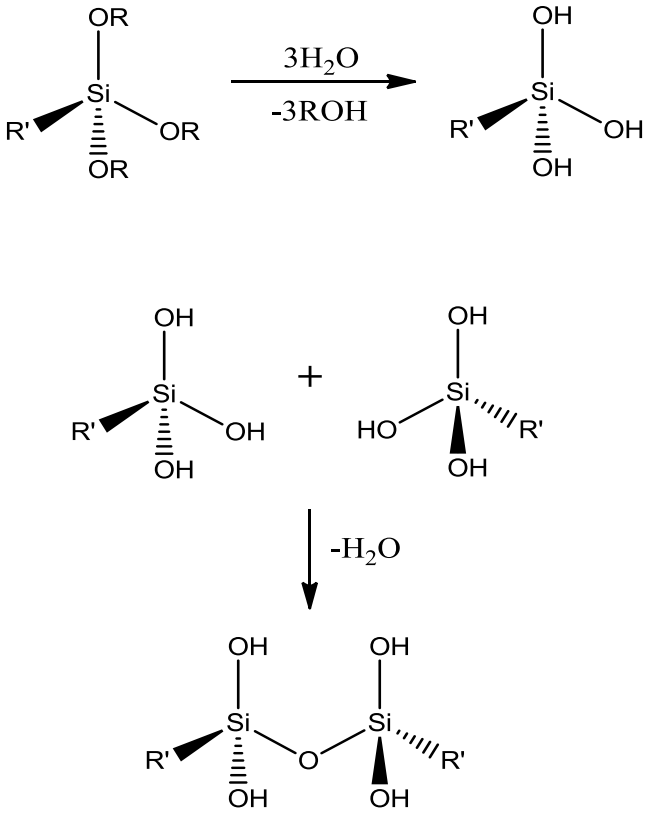

Figure 2. General scheme for the polymerization of a trialkoxysilane (hydrolysis followed by condensation).

The rates of the hydrolysis and condensation reactions are influenced by the organic substituent (R′) on the siloxane monomer, the nature of the alkoxy group, pH, the presence of a catalyst, silane concentration, temperature, inductive effects and steric effects[6] (see equations 1-3 below).

$RSiZ_3 + 3H_2O$	⟶	$RSi(OH)_3 + 3HZ$	hydrolysis	(1)
$3RSi(OH)_3$	⟶	$3RSiO_{3/2} + 4.5H_2O$	condensation	(2)
$RSi(OH)_3 + RSiZ_3$	⟶	$2RSiO_{3/2} + 3HZ$	condensation	(3)

(Z = OR′, Cl, OAc etc.)

Reaction mechanisms for the acid-catalysed and base-catalysed hydrolysis reactions are shown in Figure 3.

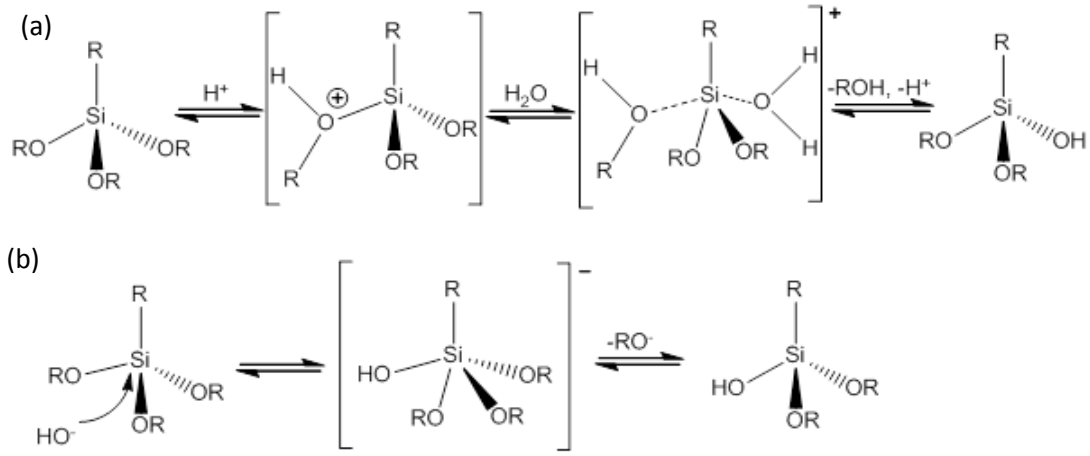

Figure 3. Reaction mechanisms for (a) the acid-catalysed and (b) the base-catalysed hydrolysis reactions of silanes.

The alkoxy groups on the silane monomer influence the rate of hydrolysis. Hydrolysis occurs faster with better leaving groups such as the alkoxy groups (as alcohols). Lower pKa values give better leaving groups and leaving group ability is determined by the pKa value of the conjugate acid (e.g. methanol, ethanol or hydrochloric acid)[13]. The chloride ion is an excellent leaving group because hydrochloric acid, the conjugate acid, has a pKa value of -7. When a chloride ion is liberated as a leaving group during the hydrolysis reaction, the hydrochloric acid formed catalyses the subsequent condensation reaction[14].

The pKa value for methanol is 15.2 whilst ethanol has a pKa value of 15.9. Methanol and ethanol are the conjugate acids for methoxy and ethoxy groups. Studies on methoxy and ethoxy silanes have shown that methoxy groups undergo hydrolysis more readily than their ethoxy homologues[15,16]. For the monomeric (3-aminopropyl)triethoxysilane (mAPTES) and the monomeric 3-trimethoxysilylpropyl)diethylenetriamine (mTMSPDT), the rate of hydrolysis is faster for the longer triamine monomer due to the methoxy groups, however, the rate of the condensation reaction is slower due to the steric hindrance of the bulky triamine chain[16].

Cross-linking of the siloxane monomers and chains affords polymeric structures which have enhanced thermal stability, mechanical properties and solvent resistance[17]. Cross-linking can be accomplished either by direct reaction of the monomers or by promoting covalent cross-linking of preformed polymer chains[6]. Curing can be stimulated using catalysts such as organic bases, carboxylic acids and complexes containing certain *p*-block and transition metal ions[18]. Extended curing, which ensures a high degree of polymer cross-linking, can be achieved by either raising the reaction temperature or through gamma and electron beam irradiation[19,20].

A silsesquioxane is a polymeric silicon structure of the form, $R'SiO_{3/2}$, and has an organic substituent, R´, as an integral component of the network. R´ can be an alkyl or aryl group, with or without saturation, and it can contain functionality, such as

amine or epoxy. A range of silsesquioxane structures are known, such as random structures, oligomeric cage silsesquioxanes with 8-16 silicon atoms, partial cage structures, ordered ladder structures and three dimensional network structures (Figure 4)[21].

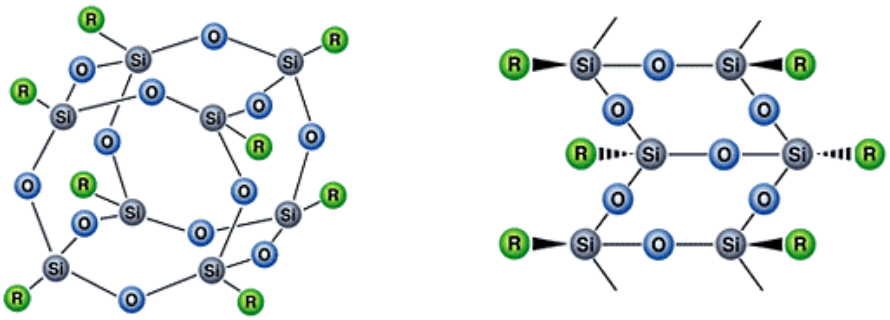

(a) (b)

Figure 4. Structures of (a) a cubic silsesquioxane oligomer, and (b) a ladder-type polymer structure.

1.3 Siloxane Monomers Used in the Present Work

1.3.1 (3-Aminopropyl)triethoxysilane (APTES)

The commercially available (3-aminopropyl)triethoxysilane liquid monomer (mAPTES) comprises a central silicon atom, from which there is attached a propyl chain with a terminal amine group and three ethoxy groups (Figure 5).

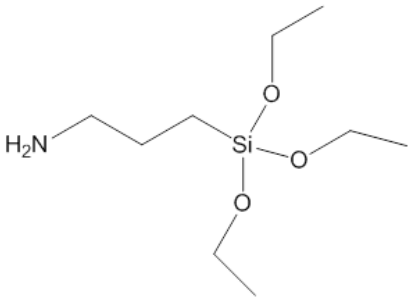

Figure 5. Structure of monomeric APTES (mAPTES).

Conversion of mAPTES to polymeric APTES (pAPTES) occurs by the two-step process of hydrolysis followed by condensation. mAPTES can be polymerised using water and hydrochloric acid[22]. pAPTES is a highly cross-linked silsesquioxane[23], rendering it a stiff material with good thermal resistance[22].

1.3.2 (3-Trimethoxysilylpropyl)diethylene triamine (TMSPDT)

Monomeric (3-trimethoxysilylpropyl)diethylene triamine (mTMSPDT) has a central silicon atom to which is attached a diethylenetriamine side group and three methoxy groups (Figure 6). mTMSPDT is liquid at room temperature and is commercially available.

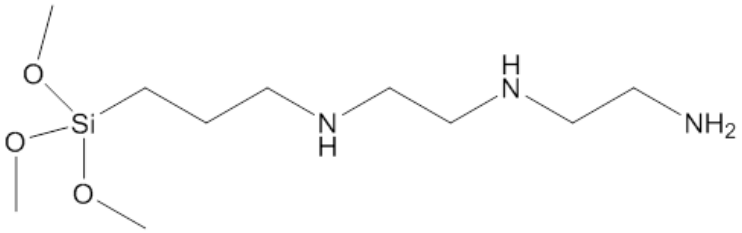

Figure 6. Structure of monomeric TMSPDT (mTMSPDT).

Like the polymerisation of mAPTES, the polymerisation of TMSPDT, to form pTMSPDT, occurs in consecutive hydrolysis and condensation steps. mTMSPDT can be polymerised in water or in an alcohol/water solvent mixture using either acid catalysts, such as acetic acid or hydrochloric acid, or base catalysts, such as *n*-dodecylamine or sodium hydroxide[24-26]. Copolymerisation can be achieved with tetraethoxysilane, tetramethoxysilane, dimethylsilanediol or vinyltrimethoxysilane (VTMS)[27-29].

When polymerised, p(TMSPDT) forms a highly cross-linked silsesquioxane structure. The amine functionality in pTMSPDT allows for the adsorption of heavy metals such as copper(II), nickel(II), cobalt(II) and the dichromate anion, CrO_4^{2-}, from aqueous solutions[26]. Silica powder modified with mTMSPDT, formed using acidic conditions, has been used for the removal of microorganisms such as *Escherichia coli*, MS2 bacteriophage virus, albumin and the protozoan parasite, *Cryptosporidium parvuum,* from water[30]. CO_2 adsorption is another use which utilises the amine functionality of the material[31]. TMSPDT is also a silane coupling agent and is used as a surface modifier and adhesion promoter as it exhibits outstanding adhesion to many inorganic substrates such as glass, metal or fillers[32]. Materials containing TMSPDT show good thermal resistance, however, the long chain polyamines have lower thermal stability than the shorter chain polyamines, such as APTES[31].

1.4 Nanotechnology

1.4.1 Definition and Description

The definition of 'Nano' recommended for use by the EU Commission is: 'Nano consists of natural, incidental or manufactured particles, in an unbound state or as an aggregate or agglomerate with one or more external dimensions in the size range 1-100 nm for more than 50% of their number size distribution'. The IUPAC glossary of terms defines 'nanoparticle' as 'microscopic particle whose size is measured in nanometres, often restricted to so-called nano-sized particles (NSPs: < 100 nm in aerodynamic diameter), also called ultrafine particles'[33]. Nanotechnology is 'the understanding and control of matter at dimensions of roughly 1-100 nm, where unique phenomena enable novel applications' according to the definition of nanotechnology by the United States (US) Nanotechnology Initiative. Although there seems to be no full definition *per se* currently agreed upon by the scientific communities who carry out research in the field of nanotechnology, nanostructures, as the name implies, are structures with at least one dimension in the nanoscale. The prefix 'nano' means one billionth of a metre (1×10^{-9} m).

Due to their size, many of the properties of nanostructures such as fluorescence, melting point, optical properties, band gap energy and chemical reactivity are observed as being different from those of the bulk counterpart[34] (Figure 7). Classical mechanics does not explain the behaviour of nanoscale structures. At the annual meeting of the American Physical Society in December 1959, Professor Richard

Feynman called for improvements to be made to the electron microscope to progress the field. In his address he stated, "...atoms on a small scale behave like nothing on a large scale, for they satisfy the laws of quantum mechanics." At the nanoscale, quantum effects are those observed due, in part, to the large surface-to-volume ratio of nanoparticles[35,36].

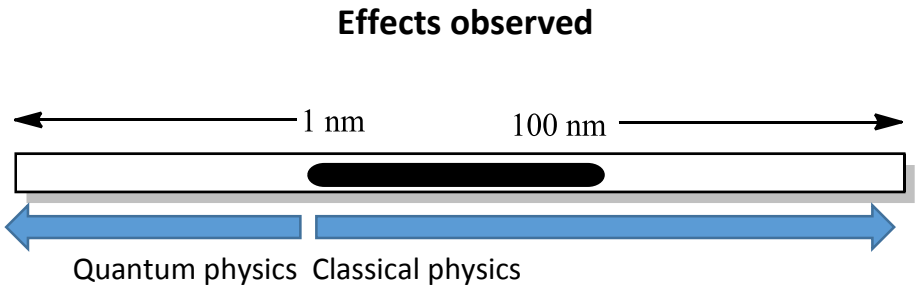

Figure 7. Dimensions in quantum and classical physics.

Nanoscale structures which exist in nature include viruses, which can be <100 nm. The ebola virus is filamentous and up to 970 nm long with a diameter of 80 nm, whilst deoxyribonucleic acid (DNA) is approximately 2.5 nm in diameter (Figure 8). Proteins can be less than 3 nm and individual atoms are less than 1 nm in diameter[35]. A particle which measures a few nanometres may contain as many as 10^5 atoms or as few as a couple of hundred atoms[37,35].

Nanomaterials have a myriad of uses. They are found in items as diverse as cosmetics, clothes, computers, aerospace technology[38] and magnetic tapes[39], and also in recoverable catalyst systems[40].

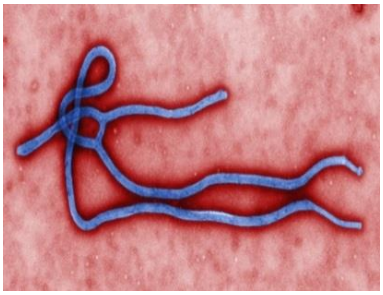

(a)

(b)

Figure 8. Images of nanoscale structures that exist in nature (a) colourised TEM image of ebola virus[41], (b) cartoon image of DNA[42].

Magnetic microspheres, ferrofluids (Figure 9) and nanospheres are used in targeted drug delivery, enzyme immobilization, RNA and DNA purification[43]. Biodegradable nanoparticles are used as magnetic resonance imaging (MRI) contrast agents, drug carriers, and as labelling and tracking agents in biomedical systems[44-46].

Figure 9. Ferrofluid on a magnet[45].

Nanoparticles are colloidal systems possessing unique properties which can be investigated using advanced microscopy, such as atomic force microscopy (AFM), transmission electron microscopy (TEM) and scanning tunnelling microscopy (STM)[35]. The improvement in imaging techniques has progressed the field of

nanotechnology greatly since the invention of TEM in the 1930's, and AFM and STM in the early 1980's. A nanoparticle is comprised of between a few hundred to a few thousand atoms incorporated in the crystal structure and the symmetry of a molecule differs between the surface and the interior[46].

In the context of the present work, Taglietti *et al.*[47] amino-silanized a glass surface using monomeric (3-aminopropyl)triethoxysilane (mAPTES) and subsequently anchored a monolayer of silver nanparticles (AgNPs) to the pendant amine functional groups (Figure 10). This stable material provided a prolonged release and high local concentration of Ag^{+} ions which promoted potent anti-biofilm activity against *Staphylococcus epidermidis* RP62A.

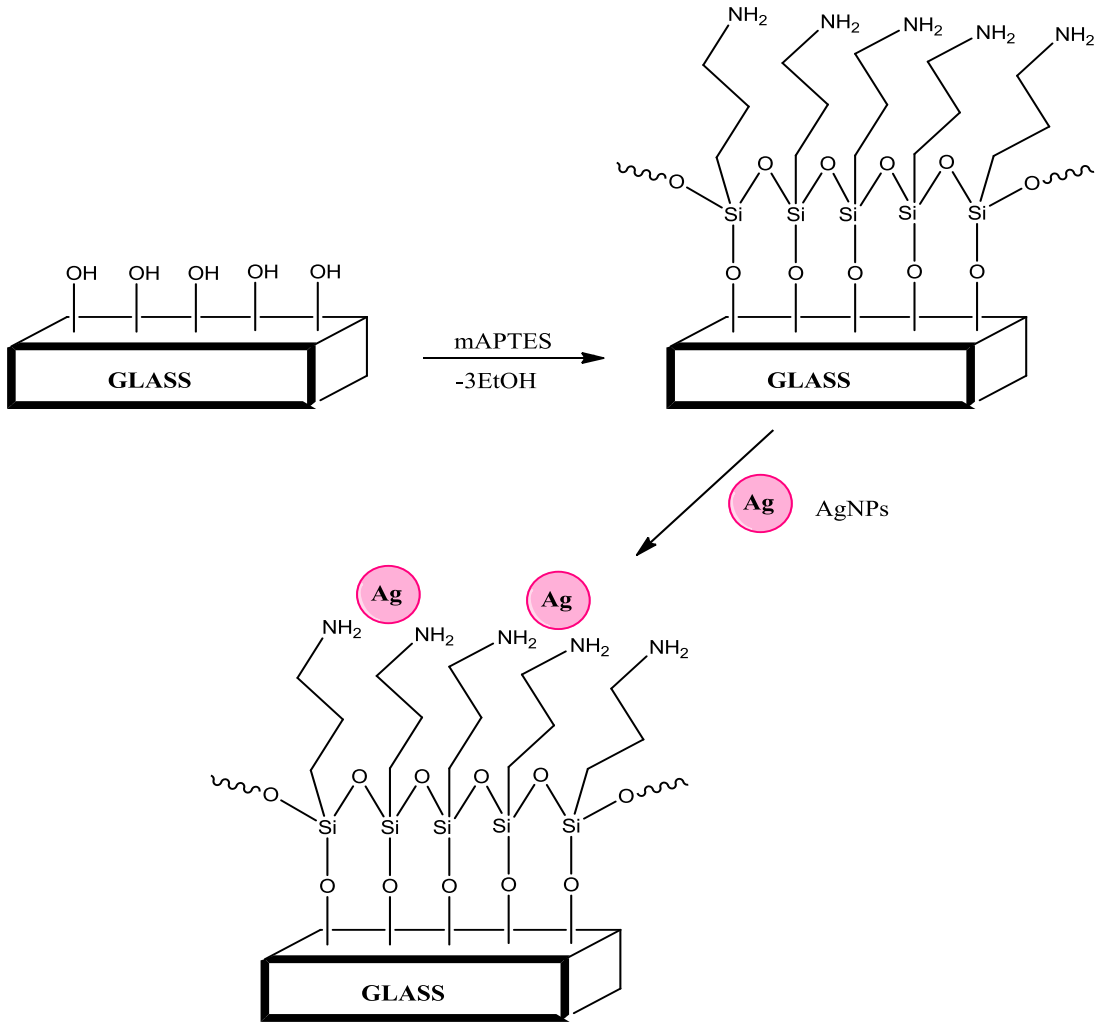

Figure 10. Silanization of glass surface with mAPTES and subsequent anchoring of AgNPs[47].

1.4.2 Iron Oxide Magnetic Nanoparticles (Fe3O4-MNPs)

Magnetite (Fe_3O_4; comprising $Fe^{2+}(Fe^{3+})_2(O^{2-})_4$) has been known since ancient times[48]. Fe_3O_4 magnetic nanoparticles (Fe_3O_4-MNPs) have magnetic properties which differ from those of the bulk material. These properties are due to both their size and the fact that each particle has a large magnetic moment. Fe_3O_4-MNPs are

'superparamagnetic' as they respond to a magnetic field but do not retain residual magnetization[35,49,50].

Saturation of the surface of metal oxides occurs by the reaction of water with the surface metal-oxygen (M-O) bonds. Fe_3O_4-MNPs are insoluble in water[51] and bare atoms of iron and oxygen on the particle surface adsorb hydroxyl ions and protons in solution to give a neutral particle with a hydroxyl-rich surface[46,52] (Figure 11).

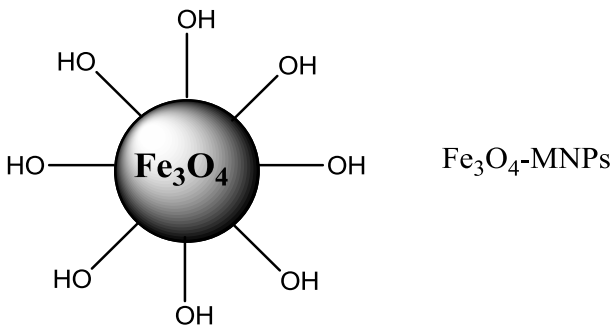

Figure 11. Schematic of the hydroxyl-rich surface of Fe_3O_4-MNPs.

The surface decoration of hydroxyl groups gives rise to columbic repulsion[53] and can be used to covalently anchor silicone polymers, using suitable alkoxy-silane monomers, in a condensation reaction (Figure 12)[47].

The size of MNPs can be tailored by covering them with a number of silicone coats[54]. As the size of the particle decreases, the ratio of the surface area to the volume of the particle increases.

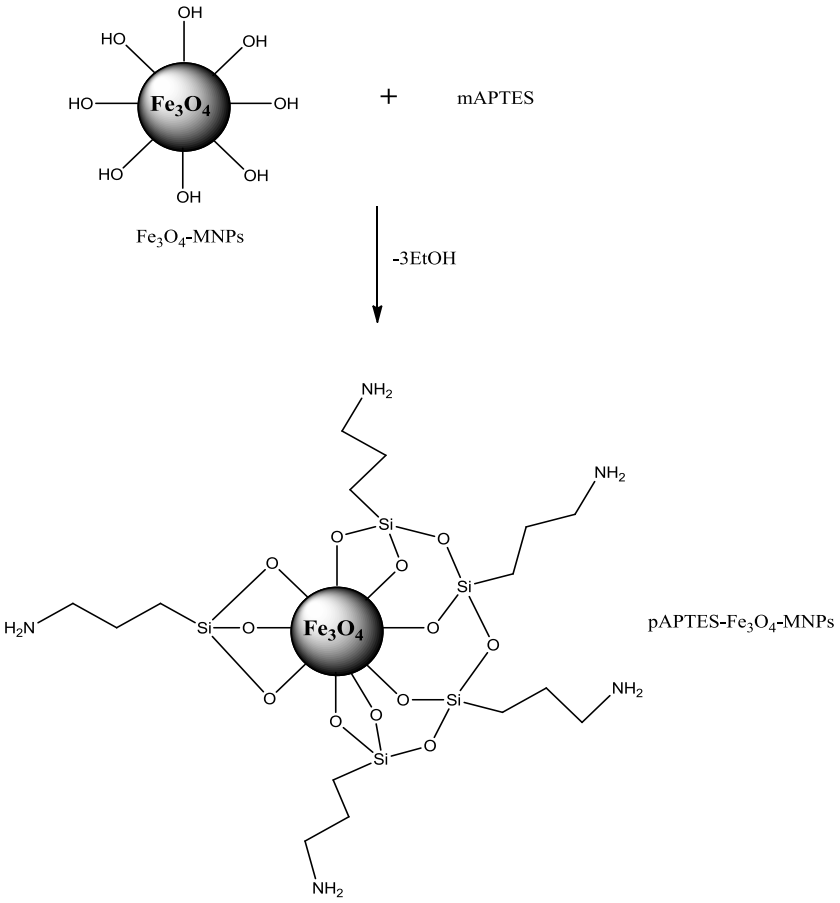

Figure 12. Schematic for the surface coating of Fe_3O_4-MNPs with monomeric (3-aminopropyl)triethoxysilane (mAPTES) to give pAPTES-Fe_3O_4-MNPs.

For nanoparticles, this ratio becomes significantly large causing a large portion of the atoms to reside on the surface compared to those in the core of the particle. For example, for a particle of 1 µm in diameter, *ca.* 0.15% of its atoms are on the surface, while for a 6 nm diameter particle *ca*. 20% of its atoms are on the surface. It is the large surface-to-volume ratio of the NPs which is the controlling factor for their novel physical, chemical and mechanical properties compared to those of the corresponding bulk material.

Nanoparticles can be synthesised either by chemical or by physical means, including thermal decomposition and reduction, co-precipitation, sol-gel, reverse micelle and emulsion solvent evaporation[35,44].

Nanoparticles of Fe_3O_4 have a large surface to volume ratio, and for the present research were synthesised using a published 'bottom-up' approach[43]. When base is added to an aqueous mixture of Fe(II) and Fe(III) ions, magnetite (Fe_3O_4) is formed[55] (Figure 13). For this research, $FeCl_2$ and $FeCl_3$ were dissolved in water and MNPs were co-precipitated by the addition of NH_4OH to the solution. The temperature at which the reaction is carried out and the concentration of ions in the reaction mixture control the resulting nanoparticle size. Since the properties of synthesised nanoparticles are affected by their size, it is necessary to have a narrow size distribution[53]. The definite composition of $FeCl_2$ and $FeCl_3$ allows for a precise reactant stoichiometric ratio (2:1) which is necessary for the co-precipitation reaction, as it has been reported that other ratios do not yield the correct product[56].

(a) (b) (c)

Figure 13. (a) Naturally occurring magnetite (Fe_3O_4)[57], (b) synthesised magnetite nanoparticles(Fe_3O_4-MNPs)[58], and (c) MNPs in a magnetic field[59].

Oxidation of the iron(II) ion in the aqueous solution is prevented, and particle size reduction is achieved by using flowing nitrogen gas during the synthesis[43]. In magnetite, iron(II) and iron(III) ions are found with both tetrahedral and octahedral geometry[60]. Fe_3O_4 forms in an inverse cubic spinel structure (Figure 14). The oxygen atoms form a face-centred cubic structure (fcc) and the iron(II) and iron(III) cations occupy the interstitial octahedral and tetrahedral sites, respectively[61]. Electron transfer occurs between the iron(II) and iron(III) sites[62].

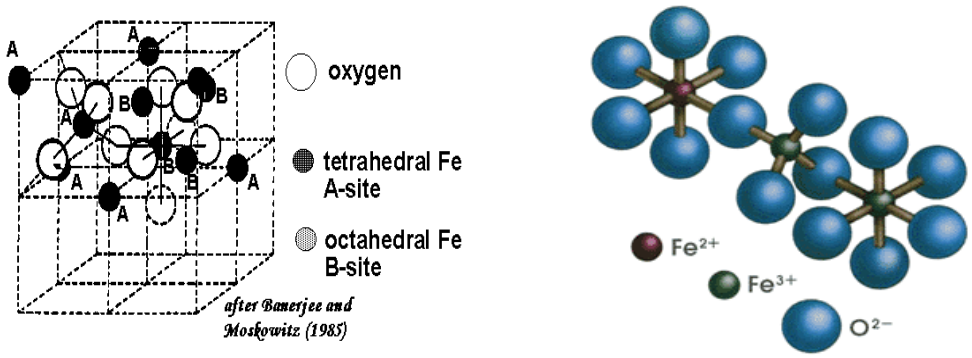

(a) (b)

Figure 14. Structure of Fe_3O_4. (a) The inverse spinal crystal lattice structure[63]and (b) The local coordination geometries of the iron(II) and iron(III) ions[64].

It is possible to extract Fe_3O_4-MNPs from a colloidal suspension by simply placing a magnet beneath the container and decanting the supernatant (Figure 15).

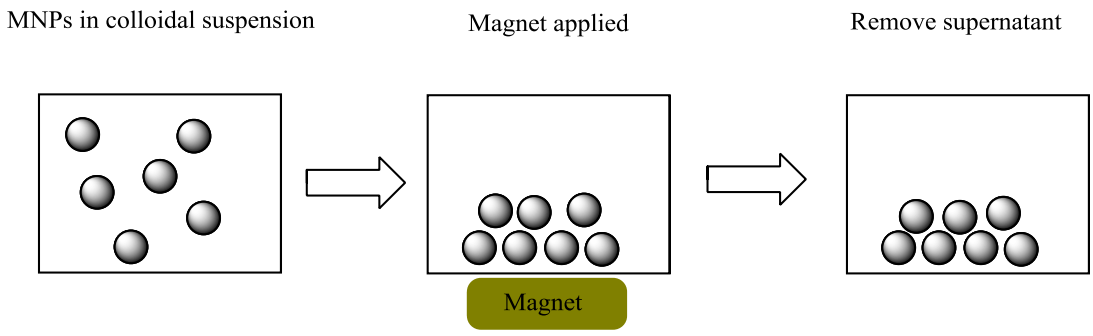

Figure 15. Use of a magnet to extract Fe_3O_4-MNPs from a colloidal suspension.

1.4.3 Silicone-coated Fe_3O_4-MNPs as Drug Delivery and Imaging Systems

Prescribed drugs can cause problems for patients for various reasons, such as insufficient active drug being available at the site where it is required, or unwanted side effects like nausea or hair loss occurring. For example, conventional chemotherapy drugs may not be site specific and thus interact with both normal and abnormal cells[65]. One method which is employed to circumvent such potential problems is to strategically place drug molecules at a selected location by using a catheter to deliver the required drugs. A selective delivery system such as this allows for a therapeutic dose of medication to be delivered to a specific area such as the site of a tumour (Figure 16).

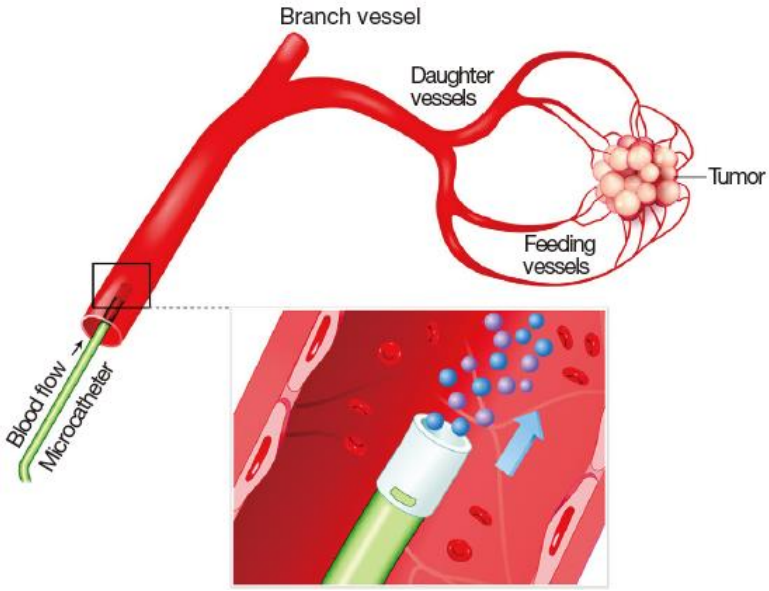

Figure 16. Targeting a tumour with microspheres[66].

A similar system of targeted drug delivery can be achieved by coating MNPs with biocompatible polymers and then attaching the required drug molecule to the

coated MNPs. When injected into the bloodstream, bare nanoparticles can adsorb proteins and agglomerate, and they can be removed quickly by macrophages[67]. Surface-coating magnetic nanoparticles with silicone polymers is a method used to prevent damage to biological systems, since bare magnetite can cause detrimental health effects[43]. Silicone polymers are very hydrophobic, and when these polymers are used to coat MNPs in a monolayer they have the effect of reducing particle-particle magnetic interactions, hence increasing the time a drug can circulate in the body[67].

Surface coating nanoclusters with layers of silicone polymer increases the size of the nanocluster and passivates the surface. In addition, agglomeration is reduced and steric stabilisation is increased[34,49,53]. Silicone-polymer-coated-MNPs can be further functionalised to carry drugs as they are non-toxic and can be introduced intravenously[49]. As a result of their magnetic functionality these drugs can be more effective than conventional therapies as they can be precisely placed using a magnetic field[51,67,68]. The following example illustrates both the problem and the solution. The blood-brain barrier (BBB) is composed of endothelial cells with tight cell junctions[69]. It protects the central nervous system in higher mammals by preventing passive diffusion within the system. This protective barrier can prevent the delivery of a therapeutic dose of drugs to sites within the brain. In the case of brain tumours, such as malignant glioma, surgery often is not possible due to the risk of damaging healthy brain tissue. MNPs which have been functionalised with appropriate drugs can be delivered to the site of a brain tumour. This can be achieved by using

ultrasound to separate the tight junctions of the BBB. Applying a magnetic field at the tumour site allows the drug molecules to be delivered to the specific target location[70-72].

Xie *et al*. reviewed the potential use of surface-engineered magnetic nanoparticle assemblies for use in cancer imaging and therapy (theranostic agents)[73]. The nanoparticles can be prepared with close control of composition, size, shape, magnetization, relaxivity and surface charge. Although still at an early stage in their development, some of these materials have a realistic potential to translate to the clinic.

Ninjbadgar and Brougham[74] surface-coated Fe_3O_4 magnetic nanoparticles with aggregation-preventing (3-glycidyloxypropyl)trimethoxysilane and then employed ring-opening coupling reactions to coat the epoxy-functionalized materials with aminated polymers (polyetheramines) and small molecules (e.g. arginine). The resulting stable nanoparticles had exceptionally high spin-lattice relaxivity (r1) values, offering a potential use as MRI contrast agents.

Cao and co-workers[49] prepared a superparamagnetic, nanocomposite material comprising a Fe_3O_4/amino-silane core and pendant cyclodextrins (Fe_3O_4-MNPs-pAPTES-CD) (Figure 17). They postulated applications including magnetically-responsive drug delivery vehicles and bioseparation technology.

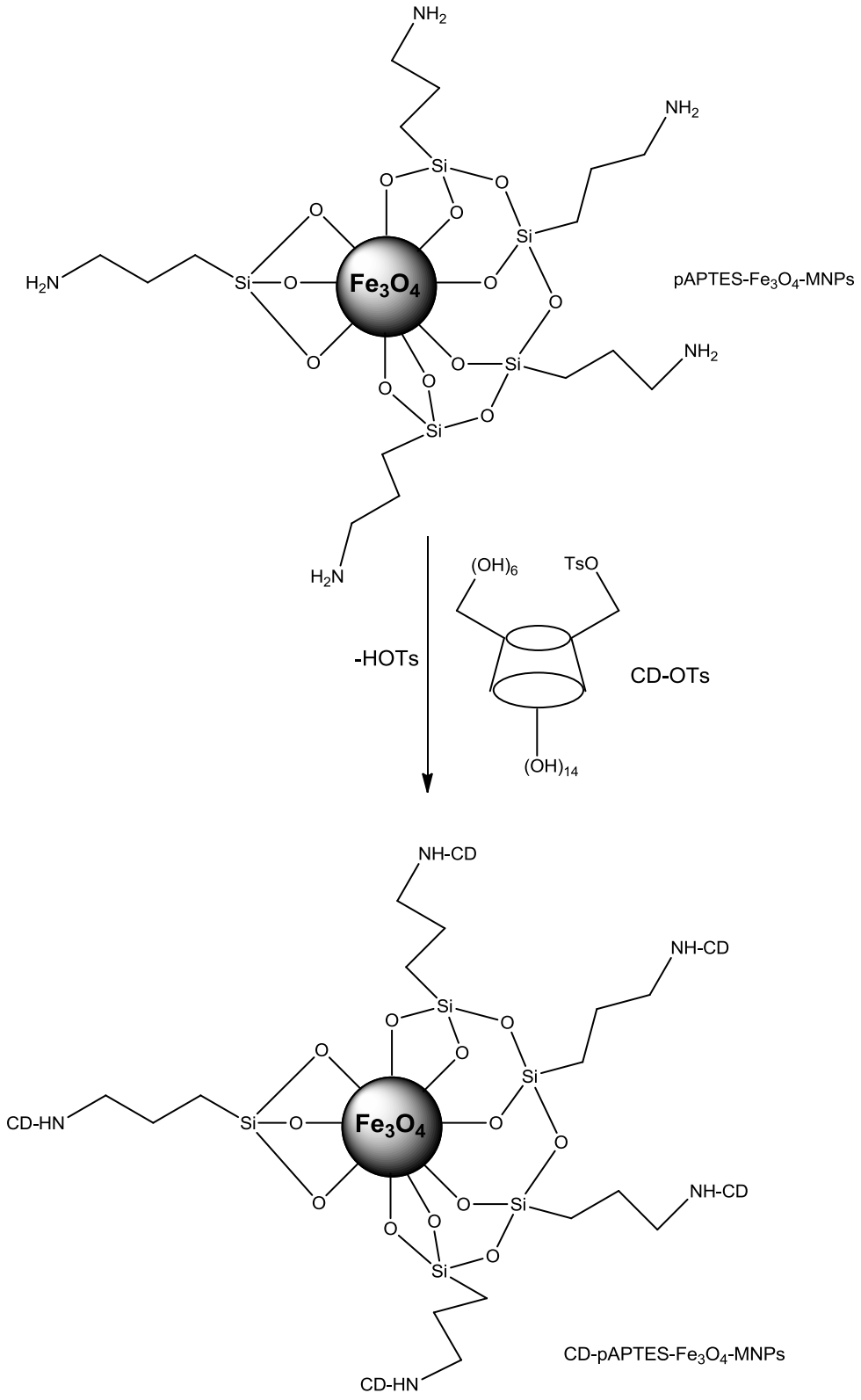

Figure 17. Schematic for formation of cyclodextrin-functionalised , silicon-coated magnetic nanoparticles (Fe_3O_4-MNPs-pAPTES-CD)[49].

1.5 Microbial Infections

1.5.1 Infectious Diseases and Microorganisms

Infectious diseases (Figure 18) can be caused by the following classes of microorganisms[41,75].

- ***Bacteria*** - These one-cell organisms are responsible for illnesses, such as strep throat, urinary tract infections and tuberculosis.
- ***Fungi*** **-** Many skin diseases, such as ringworm and athlete's foot, are caused by fungi. Other types of fungi can infect the lungs and the nervous system.
- **Viruses** - Even smaller than bacteria, viruses cause a multitude of diseases such as the common cold, shingles and acquired immune deficiency syndrome (AIDS).
- ***Parasites*** **-** Malaria and Leishmaniasis are caused by tiny parasites that are transmitted by mosquito and sandfly bites, respectively. Other parasites may be transmitted to humans from animal faeces.

Different pathogens have different modes of transmission. For example, respiratory pathogens are usually airborne and intestinal pathogens are normally spread by water or food. Drinking water that is contaminated by human or animal faeces, is likely to contain disease-causing microbes.

(a)

(b)

(c)

(d)

Figure 18. Examples of (a) Strep throat – bacterial[76], (b) Athlete's foot – fungal[77], (c) Shingles rash – viral[78] and (d) Leishmaniasis – parasitic[79] infections in humans.

Clean water, hygiene and good sewerage systems prevent the spread of water-borne diseases such as typhoid and cholera. Inanimate objects such as bedding, towels, toys and barbed wire can carry disease-causing organisms. For example, the *Trichophyton* fungus, which causes athlete's foot, can be spread indirectly through towels and changing room floors. Germs can linger on table tops, doorknobs or faucet handles and be transmitted directly to a person who touches them.

Some of the more common human diseases and infections and their causative microorganism are listed in Table 2[80].

Table 2. Common human diseases and infections and their microbial causes[80].

Ailment	Bacteria	Fungus	Protozoa	Virus
Athlete's foot		x		
Common cold				x
Diarrheal diseases	X			
Flu				x
Genital herpes				x
Meningitis	x			x
Pneumonia	x	x		x
Shingles				x
Sinusitis	x	x		
Skin diseases	x	x	x	x
Strep throat	x			
Tuberculosis	x			
Urinary tract infection	x			
Vaginal infection	x	x	x	

According to healthcare experts, infectious diseases caused by microbes are responsible for more deaths worldwide than any other single cause[41,75]. In the United

States alone, the estimated annual cost for medical care for treating infectious diseases is around $120 billion. Coupled with the crisis of the continuous emergence of highly drug-resistant microbial strains[81] there is an urgent demand for the development of new therapeutics.

1.5.2 *Candida albicans*

Fungal infection (mycosis) can either be cutaneous or systemic. Opportunistic mycosis results from a change in the biochemistry of the host, enabling proliferation of a commensal organism, such as *C. albicans*. Of the seven major *Candida* species, *C. albicans* is the most virulent[82]. This opportunistic fungal pathogen is polymorphic and changes its morphological structure between yeast, pseudohyphae and hyphae forms[83] (Figure 19).

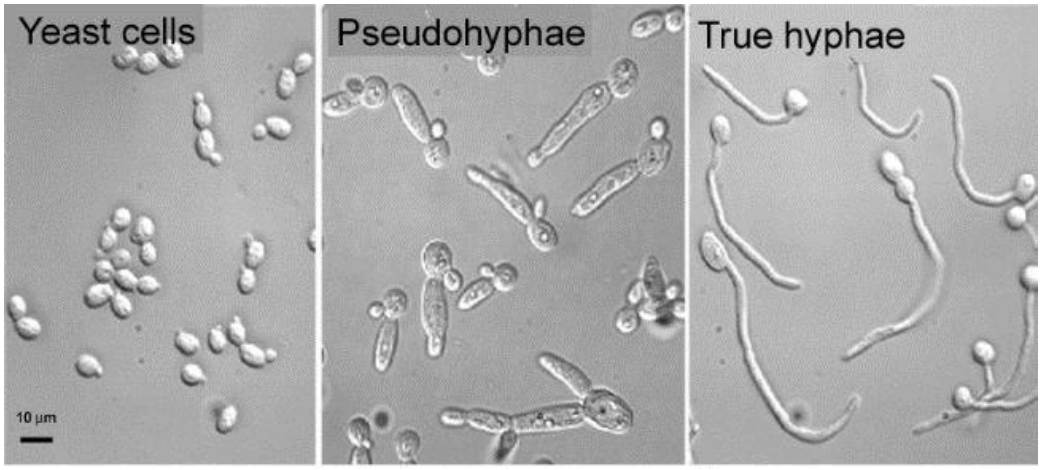

Figure 19. Yeast, pseudohyphae and true hyphae forms of *C. albicans*[84].

Infection by *C. albicans* follows colonisation of the skin, mucosa and gastro-intestinal tract. Although *C. albicans* is generally a harmless commensal, patients undergoing

antibiotic therapy and those who are immunocompromised can succumb to candidiasis (Figure 20). Indeed, oral/pharyngeal candidiasis is considered a marker for the onset of AIDS in human immunodeficiency virus (HIV+) patients, and oral cancer patients[85]. *C. albicans* cells are frequently found in biofilm-related infections[86].

Figure 20. *C. albicans* cutaneous oral infection(thrush)[87].

Candida species are becoming increasingly resistant to organic antifungal drugs and this resistance leads to greater healthcare costs. Since *ca.* 1970, the annual death rate due to candidiasis has increased and this has generally been attributed to a number of factors such as patients undergoing immunosuppressant drug therapies, indiscriminate use of antibacterial agents and long term use of catheters[88]. The duration of treatment can also be a factor, with increasing risk of infection linked to duration of hospital confinement[89].

Currently prescribed fungistatic azole drugs such as miconazole and fluconazole (Figure 21), target the biosynthetic pathway of ergosterol, the main cell wall component in both the yeast and filamentous forms of *C. albicans*[90]. The polyene

drugs, such as amphotericin B (Figure 21) and nystatin, are fungicidal and damage the plasma membrane by essentially dissolving out the vital ergosterol present in the membrane[91]. Amphotericin B is severely nephrotoxic[92] and azole drugs can cause endocrine problems in mammals due to inhibition of cytochrome P450[93].

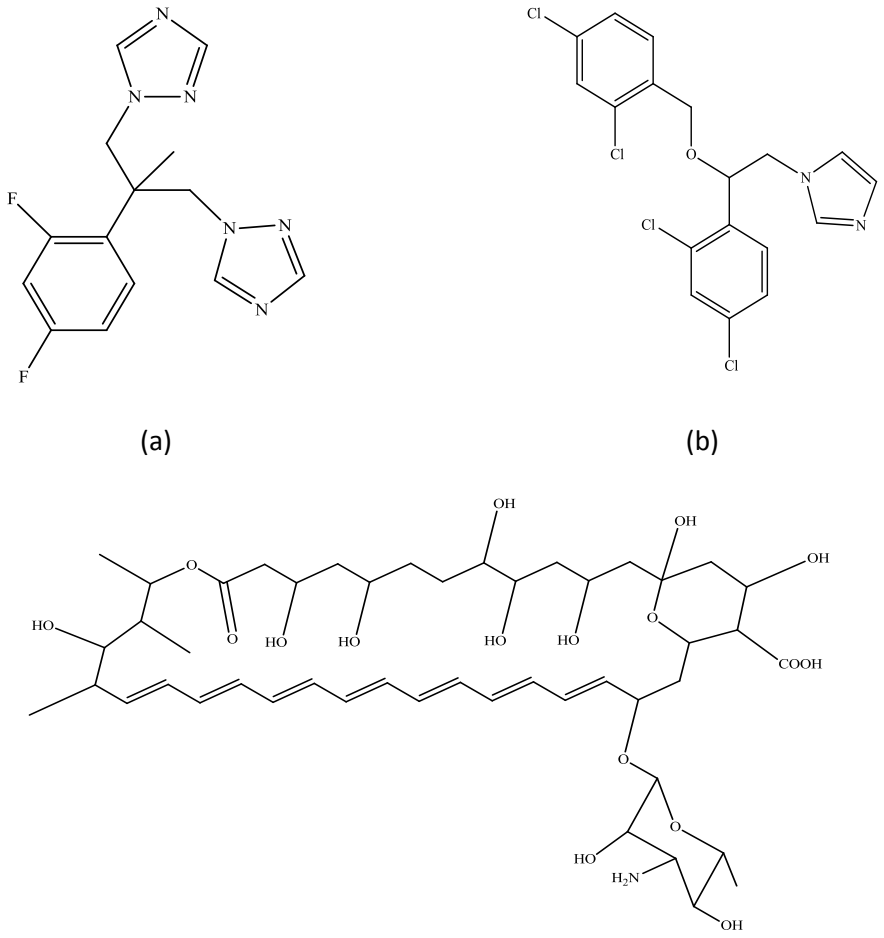

(a) (b)

(c)

Figure 21. Azole drugs (a) fluconazole and (b) miconazole and (c) the macrocyclic polyene drug, amphotericin B.

Previous studies on *Candida* species have shown that metal ions, including copper(II), block or cause the transition between different yeast morphologies[94], and can kill the

organism[95]. Copper(II)-complexed 1,10-phenanthroline (phen) ligands (Figure 22) have been found to damage mitochondrial function and inhibit respiration in fungi[96], and phen co-complexed with malonic acid and chelated to copper(II) was shown to have good activity with respect to inhibition of the growth of *C. albicans*[97].

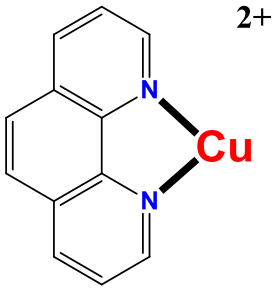

Figure 22. Copper(II) ion chelated by 1,10-phenanthroline (phen).

Copper ions are known to have an affinity for sulphur and nitrogen-containing molecules and this may affect proteins containing these particular donor atoms[98]. Inorganic derivatives of phen-based compounds may have applications with respect to fungal inhibition due to the fact that their mode of inhibition is different to that of the organic antifungal prescription drugs[99]. Metal-free phen also has potent antifungal activity, and it is assumed that the bio-active N,N´ chelating base sequesters trace metals from either the growth media or from metalloproteins associated with the organism, and that the resulting metal-phen complexes are the active species[100]. In complexes where phen was replaced by 2,2'-bipyridine (bipy), only very minimal anti-*Candida* activity was observed[97]. Manganese(II)-phen complexes have been shown to damage mitochondrial function and respiration[101]. Interestingly, *Candida* specimens treated with copper(II)-phen complexes showed

reduced ergosterol levels, whilst the equivalent manganese(II) complexes caused an increase in the amount of ergosterol. Levels of respiratory cytochromes b and c (which are components of the electron transport chain in mitochondria) in *Candida* cells decreased upon administration of copper(II) and manganese(II)-phen complexes.

1.6 Copper Chemistry and Biological Activity

1.6.1 General Copper Chemistry

Copper is positioned in the d-block in the Periodic Table and is a soft, malleable metal with a reddish-orange tarnish. Although some natural deposits of metallic copper have been found, it is generally mined either as a sulphide (e.g. covellite (CuS), charlcocite (Cu_2S) and bornite (Cu_3FeS_3)), or as a hydroxide (e.g. malachite $Cu_2CO_3(OH)_2$), silicate (e.g. chrysocolla, $CuSiO_3.2H_2O$), or sulphate (e.g. chalcanthite $CuSO_4.5H_2O$))[102].

1.6.2 Coordination Chemistry of Copper

Metallic copper has the electronic configuration [Ar] $3d^{10}4s^1$ and the copper(II) oxidation state, [Ar] $3d^9 4s^0$, is the most common. The complex salt, $Cs_2[CuCl_4]$, has the copper(II) ion at the centre of a tetrahedron and in $[EtNH_3]_2[CuCl_4]$ the metal has square-planar coordination geometry. $[Cu(bipy)_2I]^+$ and [{Cu(dimethylglyoxime)$_2$}] have trigonal bipyramidal and square-pyramidal structures, respectively, whilst the copper(II) ion has an octahedral coordination geometry in $K_2Pb[Cu(NO_2)_6]$[103].

1.6.3 Biological Activity of Copper Ions

The fact that copper ions are essential for life was first recognised in 1928[104]. Copper ions are present in all plants and animals and are also found in a variety of enzymes such as superoxide dismutase and cytochrome c oxidase[105]. As the third most abundant natural trace metal element in the body, after iron and zinc, it is found in varying concentrations (from a few ppm to several hundred ppm) in all organs and tissues of the human body[106]. In the body, it is not normally found as a free copper ion but rather as bonded to cellular proteins and organic compounds[107]. Dietary sources of copper are food (e.g. leafy greens, nuts, whole grains, oysters etc.), drinking water and copper-containing supplements, and the estimated adult daily intake from food is 1.0-1.3 mg/day (0.014-0.019 mg kg^{-1}/day)[107]. Copper-containing ointments are said to be beneficial due to the fact that copper(II) ions are necessary for promoting the growth of endotheilial cells and also for the stabilisation of skin proteins[108]. Small amounts of the ions can be acquired through a reaction between metallic copper and sweat (by wearing a copper bracelet) or by topical application of ointments containing a high concentration of copper(II) ions (Figure 23)[109].

(a) (b)

Figure 23. (a) A copper bracelet[110], and (b) a copper(II)-containing, commercially available wound ointment for topical application[111].

1.6.4. History of the Medicinal Uses of Copper

The biocidal use of copper has been known since *ca.* 2000 B.C. when the ancient Egyptians used it to sterilise water and wounds[112]. Since then, copper has been prescribed for a sore throat, boils, skin and eye infections[113] as well as lung disease[114]. From 1761, when it was found that soaking seed grains in aqueous $CuSO_4$ inhibited fungal growth, copper has been widely utilised for its antimicrobial properties. In the 1880s, a combination of $CuSO_4$, lime and water, referred to as the Bordeaux mixture (Figure 24), and a blend of $CuSO_4$ and sodium carbonate, known as the Burgundy mixture, became popular fungicides for prevention of infection in grapes and vines.

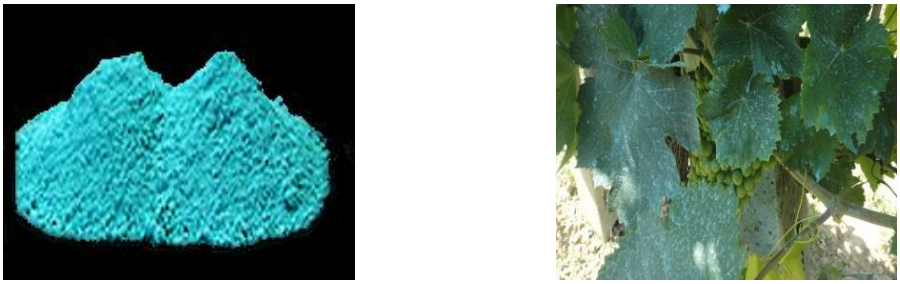

(a) (b)

Figure 24. (a) Bordeaux mixture and (b) Bordeaux mixture on the surface of vines and grapes.

Copper ions are still used extensively today for their antimicrobial properties and they can kill a wide spectrum of yeast and fungi (e.g. *Aspergillus carbonarius*, *C. albicans*, *Saccharomyces cerevisiae*), bacteria (e.g. *Escherichia coli*, *Listeria monocytogenes*, *Staphylococcus epidermidis*) and viruses (e.g. Poliovirus, Human Immunodeficiency Virus Type 1 (HIV-1), Influenza A) The US Environmental Protection Agency has verified the beneficial use of antimicrobial copper as a touch surface material, supporting the claim of the continuous kill of >99.9% of bacteria

that come in contact with the metal within a period of two hours[112]. In addition to bacteria, copper surfaces also have antifungal and antiviral properties[36]. Copper metal has been incorporated into a number of household items such as cabinet handles, cistern handles, dressing trolleys, taps and bed rails (Figure 25)[35,39]. In all cases, it is the copper(II) cation, and not the atom (copper(0)), which is responsible for the bioactivity.

(a) (b) (c)

Figure 25. (a) A copper sink, (b) a copper door handle, and (c) copper covered light switch panel.

In an attempt to prevent nosocomial infection, CuO has been incorporated into various textiles, such as polyester, polypropylene, polyethylene, polyurethane and nylon, which are used in the manufacture of pyjamas, socks, sheets and many other items[115]. Encouragingly, reports of resistance to copper are somewhat rare[116]. There are numerous references to copper-based, non-steroidal, anti-inflammatory drugs offering reduced gastrointestinal toxicity when compared to the parent, non-metal constituents[117,118]. Although there are currently no oral delivered copper-based drugs being prescribed, an ethanolic gel-base of copper-salicylate (Alcusal®) is

frequently used as a topical treatment for the relief of pain and inflammation[119]. A solution of copper(II) naphthenate (Kopertox®) is used for the treatment of equine thrush[120] and copper(II) glycinate[121] is injected into cattle to prevent copper deficiency. A DMSO solution of copper(II) salicylate (Dermcusal®) is topically applied as an anti-inflammatory and anti-arthritic agent for animals[122].

The toxicity of the copper ion is thought to be due to the generation of reactive oxygen species (ROS), which occurs during the redox cycling between the copper(I) and copper(II) oxidation states (equations below)[123]. Reduction of copper(II) to copper(I) in the presence of superoxide is followed by the re-oxidation to copper(II) by hydrogen peroxide and the generation of highly toxic hydroxyl radicals[124].

$$Cu(II) + O_2^{-\cdot} \longrightarrow Cu(I) + O_2 \quad (4)$$

$$Cu(I) + H_2O_2 \longrightarrow Cu(II) + OH^- + OH^{\cdot} \quad (5)$$

Acute copper toxicity is rare and is mostly confined to young children who have accidently swallowed copper solutions. Copper salts are powerful emetics (induce vomiting) and so large doses are rejected by the body. However, copper poisoning can result in severe liver disease and neurological defects[125]. Wilson's disease is a disorder of copper metabolism and is characterised by the accumulation of copper(II) ions in various organs, resulting in liver cirrhosis, neurological disturbances and also a range of symptoms related to the disruption of copper transport systems in the body[126]. Metal ion chelator ligands containing nitrogen donor atoms, such as

triethylenetetramine (Figure 26), can bind copper(II) ions and are used to remove excess systemic copper in Wilson's disease and in some cases of diabetes mellitus[127].

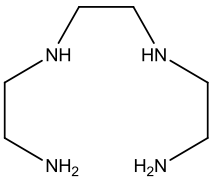

Figure 26. Structure of triethylenetetramine.

Menkes disease is an X-linked inherited chromosome disorder that causes severe prenatal and postnatal copper deficiency in males. This causes brain damage and intellectual development disorders, a scalp-hair defect (kinky hair syndrome), fragile bones, aortic aneurisms and other conditions[128]. Copper ions have also been implicated in other neurodegenerative diseases such as Alzheimer's, familial amyotrophic lateral sclerosis and Creutzfeldt-Jakob disease[125].

The potent antimicrobial properties of copper(II), coupled with its relatively low toxicity towards mammalian cells, prompted its use in the present research work. The present study aims to incorporate antimicrobially active copper(II) ions into water-insoluble silicone polymers and also into silicone polymers that have been anchored onto the surface of Fe_3O_4 magnetic nanoparticles.

CHAPTER 2

Experimental

2.1 General Methodology

2.1.1 Chemicals

Chemicals were obtained from commercial sources and, unless specified, were used without further purification.

2.1.2 Infrared Spectroscopy

Infrared spectra were obtained using a Perkin Elmer 2000 FT-IR spectrophotometer. KBr discs were used for all spectra.

2.1.3 ^{1}H NMR Spectroscopy

NMR (δ ppm; J Hz) spectra were recorded for soluble compounds on a Bruker Avance 300 MHz NMR spectrometer and also on a Bruker AVII500 500 MHz NMR spectrometer using saturated $CDCl_3$ solutions with Me_4Si reference, unless indicated otherwise, with resolutions of 0.18 Hz and 0.01 ppm.

2.1.4 Scanning Electron Microscopy and Energy Dispersive X-ray

Scanning Electron Microscopy (SEM) and Energy Dispersive X-ray (EDX) analyses were carried out on a Hitachi S-3200N Scanning Electron Microscope. The selected samples were mounted on carbon tabs. In the present study, EDX analysis of selected samples was carried out in order to qualitatively assess the elements present in the sample. It should be noted that EDX analysis does not directly correlate with the total carbon

and metal content of a sample as determined by microanalysis. EDX analysis will only provide data relevant to the sample surface and the layer just immediately below the surface (which can be penetrated by the electron beam), whereas microanalysis is for the total bulk sample.

2.1.5 Transmission Electron Microscopy

Transmission Electron Microscopy (TEM) images were obtained using a Hitachi H-7650 at the Royal College of Surgeons in Ireland, 123 St. Stephen's Green, Dublin. The samples were prepared on 400 mesh copper grids coated with Formvar film. The MNPs were suspended in ethanol, dropcast onto the grids and dried at ambient temperature.

2.1.6 Acetone Piston

Prepared samples were dried in a drying piston under vacuum at the temperature of refluxing acetone (56.5 °C).

2.1.7 Microanalytical Data

Microanalytical data were obtained using a Flash EA CHN Analyser.

Although the mass yield of polymeric products have been given the % yields have not been stated as the materials have generally an appreciable amount of encapsulated reaction solvent and/or washing solvent.

2.1.8 Solvents

Solvents used for solubility tests were water, ethanol, methanol, chloroform, dichloromethane (DCM), dimethylsulfoxide (DMSO), toluene, acetonitrile and dimethylformamide (DMF).

2.1.9 Sonication

For reactions in which samples were dissolved/suspended via sonication, a Branson 1510 sonicator bath was used.

2.1.10 Sterilisation of Microbiological Media and Equipment

A Dixons ST228 autoclave was used to sterilise the microbiological media and equipment at 121 °C and 124 kPa for 20 minutes.

2.1.11 Antimicrobial Assays

Candida albicans ATCC 10231 was obtained from the American Type Culture Collection (Manasas, VA, USA). For the antifungal testing, all work surfaces were washed with ethanol/water 70% (v/v) and a Bunsen flame was used to sterilise the immediate atmosphere while the *C. albicans* cells were plated, at a concentration of 1×10^{-6} cells cm^{-3}, onto pre-sterilised yeast extract peptone dextrose (YEPD) growth medium contained in petri dishes[129]. The petri dishes were incubated for 0.5 h at 37 °C. Three separate portions of each individual solid test sample were added and the plate then incubated for 20 h at 37 °C. The degree of fungal growth inhibition was visualised, photographed and the results tabulated.

2.1.12 MNP Separation

Freshly prepared Fe_3O_4 magnetic nanoparticles were separated from suspension using a neodymium-iron alloy magnet, N52 NdFeB + NiCuNi (size 50 x 50 x 25 mm), supplied by Magnet Expert Ltd. (code F335-N52). The magnet was placed under the reaction flask and the MNPs were held at the bottom of the flask. The mother liquor was decanted off and the MNPs were washed several times with ethanol and then dried in a vacuum desiccator**.** Samples of polymer-coated magnetic nanoparticles, which could not be efficiently separated from suspension using the neodymium-iron alloy magnet, were recovered by centrifugation at 10,000 rpm (14.336 x *g*) using a Beckman Coulter Optima L-100 XP Ultra centrifuge and then washed with either ethanol or methanol and dried in a vacuum desiccator.

2.1.13 Structural Diagrams

Where structural diagrams are given for polymeric species these are only one of a number of structural possibilities.

2.2 Fe_3O_4-MNPs

Fe_3O_4 magnetic nanoparticles were made using the following co-precipitation literature method[43]. $FeCl_3 \cdot 6H_2O$ (11.68 g, 43.21 mmoles) and $FeCl_2 \cdot 4H_2O$ (4.60 g, 21.60 mmoles) were dissolved with stirring in deoxygenated millipore water (200 mL) and under flowing N_2 gas. The pH of the suspension was pH 0.6 and the temperature was raised to 85 °C. Following 0.5 h of mechanical stirring, a single portion of NH_4OH (15 mL, 25% v/v) was added, causing an immediate precipitation of a black material and a resulting change in the pH of the suspension to pH 8. This suspension was stirred for a further 0.5 h and then cooled to room temperature. The black precipitate was separated using magnetic decantation, washed twice with millipore water and once with aqueous NaCl (0.02 M) followed by a final wash with millipore water. The solid was dried in a vacuum desiccator and stored in a desiccator.

Yield: 4.60 g, 92 %.

IR (KBr, cm^{-1}): 3385 (H-O-H stretch), 1631 (H-O-H bend), 1399, 1012, 800-400 (Fe-O).

2.3 pAPTES

mAPTES was polymerised in accordance with the patented procedure[24]. mAPTES (2.00 g, 9.03 mmoles) was added dropwise to water (50 mL) and the resulting clear solution was left stirring overnight at room temperature. The solvent was removed

under reduced pressure. A colourless crystalline solid was recovered and this was washed with ice-cold water and ice-cold ethanol on a sintered glass funnel. This washing procedure was repeated three times. The glass-like flakes were then dried under vacuum at 56 °C.

Soluble in H_2O, EtOH and MeOH

Yield: 0.91 g.

IR (KBr, cm^{-1}): 3600-3200 (H-O-H and H-N-H), 2932-2875 (C-H), 1700-1500 (H-O-H and H-N-H), 1474 (C-C), 1200-900 (Si-O-Si), 749 (Si-C).

^1H NMR (ppm, D_2O)$_\delta$: 2.76 (m, H_c), 1.57 (m, H_b), 0.46 (m, H_a).

Anal. Found: C 26.48%, H 6.76%, N 9.40%.

2.4 pAPTES-Fe_3O_4-MNPs

pAPTES-modified Fe_3O_4 magnetic nanoparticles (pAPTES-Fe_3O_4-MNPs) were made in accordance with a reported literature method[49]. Fe_3O_4-MNPs (0.300 g, 1.290 mmoles) were ground to a fine powder using a mortar and pestle, and then dispersed in a mixture of ethanol (600 mL) and water (4 mL) by sonication. To the resulting suspension was added monomeric (3-aminopropyl)triethoxysilane (mAPTES) (120 µL, 0.122 g, 0.551 mmoles) using a micropipette. The mixture was sonicated at room temperature for 0.25 h and then mechanically stirred for 7 h. The suspension was separated by centrifugation (10,000 rpm (14.336 x *g*)) and then re-dispersed by sonication in fresh ethanol and then separated again using magnetic decantation.

This re-dispersion/decantation process was repeated a further five times. The black pAPTES-Fe_3O_4-MNPs were dried in a vacuum desiccator and stored in a desiccator.

Yield: 0.250 g.

IR (KBr, cm^{-1}): 3404 (H-O-H stretch), 1625 (H-O-H bend), 1511, 1150-900 (Si-O-Si), 800-400 (Fe-O).

Anal. Found: C 1.90%; H 0.70%, N 0.39%.

2.5 $[(NO_3)_2Cu$-pAPTES]

$[(NO_3)_2Cu$-pAPTES] was synthesised using a published procedure[129]. mAPTES (125 µL, 0.118 g, 0.534 mmoles) was added dropwise to a solution of $Cu(NO_3)_2.3H_2O$ (0.280 g, 1.158 mmoles) in water (5 mL). The resulting blue solution was stirred overnight. The solvent was removed under reduced pressure. The blue solid was washed three times with ice-cold water and three times with ice-cold ethanol on a sintered glass funnel. The royal blue, glass-like flakes were dried under vacuum at 56 °C.

Insoluble in all common solvents.

Yield: 0.136 g.

IR (KBr cm^{-1}): 3700-3100 (H-O-H and H-N-H), 2930 (C-H), 1700-1600 (H-O-H and H-N-H), 1384 (NO_3), 1200-900 (Si-O-Si).

Anal. Found: C 18.53%, H 4.35%, N 10.52%.

2.6 [$(OAc)_2$Cu-pAPTES-Fe_3O_4-MNPs]

pAPTES-Fe_3O_4-MNPs (0.15 g) were sonicated until finely dispersed in ethanol (200 mL). To this suspension was added a solution of $[Cu_2(OAc)_4(H_2O)_2]$ (0.05 g, 0.125 mmoles) in ethanol (15 mL). The mixture was sonicated for 0.5 h and then stirred mechanically for 1 h. The resulting suspension was decanted magnetically and washed with fresh ethanol. This re-dispersion/decantation process was repeated a further three times. The black powder was dried in a vacuum desiccator and then stored in a desiccator.

Yield: 0.03 g.

IR (KBr, cm^{-1}): 3422 (H-O-H and H-N-H), 2923 (C-H), 1700-1500 (H-O-H, H-N-H and O-C-O), 1385 (O-C-O), 1200-1000 (Si-O-Si), 700-450 (Fe-O).

Anal. Found: C 1.63%, H 0.41%, N 0.29%.

2.7 SalH-pAPTES

method (a) – using mAPTES

Salicylaldehyde was added to mAPTES using a modified literature procedure[129]. Salicylaldehyde (0.50 g 4.09 mmoles) was added dropwise to neat mAPTES, (1.00 g, 4.50 mmoles) while stirring. The viscous yellow solution was stirred for 0.6 h and the solvent was then removed under vacuum. The yellow solid was washed with methanol three times and dried under vacuum at 56 °C.

Insoluble in all common solvents.

Yield: 0.43 g.

IR (KBr, cm^{-1}): 3366 (H-O-H and H-N-H), 2932 (aliphatic C-H), 1634 (C=N), 1600-1500 (H-O-H and H-N-H), 1200-900 (Si-O-Si).

Anal. Found: C 31.79%, H 6.57%, N 9.80%.

method (b) – using pAPTES

pAPTES, (1.00 g, 4.50 mmoles) was ground to powder using a pestle and mortar. To this was added salicylaldehyde (0.50 g, 4.09 mmoles) dropwise while stirring. The viscous yellow solution was stirred for 0.6 h and then evaporated under vacuum. The yellow solid was washed with methanol three times and dried under vacuum at 56 °C.

Insoluble in all common solvents.

Yield: 0.47 g.

IR (KBr, cm^{-1}): 3433 (H-O-H and H-N-H), 3100 (aromatic C-H), 2932 (aliphatic C-H), 1634 (C=N), 1600-1500 (H-O-H and H-N-H), 1200-900 (Si-O-Si).

Anal. Found: C 47.58%, H 5.83%, N 7.30%.

2.8 SalH-pAPTES-Fe_3O_4-MNPs

pAPTES-Fe_3O_4-MNPs (0.15 g) were sonicated in ethanol (200 mL) until finely dispersed. To this suspension was added, dropwise, a solution of salicylaldehyde (0.08 g, 70 µL, 0.65 mmoles) in ethanol (20 mL). Sonication was continued for *ca.* 5 minutes, followed by mechanical stirring for 3.5 h. The particles were separated by magnetic decantation and then re-dispersed in fresh ethanol. This re-dispersion/decantation process was repeated a further five times. The brown powder was dried in a vacuum desiccator and then stored in a desiccator.

Yield: 12.0 g.

IR (KBr, cm^{-1}): 3402 (H-O-H stretch), 1623 (C=N), 1566 (H-O-H bend), 1411, 1300-1000 (Si-O-Si), 750-450 (Fe-O).

Anal. Found: C 3.25%, H 0.47%, N 0.08%.

2.9 [Cu-Sal-pAPTES-Fe_3O_4-MNPs]

A solution of $[Cu_2(OAc)_4(H_2O)_2]$ (0.05 g, 0.12 mmoles) in ethanol (15 mL) was added dropwise to Sal-pAPTES-Fe_3O_4-MNPs (0.12 g) dispersed by sonication in ethanol (200 mL). The mixture was sonicated for a further 10 min and then placed on a mechanical stirrer for 2 h. The Cu-Sal-pAPTES-Fe_3O_4-MNPs were separated using magnetic decantation and washed with fresh ethanol. This process was repeated 5 times. The brown powder was dried in a vacuum desiccator and stored in a vacuum desiccator.

Yield: 0.08 g.

IR (KBr, cm^{-1}): 3402 (H-O-H stretch), 2918 (aliphatic C-H), 1626 (C=N), 1567 cm^{-1} (H-O-H bend), 1411, 1300-1000 (Si-O-Si), 750-450 (Fe-O).

Anal. Found: C 1.22%, H 0.23%, N 0.17%.

2.10 pTMSPDT

mTMSPDT was polymerised to form pTMSPDT by modifying a literature procedure[129]. mTMSPDT (0.50 g, 1.88 mmoles) was added dropwise to water (50 mL) whilst stirring. The colourless solution was stirred overnight at room temperature. The solvent was completely removed under vacuum to give a colourless, crystalline solid. The solid was washed with ice-cold water and then ice-cold methanol. This washing process was repeated three times. The glass-like crystal flakes were then dried under vacuum at 56 °C.

pTMSPDT was sparingly soluble in warm H_2O only.

Yield: 0.31 g.

IR (KBr, cm^{-1}): 3600-3100 (H-O-H and H-N-H and N-H), 2934 (C-H), 1700-1500 (H-O-H and H-N-H), 1473 (C-C), 1200-950 (Si-O-Si), 772 (Si-C).

^{1}H NMR (ppm, D_2O):δ 2.77 (m, H_{c-g}), 1.62 (m, H_b), 0.54 (t, H_a).

Anal. Found: C 39.04%, H 8.16%, N 18.06%.

2.11 pTMSPDT-Fe_3O_4-MNPs

pTMSPDT-modified Fe_3O_4 magnetic nanoparticles (pTMSPDT-Fe_3O_4-MNPs) were made using an amended literature method[49]. Fe_3O_4-MNPs (0.300 g, 1.290 mmoles) were ground to a fine powder using a mortar and pestle, and then dispersed by sonication in a mixture of methanol (600 mL) and water (4 mL). To the resulting suspension was added mTMSPDT (129 µL, 0.124 g, 0.467 mmoles). The mixture was sonicated for 0.25 h and then mechanically stirred for 2 h. The black product was removed from the solvent using magnetic decantation. The product was then re-dispersed using sonication in fresh methanol. This re-dispersion/decantation process was repeated a further three times. The black solid was dried in a vacuum desiccator and then stored in a desiccator.

Yield: 0.200 g.

IR (KBr, cm^{-1}): 3401 (H-O-H stretch), 2933 (C-H), 1620 (H-O-H bend), 1511, 1300-1100 (Si-O-Si), 800-450 (Fe-O).

Anal. Found: C 2.76%; H 0.68%, N 0.75%.

2.12 [$(NO_3)_2$Cu-pTMSPDT]

method (a) – using mTMSPDT

mTMSPDT (0.25 g, 0.94 mmoles) was added dropwise to a solution of $Cu(NO_3)_2.3H_2O$ (0.46 g, 1.90 mmoles) in water (5 mL). The solution was stirred for 4 h and then the

solvent was removed under reduced pressure. The solid was recovered by filtering through a sintered glass funnel. The royal blue coloured flakes were washed with ice-cold millipore water and methanol, and dried under vacuum at 56 °C.

Yield: 0.04 g.

IR (KBr cm^{-1}): 3600-3000 (H-O-H and H-N-H and N-H), 2917 (C-H), 1700-1550 (H-O-H and H-N-H), 1384 (NO_3), 1200-850 (Si-O-Si).

Anal. Found: C 19.43%, H 4.69%, N 16.55%.

method (b) – using pTMSPDT

Powdered pTMSPDT (0.13 g) was added to a solution of $Cu(NO_3)_2.3H_2O$ (0.46 g, 1.90 mmoles) in water (5 mL). The suspension was stirred for 4 h. The solvent was removed under reduced pressure and the royal blue crystal flakes were washed with ice-cold millipore water and methanol and dried under vacuum at 56 °C.

Yield: 0.03 g.

IR (KBr cm^{-1}): 3700-3100 (H-O-H and H-N-H and N-H), 3000-2800 (C-H), 1700-1550 (H-O-H and H-N-H), 1384 (NO_3), 1150-950 (Si-O-Si).

Anal. Found: C 16.98%, H 4.03%, N 13.28%.

2.13 [$(OAc)_2$Cu-pTMSPDT-Fe_3O_4-MNPs]

pTMSPDT-Fe_3O_4-MNPs (0.017 g) were dispersed by sonication in methanol. To this suspension was added a solution of $[Cu_2(OAc)_4(H_2O)_2]$ (0.060 g, 0.15 mmoles) dissolved in methanol (15 mL) and the mixture was sonicated for 1 h. The solid particles were magnetically decanted and washed with fresh methanol. This washing/decantation process was repeated three times. The black powder was separated using magnetic decantation and dried in a vacuum desiccator.

Yield: 0.010 g.

IR (KBr, cm^{-1}): 3420 (H-O-H, H-N-H and N-H), 2918 (C-H), 1700-1500 (H-O-H, H-N-H and O-C-O), 1384 (O-C-O), 1300-1000 (Si-O-Si), 700-450 (Fe-O).

Anal. Found: C 10.42%, H 0.49%, N 0.43%.

2.14 SalH-pTMSPDT

SalH-pTMSPDT was prepared according to a literature procedure[129]. Salicylaldehyde (SalH) (0.50 g, 4.09 mmoles) was added dropwise to a solution of mTMSPDT (1.05 mL, 1.09 g, 4.10 mmoles) in water (2 mL) and the solution went yellow. The yellow solution was stirred for 40 min. The solvent was removed under reduced pressure and the yellow solid product was washed with methanol and then dried under vacuum at 56 °C.

Insoluble in all common solvents.

Yield: 1.00 g.

IR (KBr, cm^{-1}): 3420 (H-O-H, H-N-H and N-H), 3048 (aromatic C-H), 3000-2800 (aliphatic C-H), 1633 (C=N), 1583 (H-O-H and H-N-H), 1200-900 (Si-O-Si).

Anal. Found: C 55.99%, H 6.82%, N 12.72%.

2.15 SalH-pTMSPDT-Fe_3O_4-MNPs

pTMSPDT-Fe_3O_4-MNPs (0.020 g) were sonicated in methanol (200 mL) until finely dispersed. To this suspension was added, dropwise, a solution of salicylaldehyde (SalH) (0.070 µL, 0.008 g, 0.066 mmoles) in methanol (20 mL). Sonication was continued for *ca.* 5 min, followed by mechanical stirring for 0.6 h. The particles were decanted magnetically and then re-dispersed in fresh methanol. This re-dispersion/decantation process was repeated a further five times. The brown powder was dried in a vacuum desiccator and then stored in a desiccator.

Yield: 0.015 g.

IR (KBr, cm^{-1}): 3434 (H-O-H, H-N-H and N-H), 2929 (aliphatic C-H), 1636 (H-O-H and H-N-H), 1350-1070 (Si-O-Si), 790-450 (Fe-O).

Anal. Found: C 8.65%, H 0.53%, N 0.51%.

2.16 [Cu-Sal-pTMSPDT-Fe_3O_4-MNPs]

$[Cu_2(OAc)_4(H_2O)_2]$ (0.15 g, 0.38 mmoles) was dissolved in methanol and added dropwise to a sonicated, methanolic dispersion of SalH-pTMSPDT-Fe_3O_4-MNPs (0.29 g). The suspension was sonicated for a further 0.25 h and then placed on a mechanical stirrer for 1 h. The solid product was separated using magnetic decantation and washed with fresh methanol. This re-dispersion/decantation process was repeated 5 times. The black powder was dried in a vacuum desiccator and stored in a desiccator.

Yield: 0.20 g.

IR (KBr, cm^{-1}): 3413 (H-O-H, H-N-H and N-H), 2925 (aliphatic C-H), 1636 (H-O-H and H-N-H), 1350-1100 (Si-O-Si), 800-460 (Fe-O).

Anal. Found: C 5.32%, H 0.52%, N 0.51%.

CHAPTER 3

Results and Discussion

This Results and Discussion section is configured to give the reader a general overview of the structural characterisation of the silicone polymers, their salicylate Schiff base derivatives and their Cu(II) complexes. Due to the insoluble nature of most of the compounds, the structural characterisation is extrapolated from a combination of IR, CHN and EDX data. Results of *in vitro* testing of the compounds against the fungal species, *Candida albicans,* are presented and discussed.

3.1 Fe_3O_4-MNPs

3.1.1 Fe_3O_4-MNPs

Black Fe_3O_4 magnetic nanoparticles (Fe_3O_4-MNPs) were prepared in good yield by using a literature co-precipitation method[43]. The IR spectrum of Fe_3O_4-MNPs (Figure 27) contains a cluster of strong Fe-O bands in the region 800-400 cm^{-1} which are comparable with the previously reported literature values[43,52]. The bands at 634 and 584 cm^{-1} are assigned to splitting of the Fe-O 570 cm^{-1} band which occurs in the spectrum of 'bulk' magnetite. The Fe-O 375 cm^{-1} band in 'bulk' magnetite shifts to 443 cm^{-1} in the spectrum of nanoparticulate Fe_3O_4. The presence of a strong H-O-H stretching band centered around 3385 cm^{-1} and a weak H-O-H bending vibration at 1631 cm^{-1} indicates that the Fe_3O_4-MNPs are hydrated.

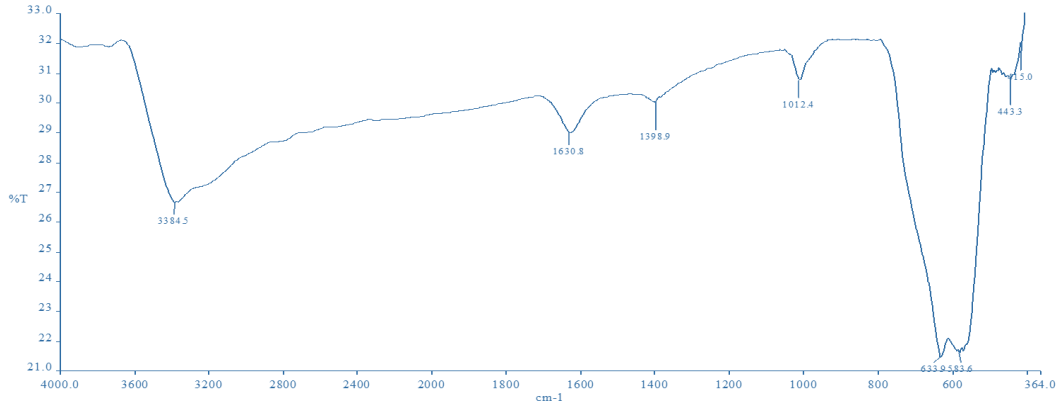

Figure 27. IR spectrum of hydrated Fe_3O_4-MNPs.

A representation of the structure of Fe_3O_4-MNPs is shown in Figure 28.

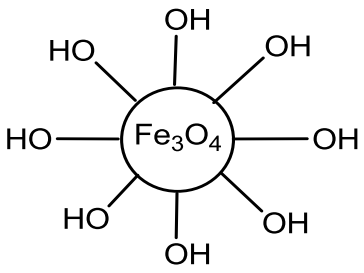

Figure. 28. A schematic representing the structure of Fe_3O_4-MNPs (incorporated H_2O molecules not shown).

The surface morphology of Fe_3O_4-MNPs was studied using SEM (Figure 29). The lower magnification image shows smooth surfaces with sharp, angular, stepped ledges throughout, while images taken under higher magnification reveal a rough, rippled surface and angular ledges.

SEM images of Fe_3O_4-MNPs from literature sources[130,131] (Figure 30) appear to have less apparent agglommeration at the lower magnification (10 µm). A dimpled surface is visible at the 50 nm magnification. Variations in synthetic protocol such as the speed of mechanical stirring used during synthesis may account for these differences[132].

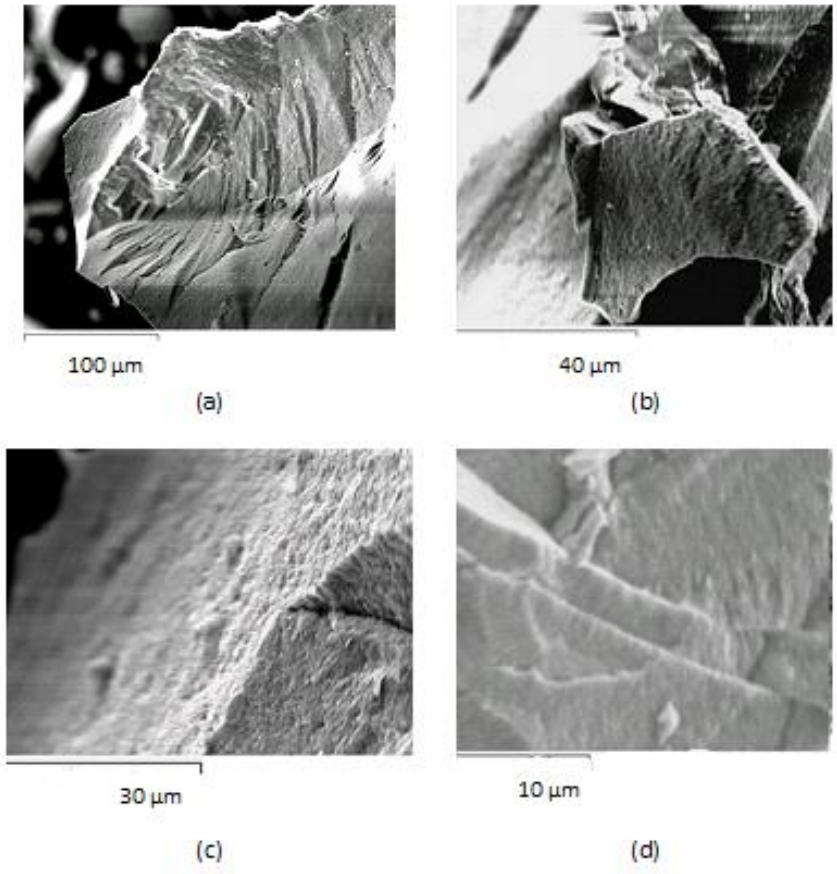

Figure 29. SEM images of Fe_3O_4-MNPs (synthesised in the present study) at various magnifications: (a) 100 µm, (b) 40 µm, (c) 30 µm and (d) 10 µm.

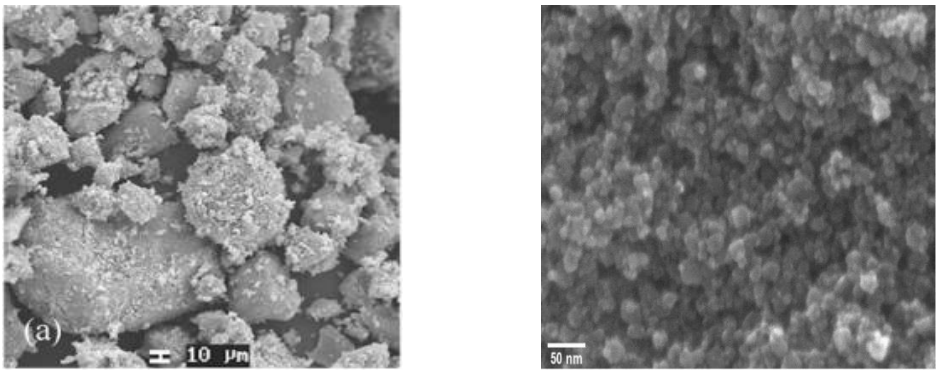

(a) (b)

Figure 30. SEM images of Fe_3O_4-MNPs (a) 10 µm[130], and (b) at high magnification 50 nm[131].

When making small molecules, a distribution of sizes is generally obtained[43]. Aggregation of the uncoated, bare Fe_3O_4-MNPs prepared in the present study is observed in the TEM images shown in Figure 31. Such agglomeration is normally to be expected as there were no surfactants present during sample preparation[133]. Individual nanoparticles of <20 nm are visible in Figure 31 (b) at a magnification of X600,000 at 100 kV.

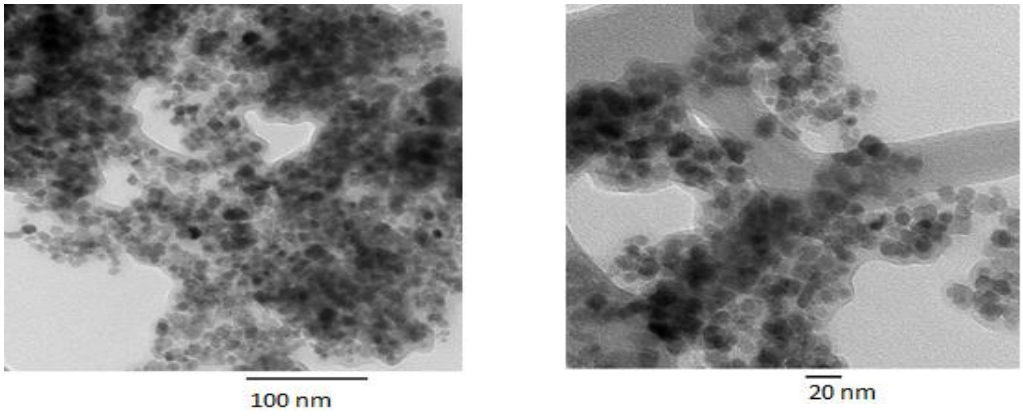

(a) (b)

Figure 31. TEM images of Fe_3O_4-MNPs synthesised in the present work at magnifications of (a) 100 nm and (b) 20 nm. (Hitachi H7650. 100 kV).

The TEM images obtained for the Fe_3O_4-MNPs particles prepared in the present study are comparable to images available from the literature[56] (Figure 32 (a)) and from commercial sources[134] (Figure 32 (b)).

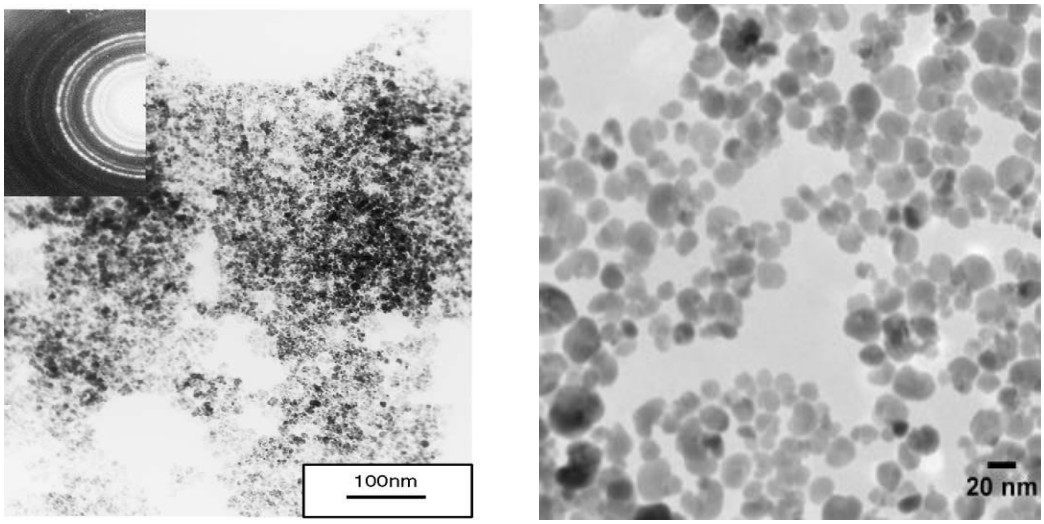

(a) (b)

Figure 32. TEM and Selected Area Electron Diffraction (SAED) image of (a) Fe_3O_4-MNPs[56], and (b) high magnification TEM image of Fe_3O_4-MNPS from a commercial website[134].

3.2 pAPTES Materials

3.2.1 pAPTES

Emulating the literature method[24] of stirring mAPTES in water at room temperature gave colourless pAPTES in high yield. Although microanalytical data for pAPTES (found: C 26.48%, H 6.76%, N 9.40%) corresponded well with those reported in the literature[135,136,129], the % elemental composition values were substantially lower than those calculated for a pure polymer of formula $(C_3H_8NSiO_{3/2})_n$ (calc.: C 32.70%, H 7.32%, N 12.71%). The found %C:%N ratio of 2.8:1 for the present sample of pAPTES was slightly higher than that calculated (%C:%N = 2.6:1) for the propylamine functionality in pure pAPTES, suggesting the presence of some extra carbon-

containing species in the pAPTES sample. Indeed, the ^{1}H NMR spectrum of the material (discussed below) confirmed the presence of a small quantity of ethyl moieties in the sample, possibly due to trapped ethanol from the washing procedure and/or ethoxy groups from some unreacted mAPTES.

The IR spectrum of pAPTES (Figure 33) shows the characteristic broad band (1200-900 cm^{-1}) associated with the Si-O-Si linkage[145]. The relatively broad bands (3600-3200 and 1700-1500 cm^{-1}) arise from H-O-H and H-N-H stretching and H-O-H and H-N-H bending vibrations[195] respectively, indicating that there is some trapped water and ethanol molecules (see discussion of ^{1}H NMR spectrum) in the pAPTES matrix.

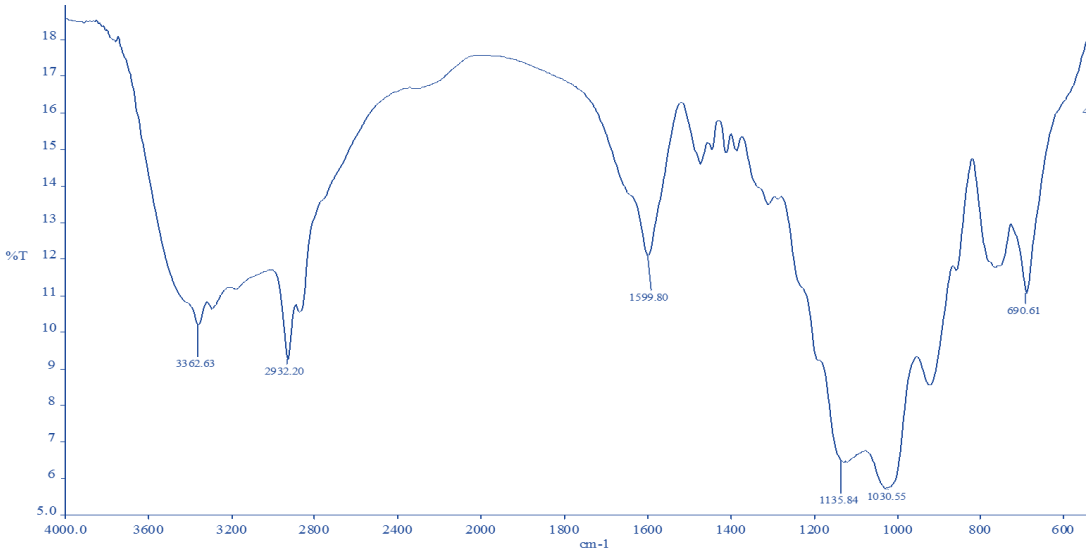

Figure 33. IR spectrum of pAPTES.

The ^{1}H NMR (D_2O solution) spectrum of pAPTES (Figure 34) shows multiplets at *ca*. 0.5, 1.6 and 2.8 ppm for H_a, H_b and H_c, respectively. A triplet and a quartet centred at *ca*. 1.05 and 3.55 ppm indicated the presence of a relatively small quantity of ethyl

moieties in the sample, arising from ethanol washing of the product and/or some unreacted mAPTES (discussed above).

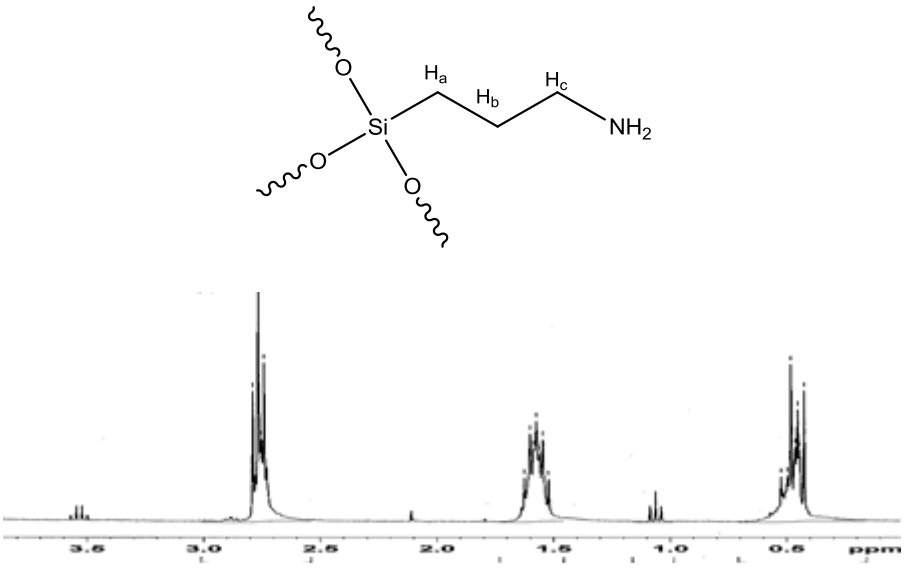

Figure 34. ^{1}H NMR (D_2O) spectrum of pAPTES.

A schematic representing the structure of pAPTES is shown in Figure 35.

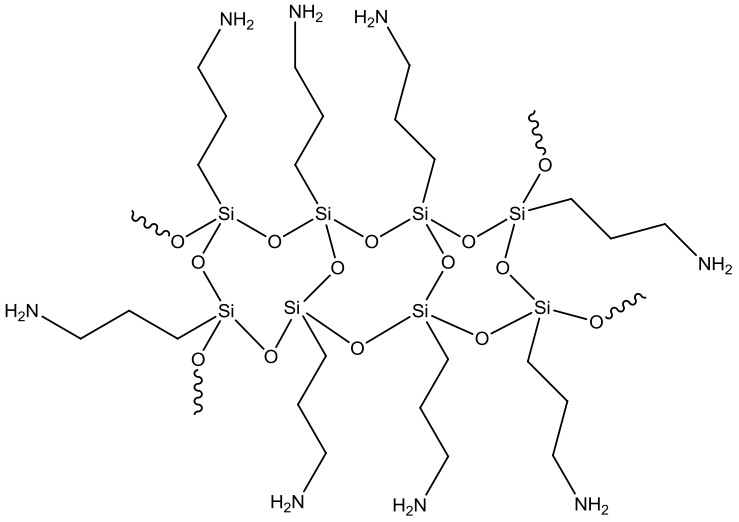

Figure 35. A schematic representing the structure of pAPTES.

SEM images of pAPTES are shown in Figure 36 and reveal a relatively smooth, cheese-like surface morphology. Some bubbling is visible on the block-like polymers which probably arises during solvent removal under high vacuum.

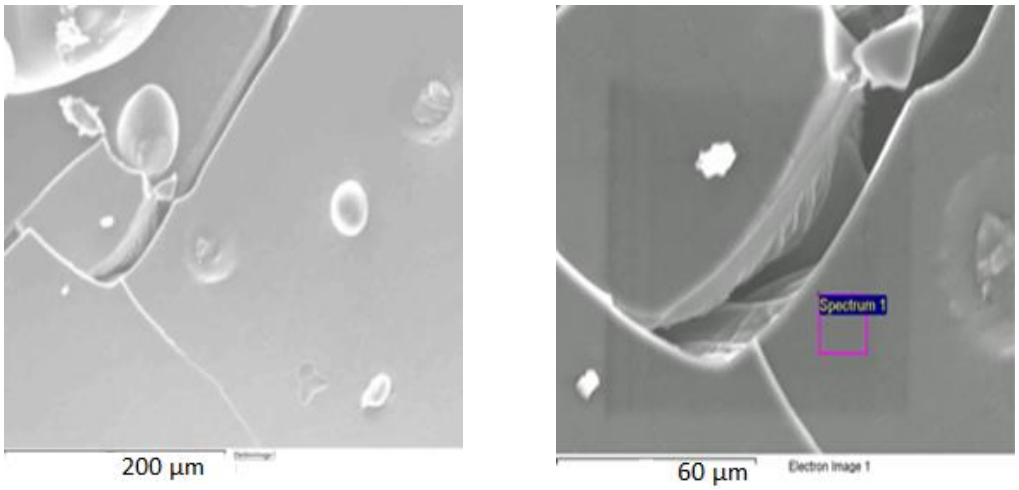

Figure 36. SEM images of pAPTES under (a) low magnification and (b) high magnification.

3.2.2 pAPTES-Fe_3O_4-MNPs

Following a literature procedure[49], black pAPTES-Fe_3O_4-MNPs were made by treating a suspension of Fe_3O_4-MNPs in aqueous ethanol with mAPTES (*ca.* 2.3:1 mole ratio). It is known that when Fe_3O_4 magnetic nanoparticles are dispersed in an aqueous medium the surface $Fe^{2+/3+}$ and O^{2-} ions would adsorb OH^- and H^+ ions, respectively, from self-dissociated H_2O molecules (Scheme 1)[52]. Addition of mAPTES to water promotes hydrolysis, ethanol elimination and formation of $(OH)_3Si(CH_2)_3NH_2$. Surface -OH moieties on the Fe_3O_4-MNPs can condense with the –OH groups on $(OH)_3Si(CH_2)_3NH_2$ molecules to form Fe-O-Si bonds (Scheme 2). Subsequent condensation of neighboring HO-Si functions creates interconnected -O-Si-O-Si-

linkages and a polymeric silicone surface coating on the nanoparticles. A schematic representation of the structure of pAPTES-Fe_3O_4-MNPs is shown in Figure 37.

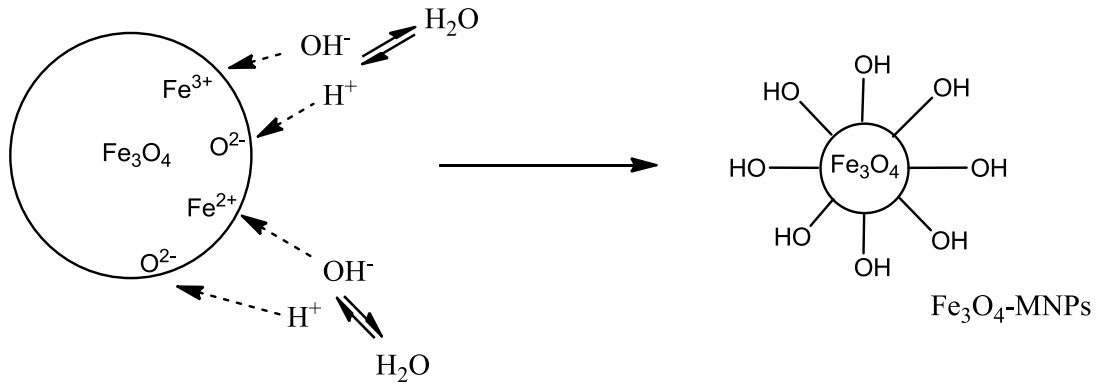

Scheme 1. Formation of surface –OH moieties on Fe_3O_4-MNPs.

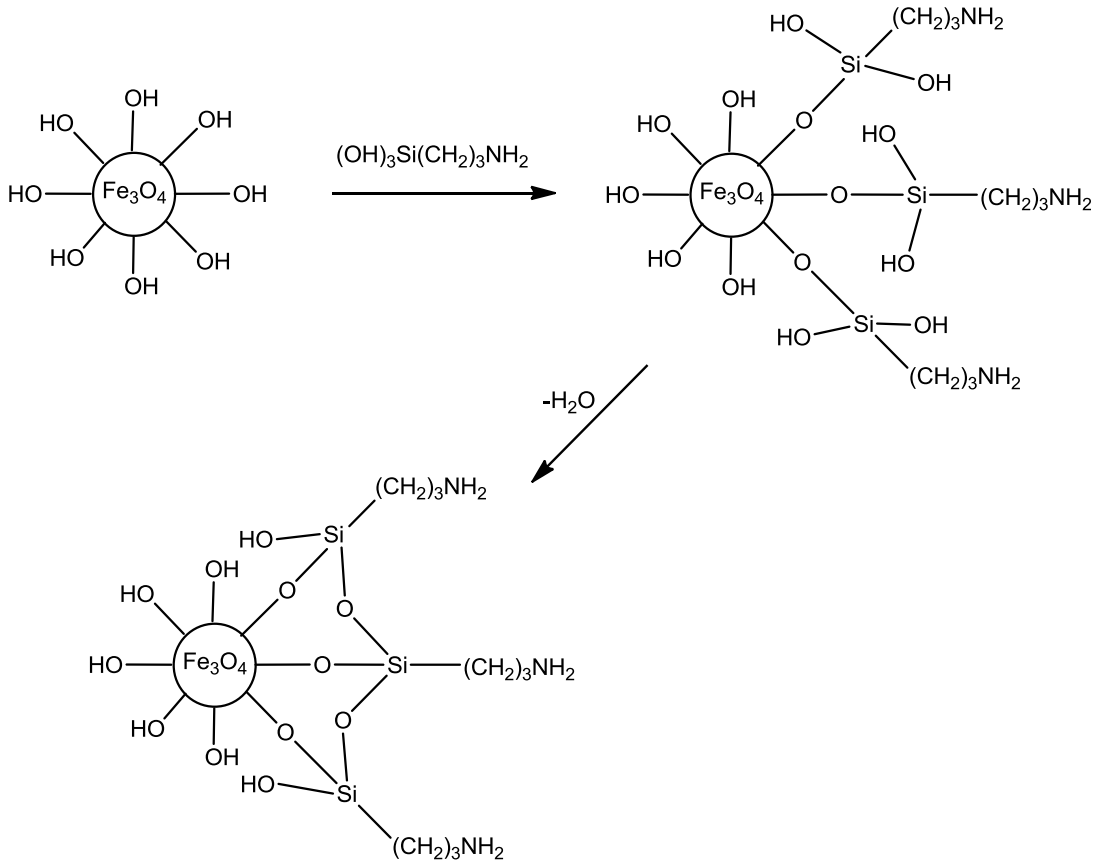

Scheme 2. Schematic for formation of pAPTES-Fe_3O_4-MNPs.

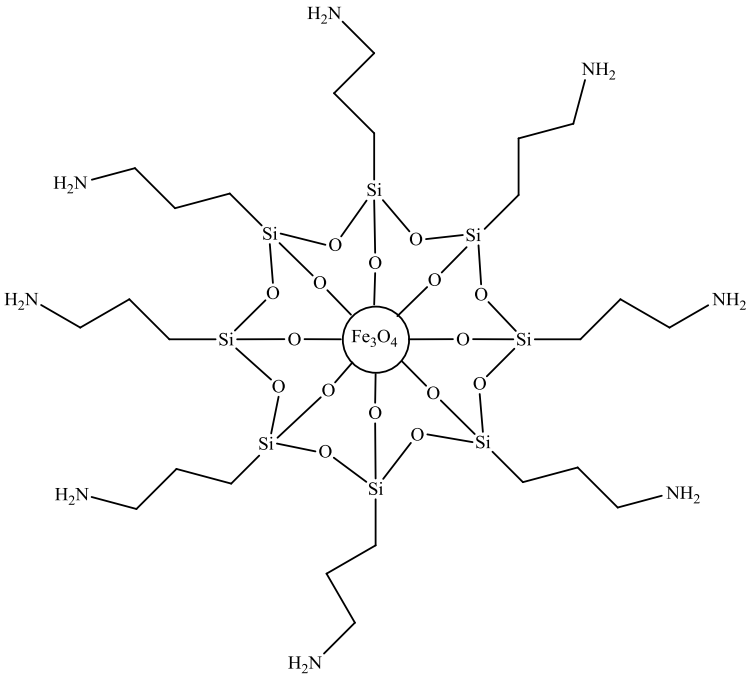

Figure 37. Representation of the structure of pAPTES-Fe_3O_4-MNPs.

As expected, the carbon, hydrogen and nitrogen elemental mass composition percentages of these elements in pAPTES-Fe_3O_4-MNPs (found: C 1.90%; H 0.70%, N 0.39%), which arise from the propylamine functionality in the silicone coating on the nanoparticles, were significantly less than those in pAPTES (found: C 26.48%, H 6.76%, N 9.40%). This is confirmation that the polymer surface coating in pAPTES-Fe_3O_4-MNPs represents only a very small proportion of the sample bulk. The finding that the %C:%N ratio in pAPTES (2.8:1) is appreciably less than that in pAPTES-Fe_3O_4-MNPs (4.87:1), suggests that there may be some non-hydrolysed EtO-Si units from mAPTES and/or retention of ethanol (from washings) in the latter material, even after prolonged desiccation. These are the only other possible source of additional C atoms in the sample which are required to align the high %C:%N ratio. If it is assumed that EtOH is the source of additional C atoms then theoretical calculation show that,

on average, *ca.* 1 EtOH is present for each aminopropyl moiety in pAPTES-Fe_3O_4-MNPs (gives a %C:%N ratio of 4.29:1)

The IR spectrum of the polymer-coated pAPTES-Fe_3O_4-MNPs (Figure 38) is very similar to that of the uncoated, hydrated Fe_3O_4-MNPs (Figure 27), with the most prominent bands being associated with the H-O-H (3404, 1625 cm^{-1}) and Fe-O (800-400 cm^{-1}) vibrations. By comparing the IR spectrum of pAPTES (Figure 33) with that of pAPTES-Fe_3O_4-MNPs the occurrence of relatively weak Si-O-Si bands (1150-900 cm^{-1}) confirms the presence of the silicone coating in the latter sample. As the amount of silicone coating on the surface of the nanoparticles is extremely small in comparison to the bulk quantity of Fe_3O_4-MNPs (confirmed by microanalytical and EDX data) the weak C-H stretching bands (*ca.* 2900 cm^{-1}) and the H-N-H stretching and bending bands associated with the aminopropyl function were not clearly discernible in the pAPTES-Fe_3O_4-MNPs spectrum. The IR spectra of Fe_3O_4-MNPs and pAPTES-Fe_3O_4-MNPs for the samples prepared in the present study were very similar to those published by Ma *et al*. for the same materials[52].

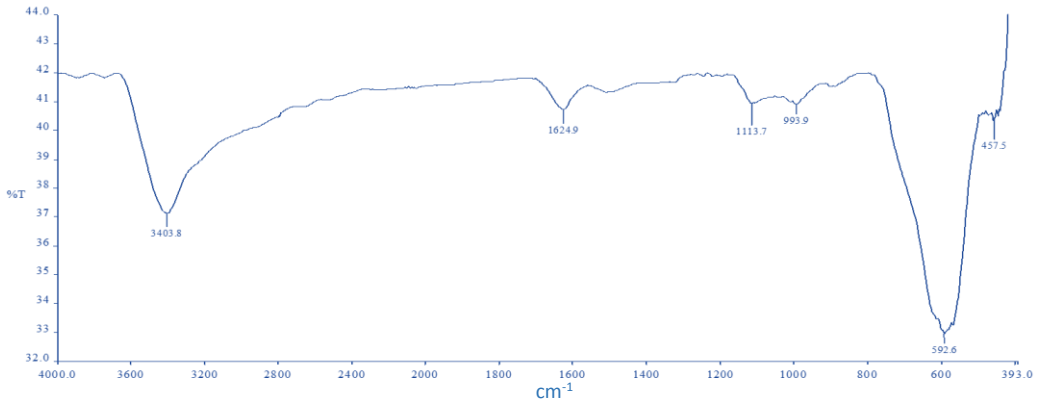

Figure 38. IR spectrum of pAPTES-Fe_3O_4-MNPs.

The surface morphology of pAPTES-Fe_3O_4-MNPs was imaged using SEM (Figure 39). The sample shows both smooth and granular surfaces.

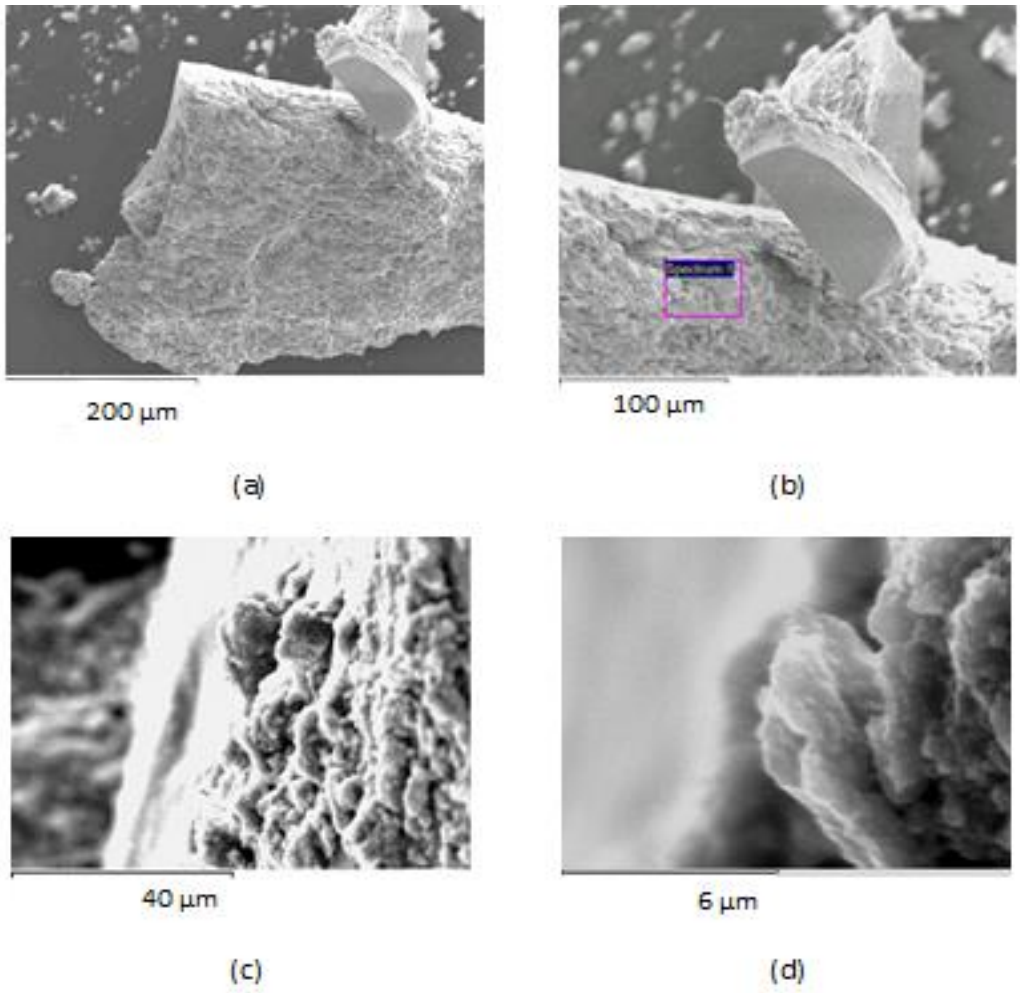

Figure 39. SEM images of pAPTES-Fe_3O_4-MNPs. Images (c) and (d) are higher magnifications of the rippled regions.

TEM images of pAPTES-Fe_3O_4-MNPs, synthesised in the present study, (Figure 40) show particles of <10 nm in diameter which are well formed and with little apparent

agglomeration. These TEM images are very similar to those available from literature sources (Figure 41).

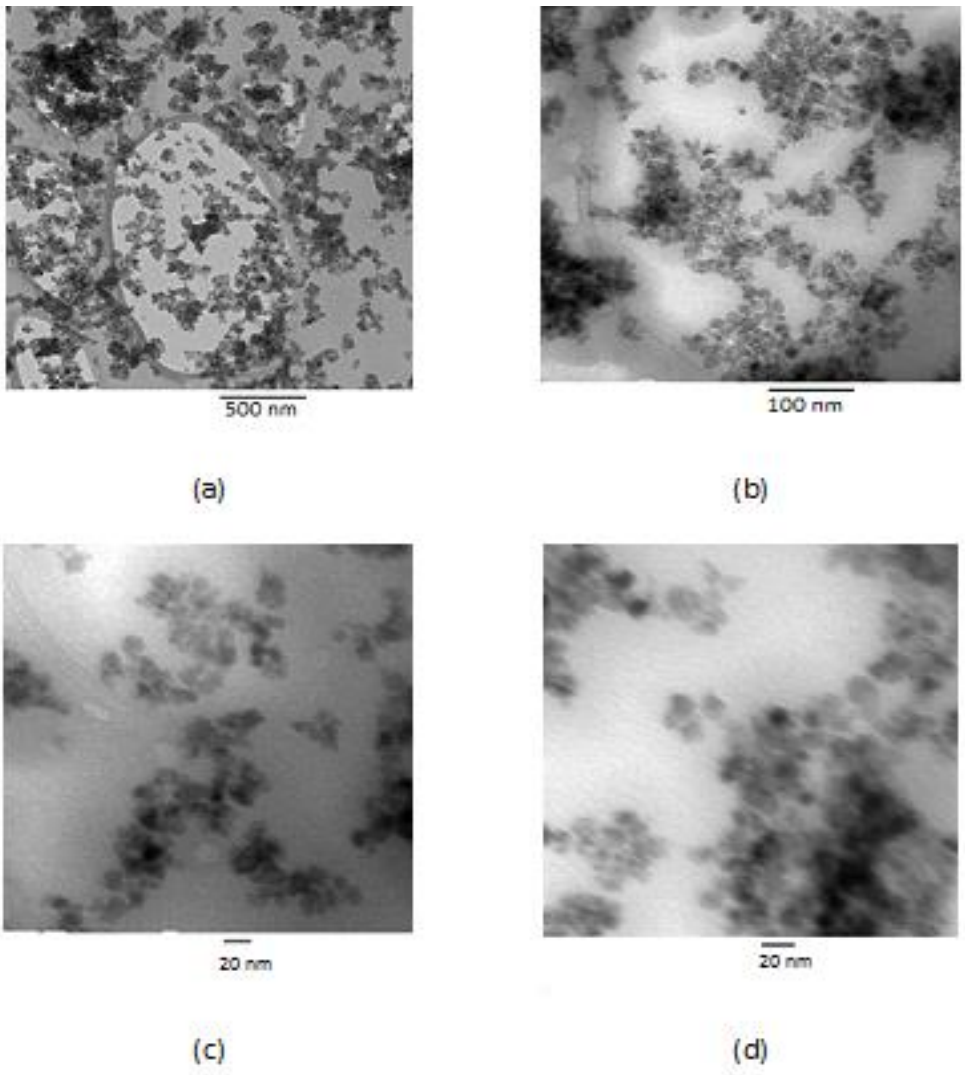

Figure 40. TEM images of pAPTES-Fe_3O_4-MNPs at magnification of (a) 500 nm (b) 100 nm (c) 20 nm (d) 20 nm (Hitachi H7650. 100 kV).

Tem images are very similar to those available from literature sources (Figure 41).

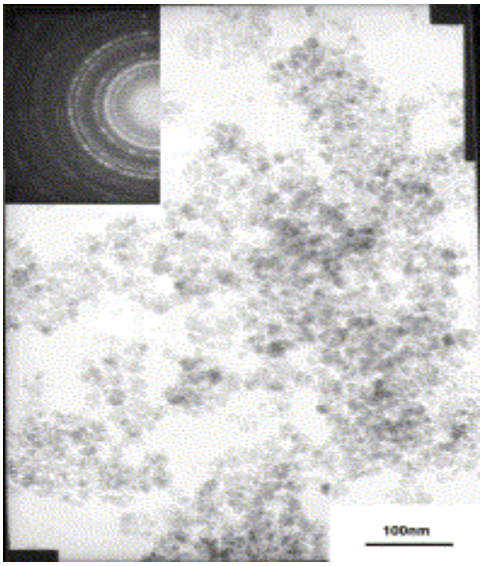

Figure 41. TEM image of pAPTES-Fe_3O_4-MNPs from a literature source[52].

A qualitative EDX spectrum of pAPTES-Fe_3O_4-MNPs (Figure 42) confirmed the presence of silicon on the surface of the nanoparticles. An approximate surface coverage of APTES on the Fe_3O_4-MNPs was calculated at 37%, a value that is slightly less than that reported in the literature[52]. This is indicative of a near-monolayer surface coating of silicone-polymer on the surface of the Fe_3O_4-MNPs.

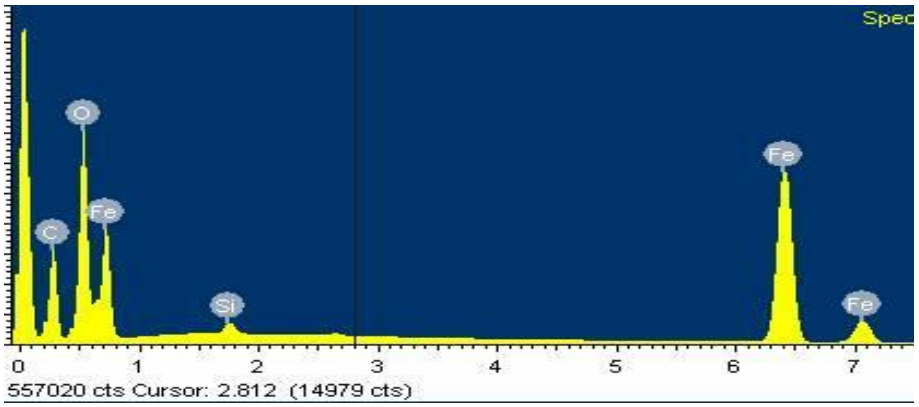

Figure 42. EDX spectrum of pAPTES-Fe_3O_4-MNPs.

3.2.3 [$(NO_3)_2$Cu-pAPTES]

[$(NO_3)_2$Cu-pAPTES] was synthesised using a modified literature procedure[129]. Royal blue, glass-like flakes of [$(NO_3)_2$Cu-pAPTES] formed in good yield upon addition of $Cu(NO_3)_2.3H_2O$ to mAPTES in water in a *ca*. 2.2:1 mole ratio. The IR spectrum of the product (Figure 43) shows characteristic bands for water and -NH_2 functions (3700-3100 and 1700-1600 cm^{-1}), aliphatic C-H (2930 cm^{-1}), NO_3^- (1384 cm^{-1}) and Si-O-Si moieties (1200-900 cm^{-1}).

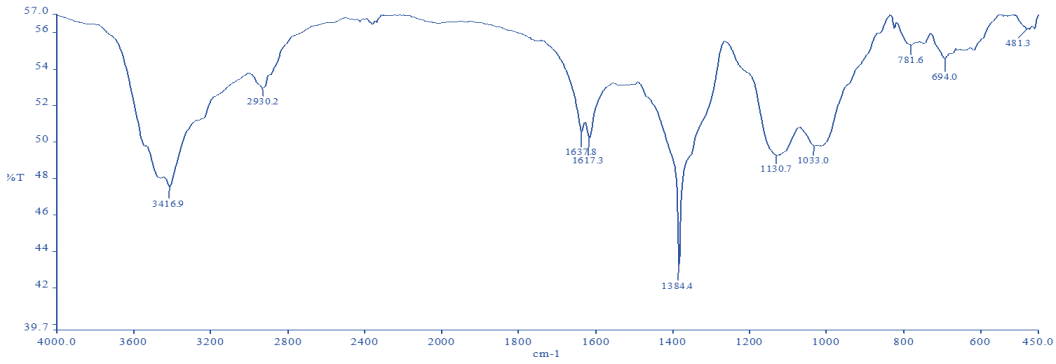

Figure 43. IR spectrum of [$(NO_3)_2$Cu-pAPTES].

The hydrated [$(NO_3)_2$Cu-pAPTES] sample returned microanalytical data (found: C 18.53%, H 4.35%, N 10.52%) which gave a %C:%N ratio of 1.76:1. To achieve this %C:%N ratio it has been calculated that, on average, there are *ca.* 4.5 -$CH_2CH_2CH_2NH_2$ moieties for every 1 $Cu(NO_3)_2$ within solid [$(NO_3)_2$Cu-pAPTES] (gives a theoretical %C:%N ratio of 1.78:1). If a tentative assumption is made that there is a homogeneous distribution of Cu(II) ions throughout the solid, then in some instances there are 4 $CH_2CH_2CH_2NH_2$ moieties coordinated (by the amine N atom) to the metal centre,

whilst at other sites there could be 5 $CH_2CH_2CH_2NH_2$ coordinated to the metal. A schematic representing one of the possible structural formats of $[(NO_3)_2Cu\text{-}pAPTES]$ is given in Figure 44.

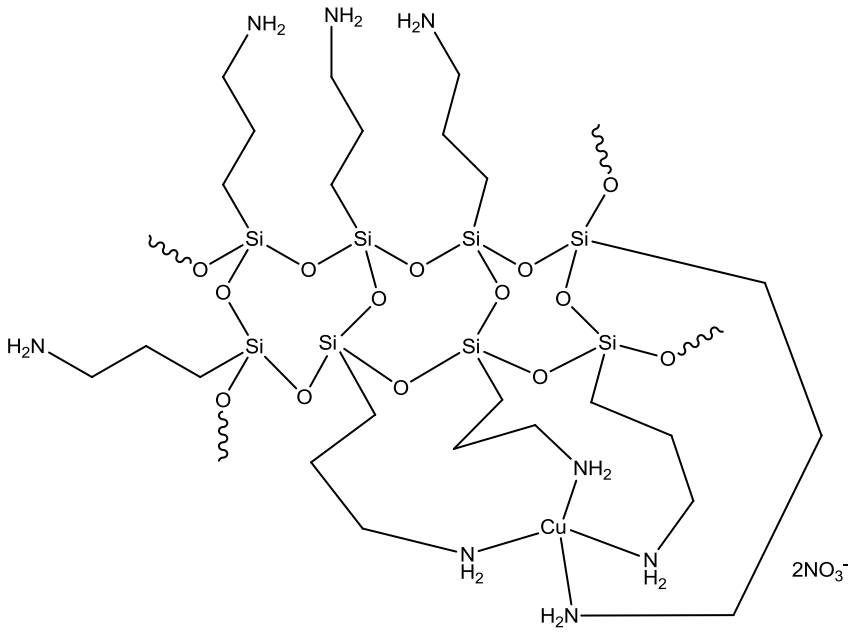

Figure 44. Schematic representation of one of the possible structural forms of $[(NO_3)_2Cu\text{-}pAPTES]$.

The surface morphology of $[(NO_3)_2Cu\text{-}pAPTES]$ obtained from the current study was imaged using SEM (Figure 45). The images show smooth blocks of polymer with some cracks on the surface. Pitting is visible on the lower magnification image (a) below, while the image take at higher magnification (b) has white flecks of copper visible on the surface.

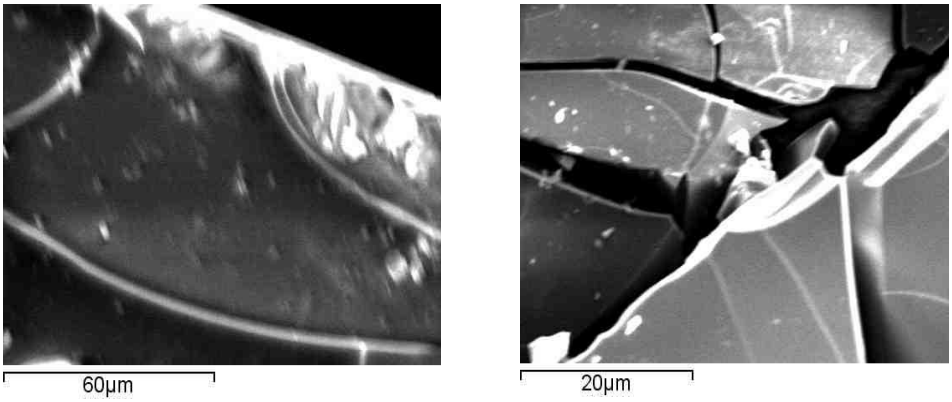

(a) (b)

Figure 45. SEM images of [$(NO_3)_2$Cu-pAPTES] under (a) low magnification and (b) high magnification.

The SEM images obtained from the current study are similar to those reported by Owens[129] (Figure 46), which have a block-like morphology with some cracks apparent. The image under high magnification (10 µm) reveals ridges.

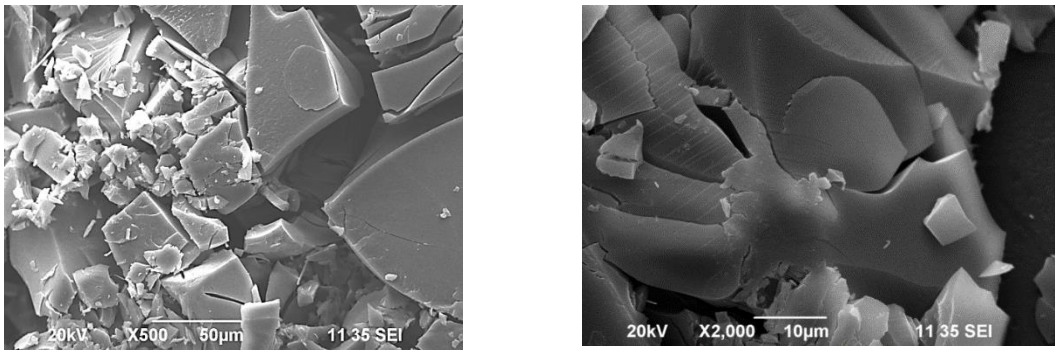

Figure 46. SEM images of p(APTES)Cu reported by Owens under (a) low magnification and (b) high magnification[129]. The sample was prepared using a 5:1 mole ratio of $Cu(NO_3)_2$:mAPTES.

The presence of copper(II) ions on the surface of the sample was confirmed by EDX (Figure 47).

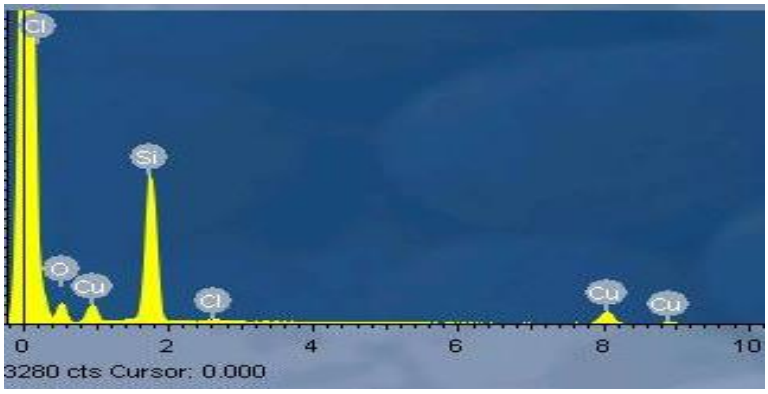

Figure 47. EDX spectrum of $[(NO_3)_2Cu\text{-}pAPTES]$.

3.2.4 $[(OAc)_2Cu\text{-}pAPTES\text{-}Fe_3O_4\text{-}MNPs]$

Suspended black $pAPTES\text{-}Fe_3O_4\text{-}MNPs$ (0.15 g) were reacted with an ethanolic solution of $[Cu_2(OAc)_4(H_2O)_2]$ (0.05 g) to give black $[(OAc)_2Cu\text{-}pAPTES\text{-}Fe_3O_4\text{-}MNPs]$. The apparent low mass yield (0.03 g) can principally be attributed to loss of solid during product recovery operations. The very finely dispersed powdery material did not settle fully throughout the numerous sedimentation/magnetic decantation process.

As in the case of $pAPTES\text{-}Fe_3O_4\text{-}MNPs$ (Figure 38), the IR spectrum of $[(OAc)_2Cu\text{-}pAPTES\text{-}Fe_3O_4\text{-}MNPs]$ (Figure 48 (a)) is dominated by strong H-O-H and Fe-O bands (centred around 3422 and 600 cm^{-1}, respectively). Very weak bands are present for the C-H and O-Si-O moieties (2923 and 1200-1000 cm^{-1}, respectively). The acetate O-C-O asymmetric vibration band is thought to be masked by the broad H-O-H/H-N-H

bending band centred around 1632 cm^{-1}, whilst the weak, sharp band at 1385 cm^{-1} could be due to the O-C-O symmetric stretch.

Note that in the IR spectrum of $[Cu_2(OAc)_4(H_2O)_2]$ **(**Figure 48 (b)), the prominent O-C-O asym and O-C-O sym bands occur at 1602 and 1445 cm^{-1}, respectively.

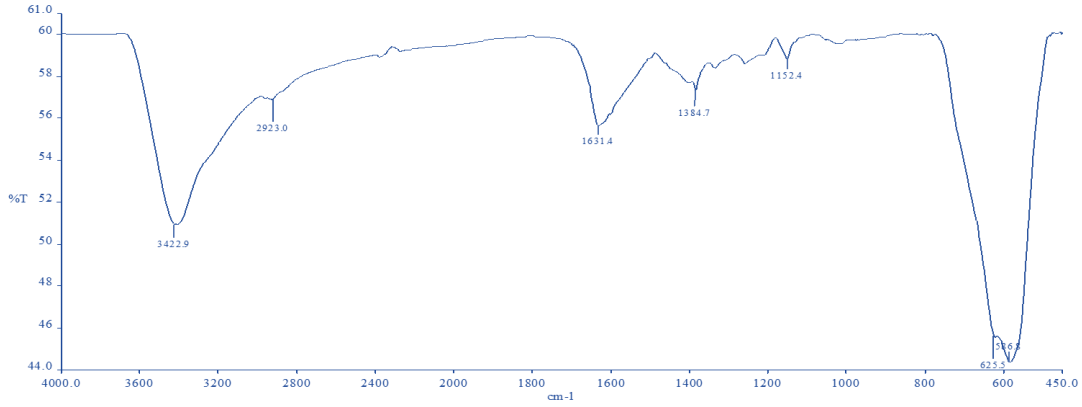

(a)

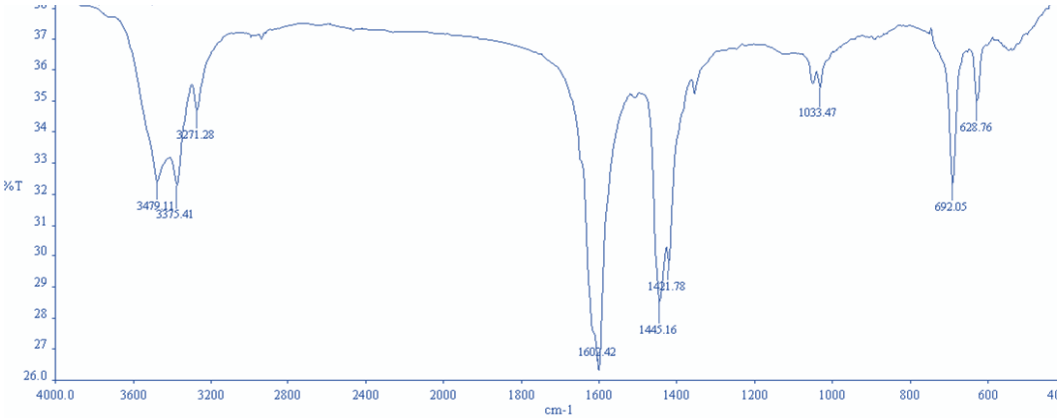

(b)

Figure 48. IR spectra of (a) $[(OAc)_2Cu\text{-}pAPTES\text{-}Fe_3O_4\text{-}MNPs]$, and (b) $[Cu_2(OAc)_4(H_2O)_2]$.

Microanalytical data for hydrated $[(OAc)_2Cu\text{-}pAPTES\text{-}Fe_3O_4\text{-}MNPs]$ (found: C 1.63%, H 0.41%, N 0.29%: %C:%N ratio = 5.62:1) returned, an average, 1 $CH_2CH_2CH_2NH_2$ moiety for every 1 $Cu(OAc)_2$ on the polymer-coated solid surface (this gives a theoretical

%C:%N ratio of 6.0:1). Again, if there is a tentative assumption of a homogeneous distribution of Cu(II) ions throughout the surface silicone coating, then the coordination environment around each Cu(II) centre could comprise two bidentate acetates and one propylamine, as illustrated in Figure 49.

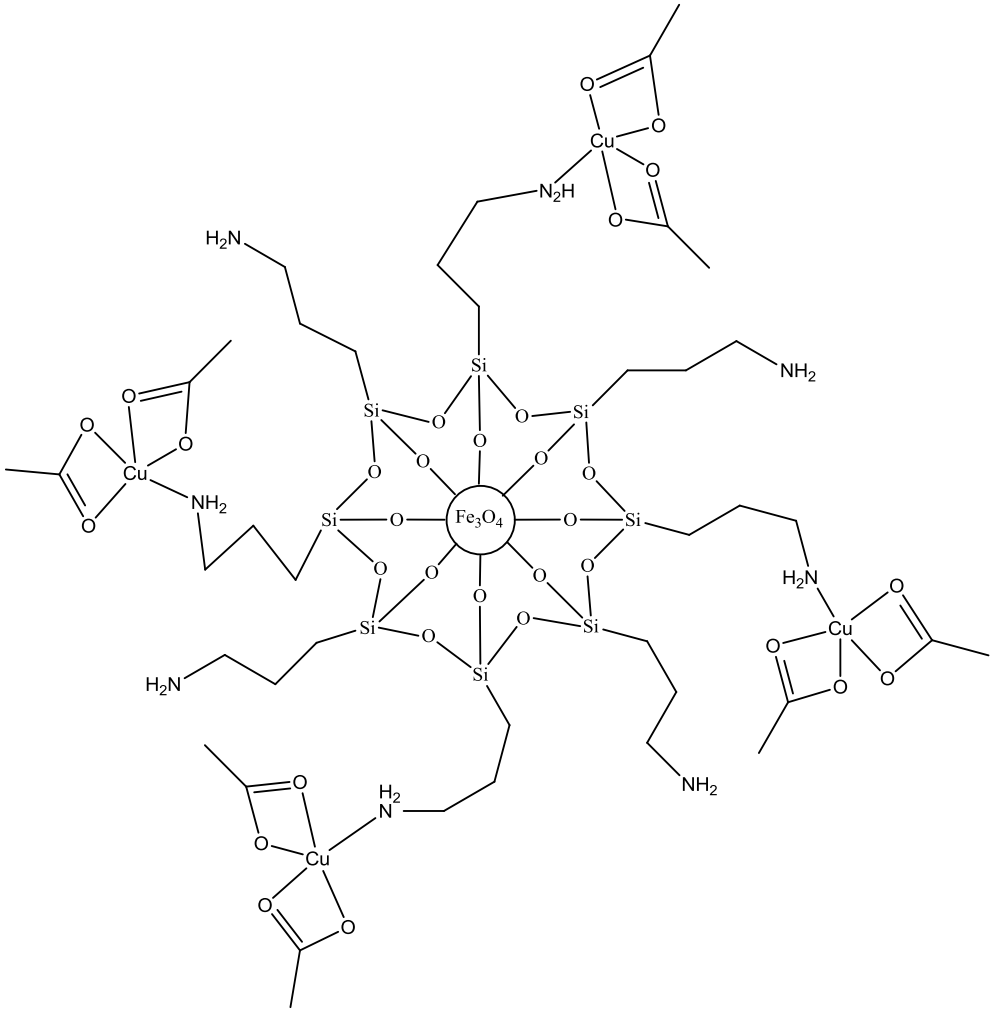

Figure 49. Schematic representation of one of the possible structural forms of [$(OAc)_2$Cu-pAPTES-Fe_3O_4-MNPs]**.**

SEM images of [$(OAc)_2$Cu-pAPTES-Fe_3O_4-MNPs] (Figure 50) reveal a smooth surface, and one which was much more flaky than pAPTES (Figure 36). [$(OAc)_2$Cu-pAPTES-

Fe_3O_4-MNPs] was also devoid of the external rippling apparent on the Fe_3O_4-MNPs (Figure 29) and pAPTES-Fe_3O_4-MNPs (Figure 39) samples.

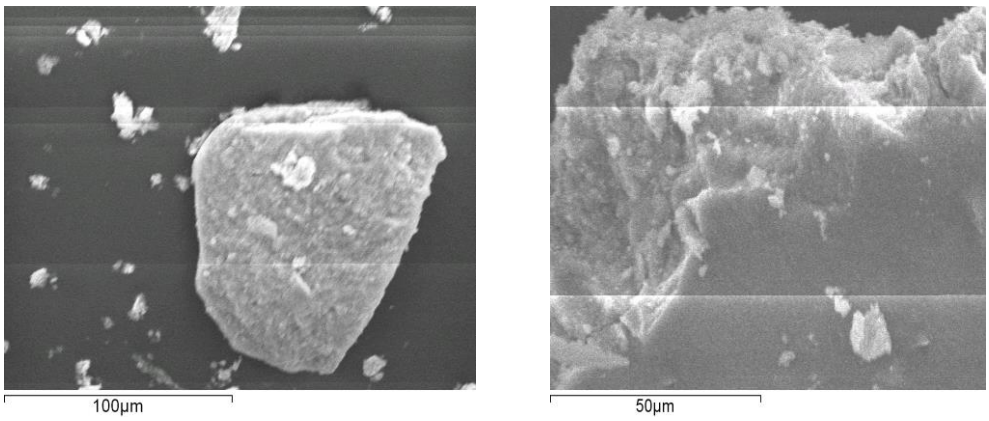

(a) (b)

Figure 50. SEM images of [$(OAc)_2$Cu-pAPTES-Fe_3O_4-MNPs] under (a) low magnification and (b) high magnification.

A qualitative EDX spectrum of [$(OAc)_2$Cu-pAPTES-Fe_3O_4-MNPs] (Figure 51) confirmed the presence of surface iron, copper, silicon and oxygen. As expected, the copper content is very small in relation to the amount of surface iron.

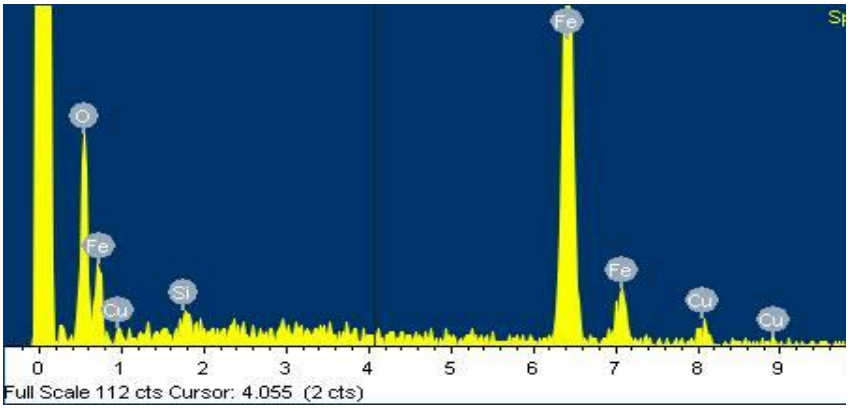

Figure 51. EDX spectrum of [$(OAc)_2$Cu-pAPTES-Fe_3O_4-MNPs].

3.2.5 SalH-pAPTES

Addition of salicylaldehyde (SalH) to neat mAPTES, (*ca.* 1:1 mole ratio) afforded the yellow solid, SalH-pAPTES. The strong C=O stretching band (1666 cm^{-1}) that was present in the IR spectrum of SalH was absent from the spectrum of SalH-pAPTES (Figure 52). The latter material gave a prominent C=N band at 1634 cm^{-1}, indicating formation of the Schiff base. The broad band spanning the region 1200-900 cm^{-1} verified the creation of O-Si-O linkages in the polymer product.

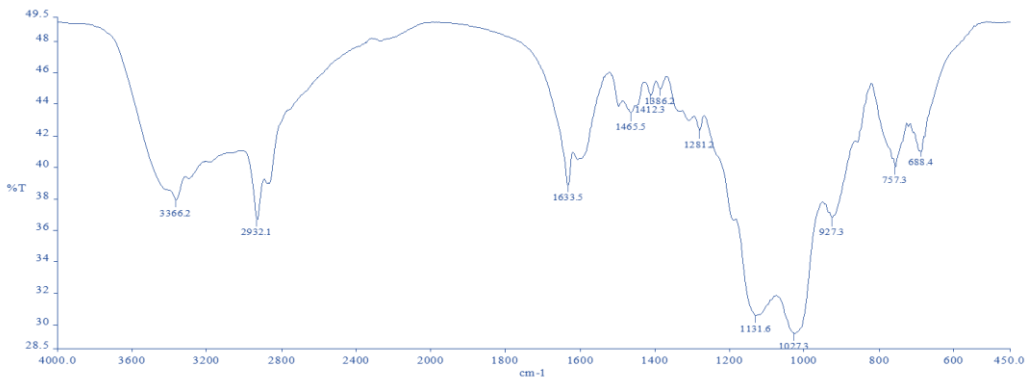

Figure 52. IR spectrum of SalH-pAPTES made using mAPTES.

Addition of salicylaldehyde to preformed pAPTES also produced a yellow solid, the IR spectrum of which (Figure 53) was quite similar to that given by the SalH-pAPTES sample formed using mAPTES. Again, the absence of a C=O band implied that the polymer was free from unreacted aldehyde.

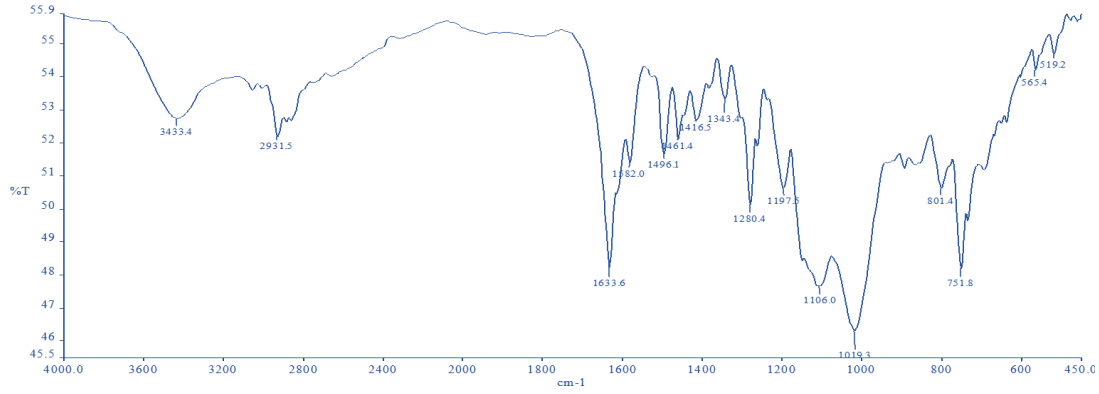

Figure 53. IR spectrum of SalH-pAPTES made using pAPTES.

If it is assumed that all mAPTES has been converted into pAPTES in the SalH + mAPTES reaction, and that there are no encapsulated EtOH (liberated during the hydrolysis of silane monomer molecules) or EtOH molecules (from the product washing process), then microanalytical data for the product (found: C 31.79%, H 6.57%, N 9.80%; %C:%N = 3.24:1) suggests that *ca.* one in every nine pendant $–CH_2CH_2CH_2NH_2$ functions of the silicone polymer has undergone a Schiff base condensation reaction with salicylaldehyde to give a $–CH_2CH_2CH_2N=CH(C_6H_3–OH)$ moiety (gives a %C:%N ratio of 3.24:1), as depicted in Figure 54. It is not known if there is a homogeneous distribution of the Schiff base residues throughout the product.

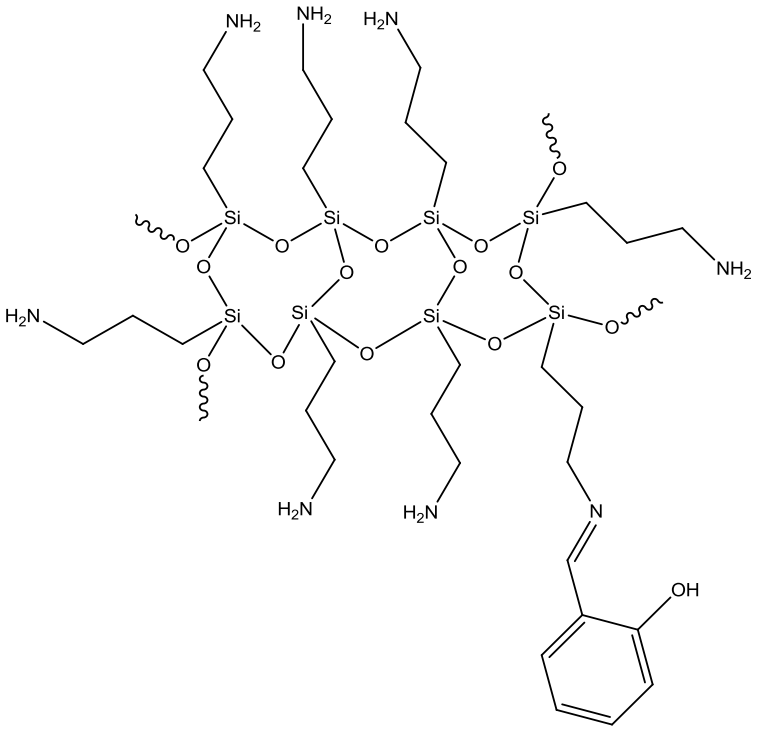

Figure 54. Schematic representation of the structure of SalH-pAPTES.

Surprisingly, when Sing *et al.*[137] refluxed a 1:1 mole mixture of SalH and mAPTES in MeOH only the Schiff base product formed with the monomer (SalH-mAPTES) and there was no mention of any Schiff base polymeric silicon material being produced at this stage (Scheme 3, Step(i)), even though they describe that the product of this reaction was a viscous, yellow material. This result appears somewhat strange given the fact that water, which is a stoichiometric by-product in a Schiff base condensation reaction, is known to promote the rapid hydrolysis of mAPTES and that this hydrolysed monomer, $(OH)_3SiCH_2CH_2CH_2NH_2$, readily oligomerizes/polymerises. Furthermore, these authors also found that subsequent refluxing of their SalH-mAPTES compound with copper(II) acetate gave the complex, [Cu-Sal-$(mAPTES)_2$], in which the Cu(II) ion was coordinated by two deprotonated ligands (Scheme 3, Step(ii)). Silane polymerization only occurred when [Cu-Sal-$(mAPTES)_2$] was refluxed

with the pre-calcined silica, Si-MCM 41, giving [Cu-Sal-(mAPTES)$_2$-Si-MCM 41] (Scheme 3, Step(iii)).

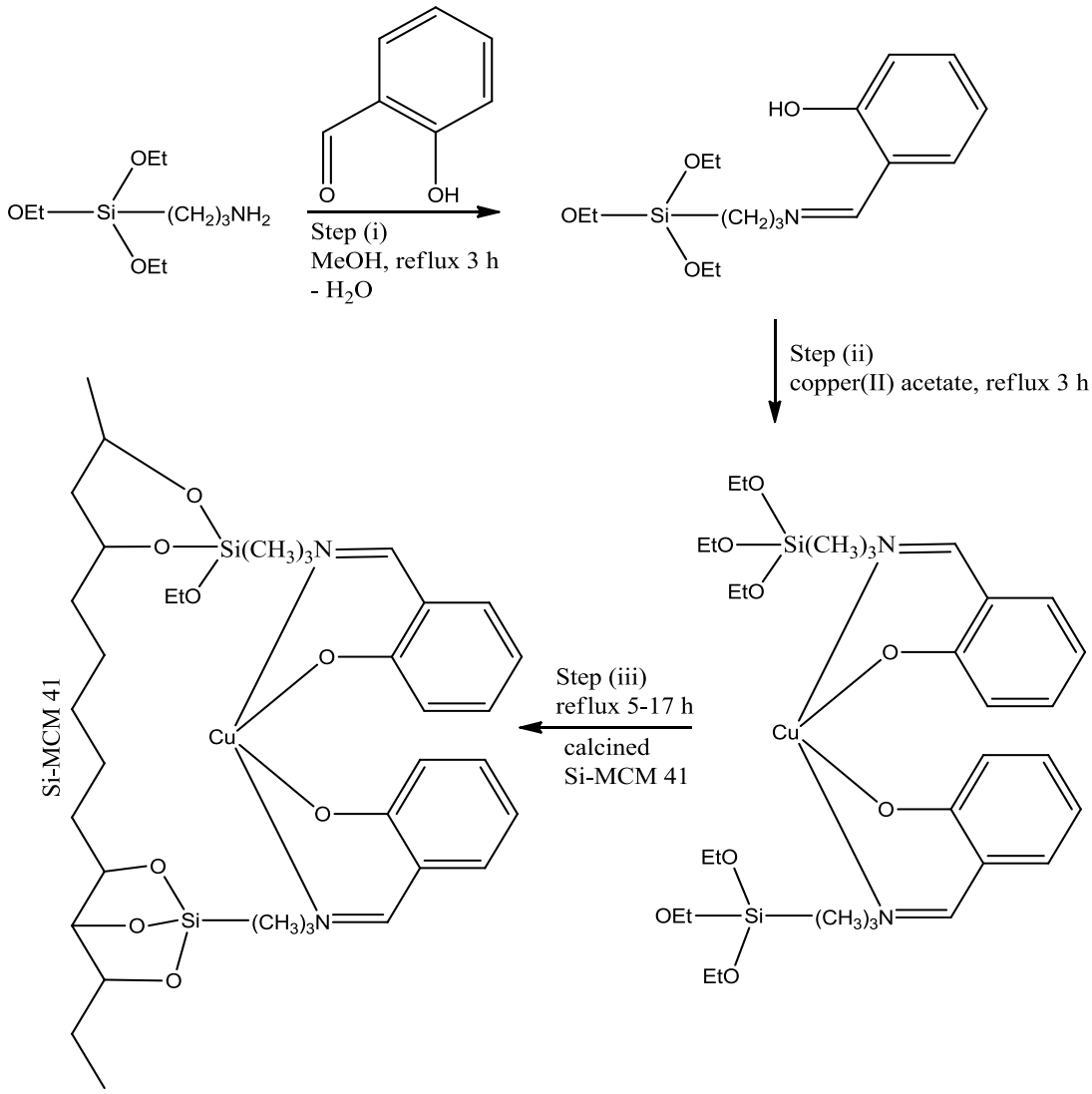

Scheme 3. Synthesis of the Cu(II)-Schiff base [Cu-Sal-(mAPTES)$_2$-Si-MCM 41][137].

SEM images of SalH-pAPTES made from SalH + mAPTES (Figure 55) and from SalH + pAPTES (Figure 56) indicate that surface morphology is dependent upon the synthetic protocol employed. The sample prepared using mAPTES has a rippled texture whilst that obtained using pAPTES has a somewhat flaky consistency.

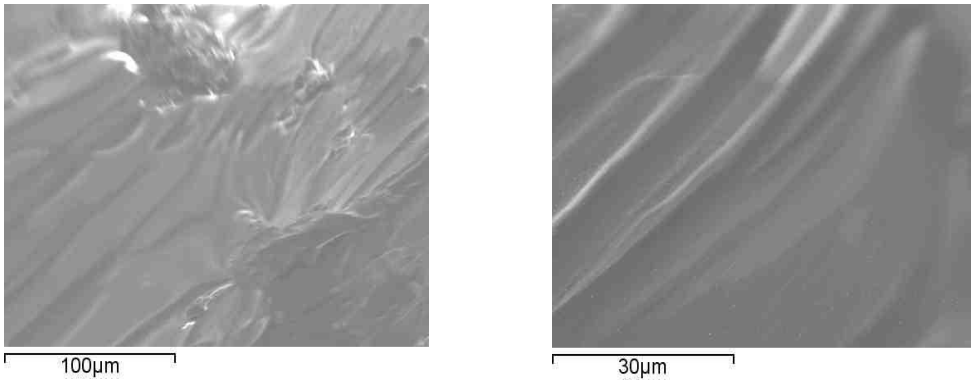

(a) (b)

Figure 55. SEM images of the SalH-pAPTES sample made from SalH + mAPTES under (a) low magnification and (b) high magnification.

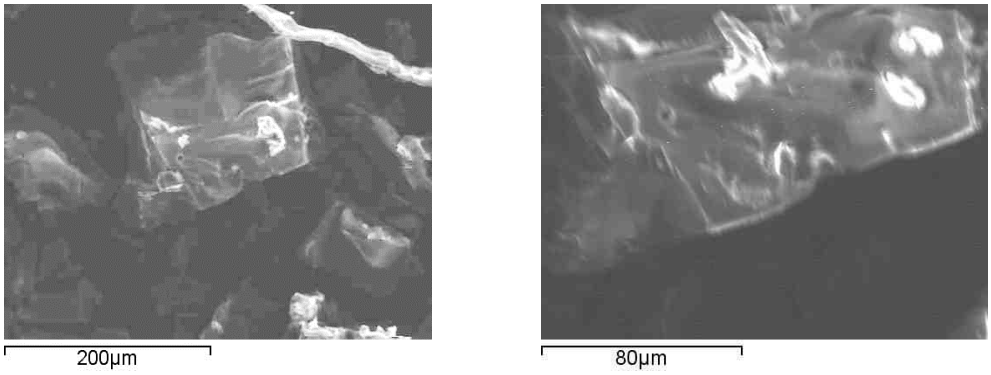

(a) (b)

Figure 56. SEM images of the SalH-pAPTES sample made from SalH + pAPTES under (a) low magnification and (b) high magnification.

3.2.6 SalH-pAPTES-Fe_3O_4-MNPs

Addition of salicylaldehyde to an ethanolic suspension of pAPTES-Fe_3O_4-MNPs (*ca.* 1:2 mass ratio) gives the brown powder, SalH-pAPTES-Fe_3O_4-MNPs. The IR spectrum of the material (Figure 57) is very similar to that of the precursor solid, pAPTES-Fe_3O_4-

MNPs (Figure 38) and bands attributable to the salicylate moiety (e.g. aromatic C-H and C-C ring vibrations) are not clearly recognisable.

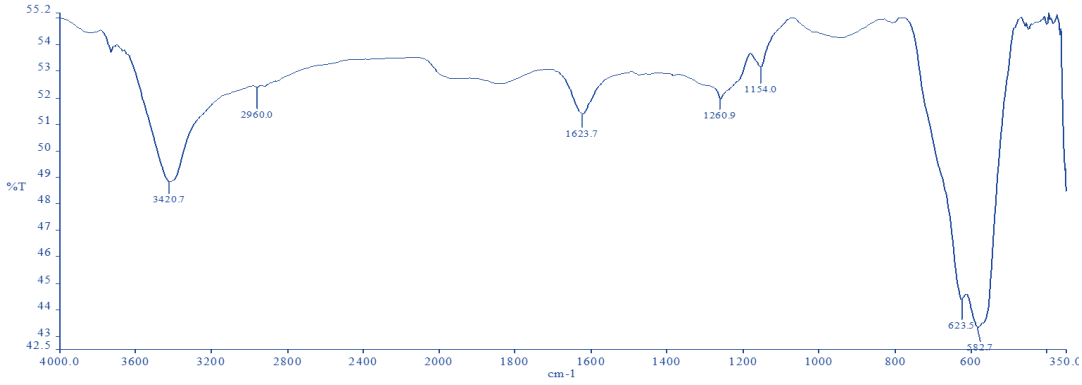

Figure 57. IR spectrum of SalH-pAPTES-Fe_3O_4-MNPs.

Microanalytical data for SalH-pAPTES-Fe_3O_4-MNPs (found: C 3.25%, H 0.47%, N 0.08%) translates to a very large %C:%N ratio of 40.6:1. If all of the pendant propylamine functions on pAPTES-Fe_3O_4-MNPs had undergone a Schiff base condensation reaction then the theoretical %C:%N ratio should be 5.6:1. Given the extremely high %C:%N ratio found for SalH-pAPTES-Fe_3O_4-MNPs (40.6:1), the extra carbon content presumably comes from large quantities of EtOH (reaction and washing solvent used) tightly bound in the polymer matrix. Theoretical calculations show that, on average, for each pendant $–CH_2CH_2CH_2N=CH(C_6H_3–OH)$ moiety then 22 EtOH molecules must be added to give a %C:%N ratio of 46.39:1. However, if solid SalH-pAPTES-Fe_3O_4-MNPs contained such a large quantity of EtOH then it would be anticipated that a reasonably pronounced aliphatic C-H stretching band (*ca.* 2900 cm^{-1}) would be visible in the IR spectrum of the sample. This was not the case. Figure 58 shows only one of a number of structural possibilities for SalH-pAPTES-Fe_3O_4-MNPs (trapped EtOH molecules not included).

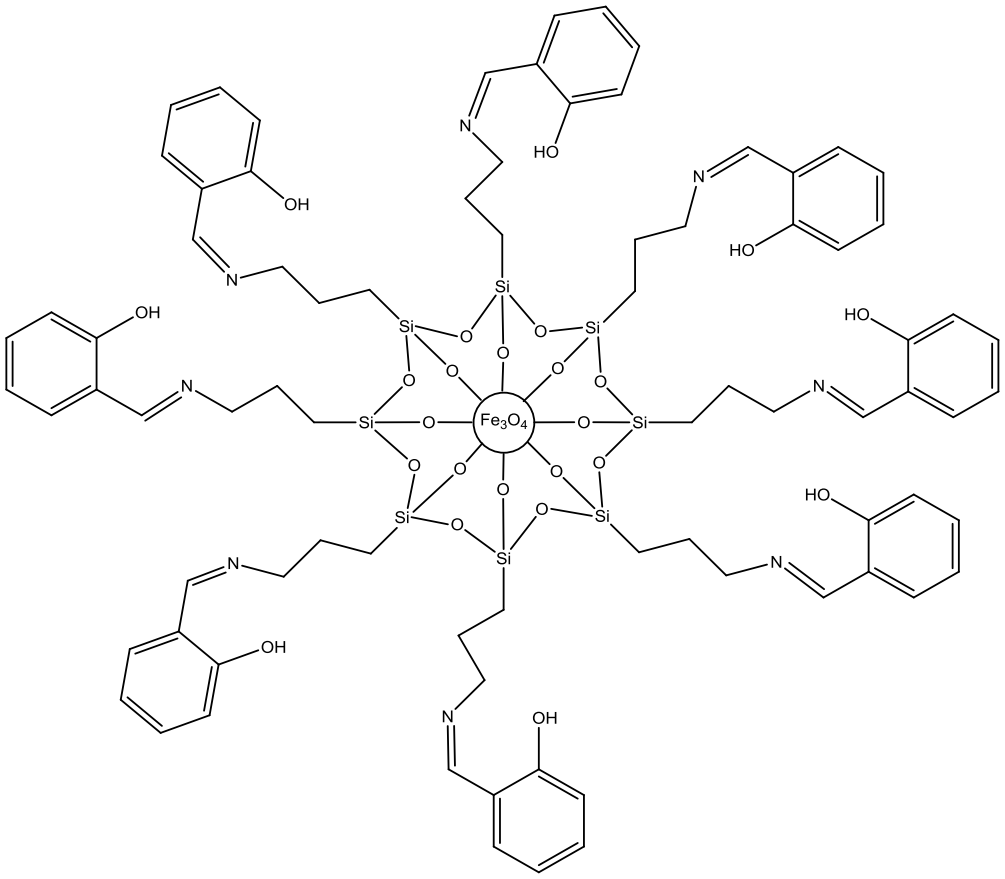

Figure 58. Schematic illustration of one of a number of structural possibilities for SalH-pAPTES-Fe_3O_4-MNPs.

At low magnification, SEM images of SalH-pAPTES-Fe_3O_4-MNPs (Figure 59) show an irregular, rough surface, which bore some resemblance to the surface of pAPTES-Fe_3O_4-MNPs (Figure 39). At higher magnification, it became evident that the SalH-pAPTES-Fe_3O_4-MNPs surface was constituted by a loose assembly of small particles of various shapes and sizes.

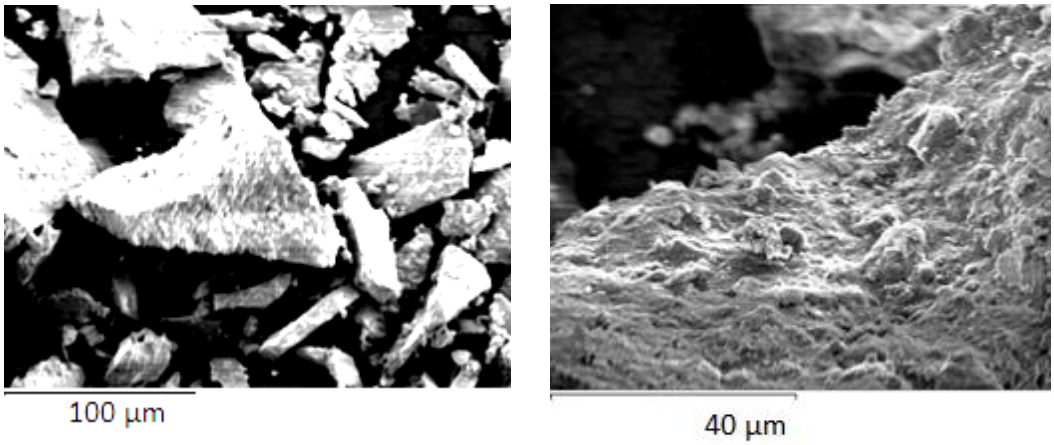

(a) (b)

Figure 59. SEM images of SalH-pAPTES-Fe_3O_4-MNPs under (a) low magnification dn (b) high magnification.

3.2.7 [Cu-Sal-pAPTES-Fe_3O_4-MNPs]

Addition of $[Cu_2(OAc)_4(H_2O)_2]$ to an ethanolic suspension of brown SalH-pAPTES-Fe_3O_4-MNPs (0.05 g:0.12 g mass ratio) gave a relatively low mass yield (0.08 g) of [Cu-Sal-pAPTES-Fe_3O_4-MNPs], which was also a brown powder. In addition to strong H-O-H (3402 and 1567 cm^{-1}), Si-O-Si (1300-1000 cm^{-1}) and Fe-O (750-450 cm^{-1}) bands, the IR spectrum of the product (Figure 60) also contained relatively weak aliphatic C-H and imine C=N stretching bands (2918 and 1626 cm^{-1}, respectively). Likewise, Sing *et al*.[137] reported C-H and C=N bands at essentially identical wavenumbers in the spectrum of their Cu(II) Schiff base polymer, [Cu-Sal-$(mAPTES)_2$-Si-MCM 41] (see Scheme 3).

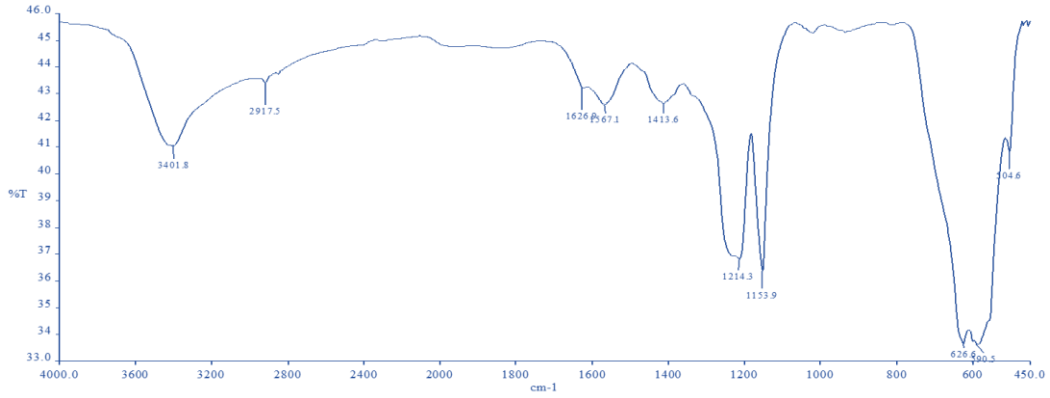

Figure 60. IR spectrum of [Cu-Sal-pAPTES-Fe_3O_4-MNPs].

For [Cu-Sal-$(mAPTES)_2$-Si-MCM 41], which was also derived using copper(II) acetate, Singh *et al.*[137] indicated that charge balance for the encapsulated Cu^{2+} dications was provided by deprotonated phenolic oxygens from two salicylate residues, and not by acetate anions (Figure 53). Acetic acid will be the by-product formed upon combination of the released phenolic H^+ ions with $CH_3CO_2^-$ ions. Metal coordination by the imine N and the phenolic O atoms gives stable, six-membered chelate rings. This is also thought to be the case with [Cu-Sal-pAPTES-Fe_3O_4-MNPs]. Support for this bonding comes from the fact that IR bands attributable to acetate O-C-O stretching were not evident in the spectra of [Cu-Sal-pAPTES-Fe_3O_4-MNPs] and [Cu-Sal-$(mAPTES)_2$-Si-MCM 41][137].

Surprisingly, microanalytical data for [Cu-Sal-pAPTES-Fe_3O_4-MNPs] (found: C 1.22%, H 0.23%, N 0.17%) revealed a dramatic reduction in the %C:%N ratio (7.18:1) compared to the precursor material, SalH-pAPTES-Fe_3O_4-MNPs (40.6:1), where there are thought to be *ca.* 22 EtOH molecules trapped per pendant –$CH_2CH_2CH_2N{=}CH(C_6H_3{-}OH)$ group. For [Cu-Sal-pAPTES-Fe_3O_4-MNPs], the established

7.18:1 %C:%N ratio is close to the theoretical value calculated (8.57:1) for a material in which the only carbon and nitrogen atoms present in the sample come from the –$CH_2CH_2CH_2N{=}CH(C_6H_3{-}OH)$ moiety (i.e. the EtOH molecules trapped in SalH-pAPTES-Fe_3O_4-MNPs are lost upon conversion to [Cu-Sal-pAPTES-Fe_3O_4-MNPs]). A structural schematic for one of a number of possible structures of [Cu-Sal-pAPTES-Fe_3O_4-MNPs] is given in Figure 61.

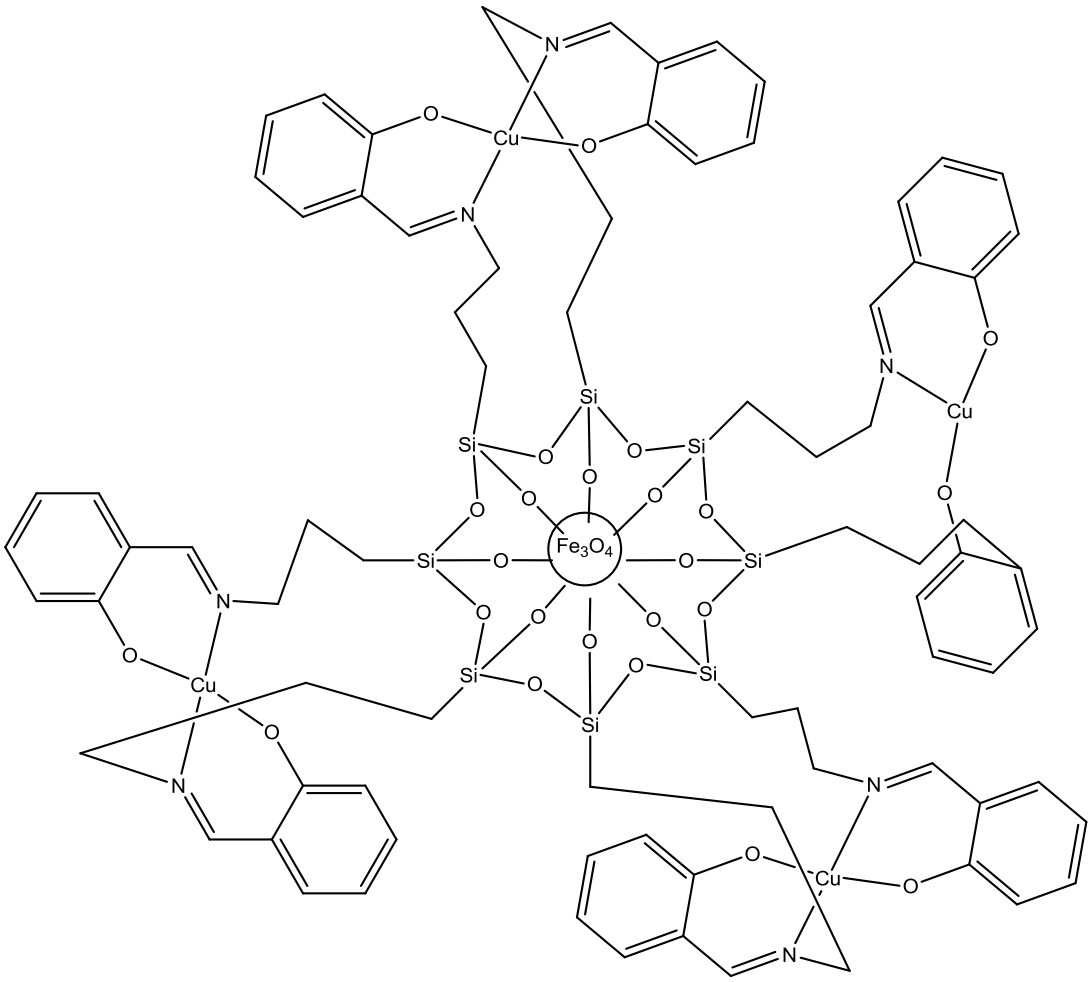

Figure 61. Schematic diagram of one possible structure for [Cu-Sal-pAPTES-Fe_3O_4-MNPs].

SEM images of [Cu-Sal-pAPTES-Fe_3O_4-MNPs] (Figure 62) show particles which have a relatively smooth outer top layer and a rougher edge topography. At the higher magnification (50 µm scale), the surface texture appears to be smoother than its precursor material, SalH-pAPTES-Fe_3O_4-MNPs (Figure 57), which is undoubtedly attributable to the presence of chelated Cu(II) ions and the absence of trapped EtOH molecules in the material.

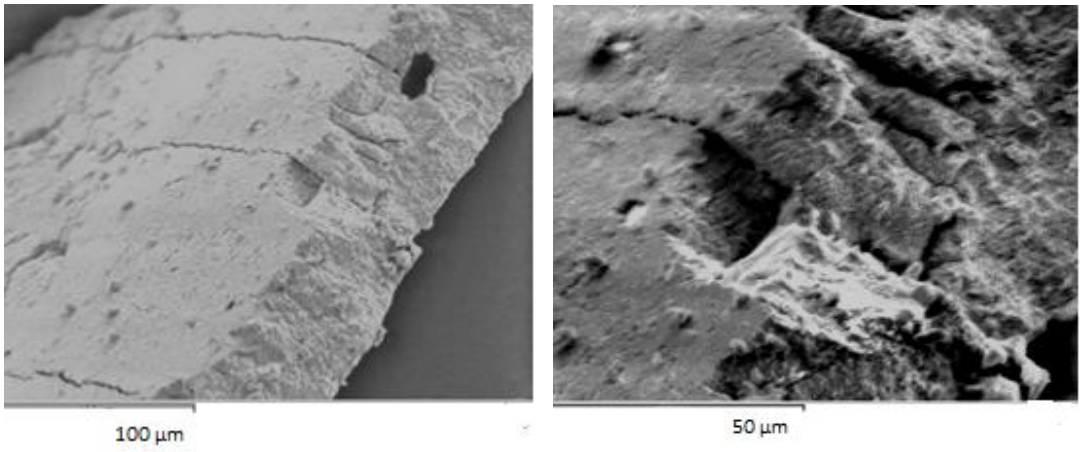

(a) (b)

Figure 62. SEM images of [Cu-Sal-pAPTES-Fe_3O_4-MNPs].

A qualitative EDX spectrum of [Cu-Sal-pAPTES-Fe_3O_4-MNPs] (Figure 63) confirmed the presence of surface iron, copper, silicon and oxygen. As expected, the Cu(II) content appeared to be quite small.

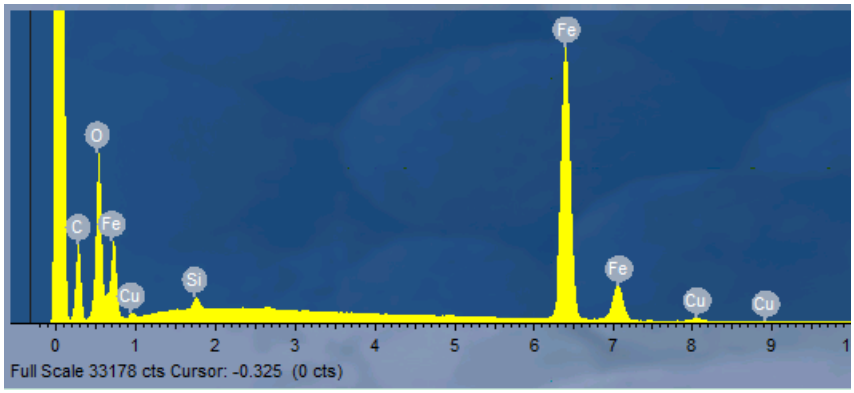

Figure 63. EDX spectrum of [Cu-Sal-pAPTES-Fe_3O_4-MNPs].

3.3 pTMSPDT Materials

3.3.1 pTMSPDT

As outlined in the established literature procedures[138,139], hydrolysis and subsequent condensation of mTMSPDT occurs in aqueous media at room temperature to give the colourless pTMSPDT solid in good mass yield. Although microanalytical data (found: C 39.04%, H 8.16%, N 18.06%; %C:%N = 2.16:1) correlated well with that reported by Owens[129] (found: C 39.42%, H 8.33%, N 17.73%; %C:%N = 2.22:1) the elemental composition values were significantly less than those predicted by the theoretical calculations for pure pTMSPDT of formulation $(C_7H_{18}N_3SiO_{3/2})_n$ (calc.: C 42.83%, H 9.24%, N 21.40%; %C:%N = 2.00:1). This was the same scenario as that witnessed in the case of pAPTES. The larger %C:%N ratio found for the synthesised pTMSPDT sample (2.22:1) infers incorporation of methanol in the solid (can arise from hydrolysis of methoxy groups on the monomer and/or the reaction/washing solvent). Theoretical calculations show that for each pendant $-(CH_2)_3NH(CH_2)_2NH(CH_2)_2NH_2$

moiety there is, on average, *ca.* 1 MeOH molecule present (gives a %C:%N ratio of 2.29:1).

The IR spectrum of pTMSPDT (Figure 64) was very similar to that of pAPTES (Figure 33) and contained bands associated with trapped water and the various structural moieties constituting the polymer matrix (to avoid unnecessary repetition, band frequencies are not discussed here but these are outlined in the Experimental Section).

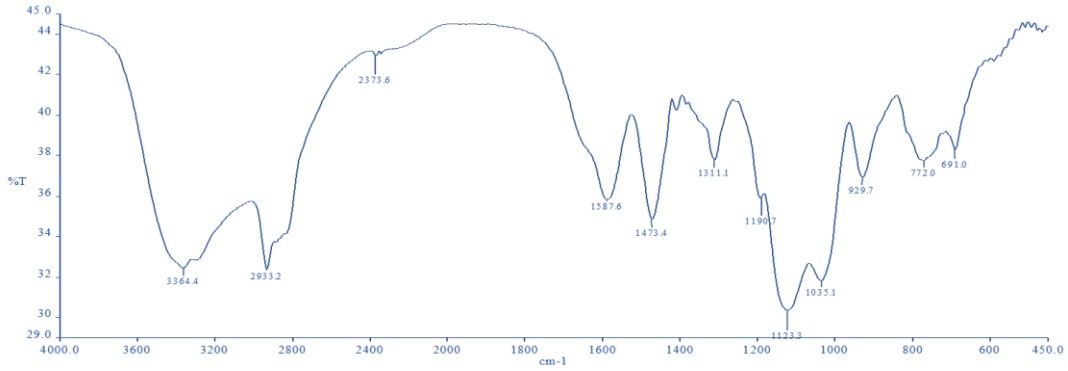

Figure 64. IR spectrum of pTMSPDT.

The somewhat weak ^{1}H NMR (D_2O solvent) spectrum of sparingly soluble pTMSPDT (Figure 65) was very similar to that given by Owens[129]. The spectrum showed peaks centred at δ 2.77 (m, $H_{c\text{-}g}$), 1.62 (m, H_b) and 0.54 (t, H_a).

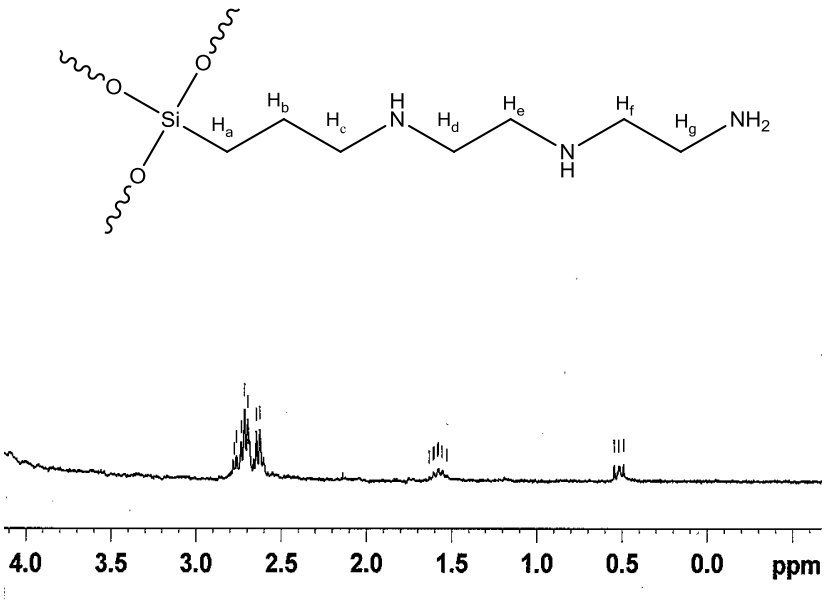

Figure 65. ^{1}H NMR (D_2O) spectrum of pTMSPDT.

A schematic representing the structure of pTMSPDT is given in Figure 66.

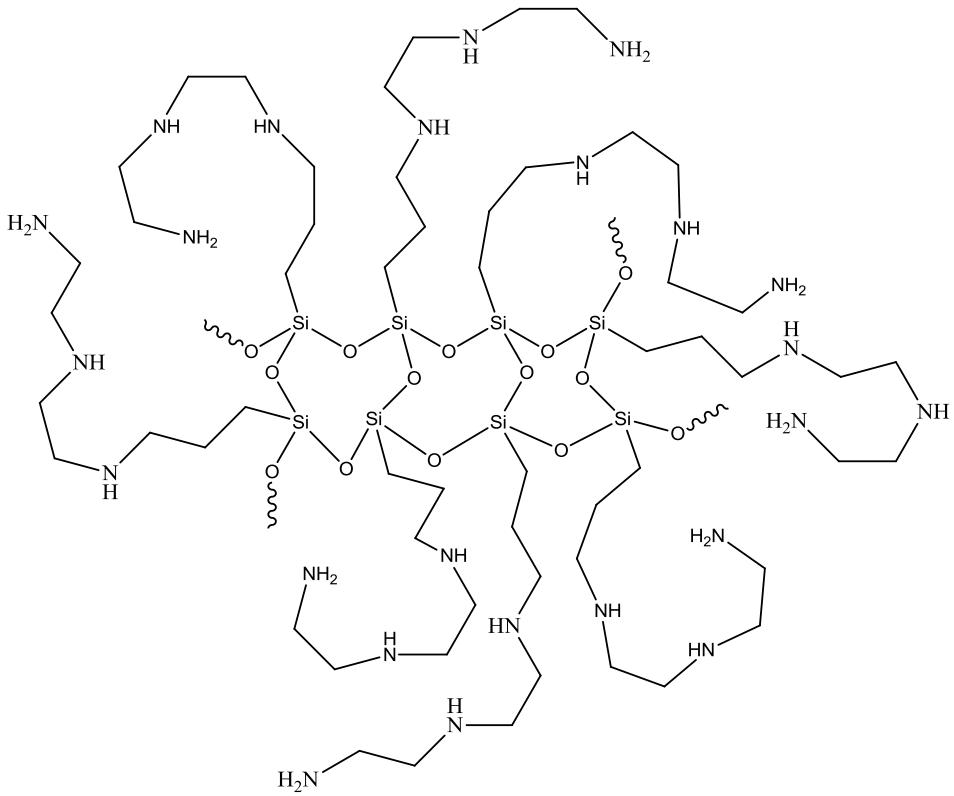

Figure 66. A schematic representing the structure of pTMSPDT (incorporated MeOH not shown).

The smooth surface topography of pTMSPDT (Figure 67) was very similar to that of pAPTES (Figure 36).

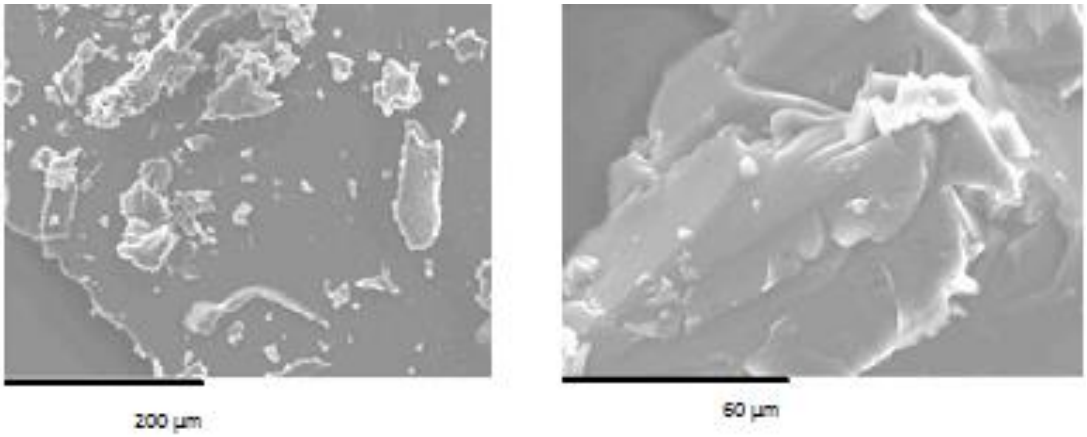

Figure 67. SEM images of pTMSPDT.

3.3.2 pTMSPDT-Fe_3O_4-MNPs

Black pTMSPDT-Fe_3O_4-MNPs were synthesised using a modified published method[49], in which an aqueous methanolic suspension of Fe_3O_4-MNPs were treated with mTMSPDT in a *ca.* 2.8:1 mole ratio at room temperature. As was found in the case of the IR spectrum of pAPTES-Fe_3O_4-MNPs (Figure 38), the spectrum of pTMSPDT-Fe_3O_4-MNPs (Figure 68) is dominated by very strong Fe-O bands (800-450 cm^{-1}) and moderately intense H-O-H and Si-O-Si bands (3401 and 1300-1100 cm^{-1}, respectively). A strong aliphatic C-H band was evident at 2933 cm^{-1}.

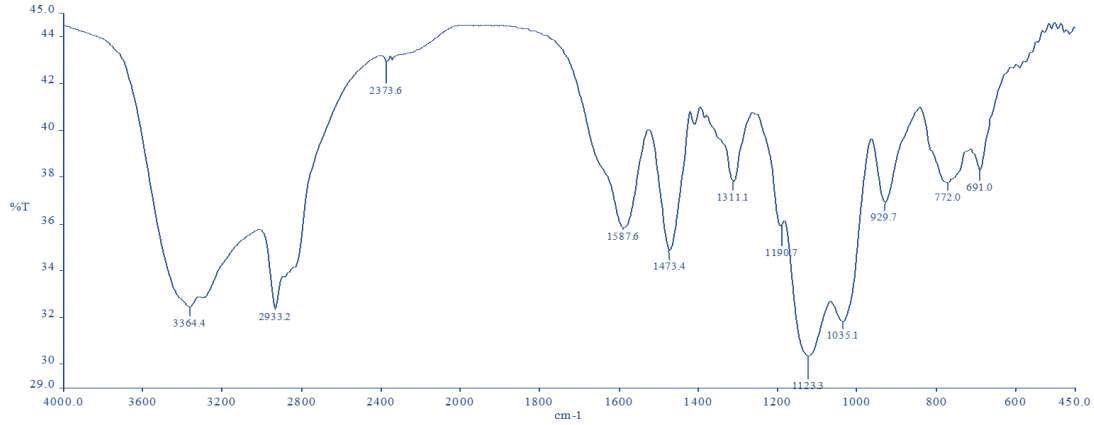

Figure 68. IR spectrum of pTMSPDT-Fe_3O_4-MNPs.

Microanalytical data (found: C 2.76%; H 0.68%, N 0.75%; %C:%N = 3.68:1) shows a significantly higher carbon content than that calculated for the propyldiethylenetriamine moiety, -$(CH_2)_3NH(CH_2)_2NH(CH_2)_2NH_2$ (calculated %C:%N = 2:1), again implying incorporation of methanol in the solid. It has been calculated that there are an average of 6 MeOH molecules present for each pendant -$(CH_2)_3NH(CH_2)_2NH(CH_2)_2NH_2$ moiety (gives a %C:%N ratio of 3.17:1).

A schematic representation of the structure of pTMSPDT-Fe_3O_4-MNPs is shown in Figure 69.

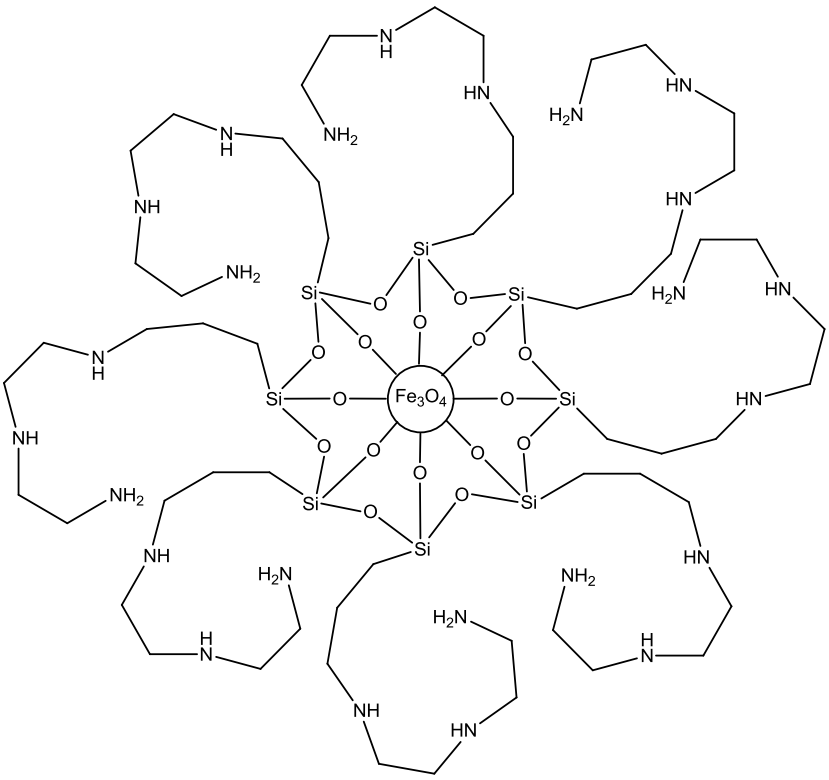

Figure 69. A schematic representation of the structure of pTMSPDT-Fe_3O_4-MNPs (incorporated MeOH molecules not shown).

The high magnification SEM image of pTMSPDT-Fe_3O_4-MNPs (Figure 70; 10 µm) reveals a flaky, layered morphology, and one which is quite different to the smooth/granular surfaces in pAPTES-Fe_3O_4-MNPs (Figure 39).

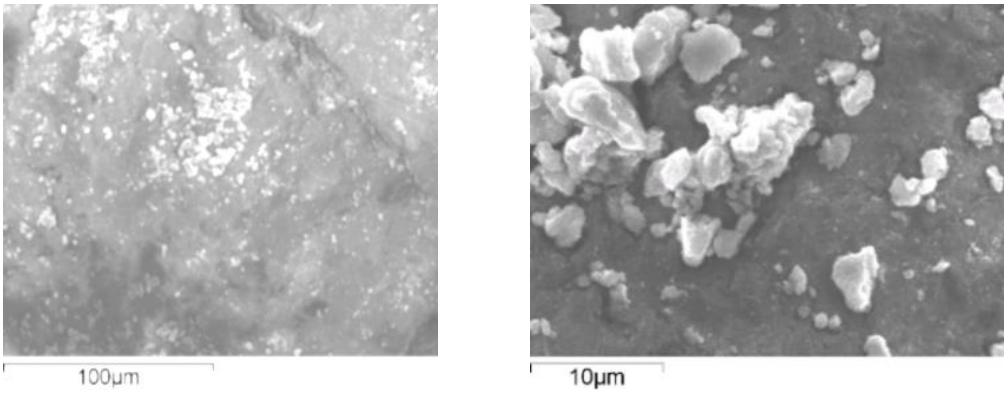

(a) (b)

Figure 70. SEM images of pTMSPDT-Fe_3O_4-MNPs.

3.3.3 [(NO3)2Cu-pTMSPDT]

Glass-like flakes of [$(NO_3)_2$Cu-pTMSPDT] could be made by reacting $Cu(NO_3)_2.3H_2O$ with either monomeric mTMSPDT or polymeric pTMSPDT in water. However, the mass yield in both reactions was quite small. Although the bulk appearance and royal blue colour of [$(NO_3)_2$Cu-pTMSPDT] was very similar to that of [$(NO_3)_2$Cu-pAPTES], the mass yield of the latter material was much superior. As expected, the IR spectra of [$(NO_3)_2$Cu-pAPTES] (Figure 43) and [$(NO_3)_2$Cu-pTMSPDT] (Figure 71) were quite alike, with both showing a strong, sharp nitrate band at 1384 cm^{-1} and also prominent H-O-H/amine and Si-O-Si bands (3600-3000 and 1200-850 cm^{-1}, respectively, for [$(NO_3)_2$Cu-pTMSPDT]). The IR spectra of [$(NO_3)_2$Cu-pTMSPDT] samples made using either mTMSPDT or pTMSPDT were identical.

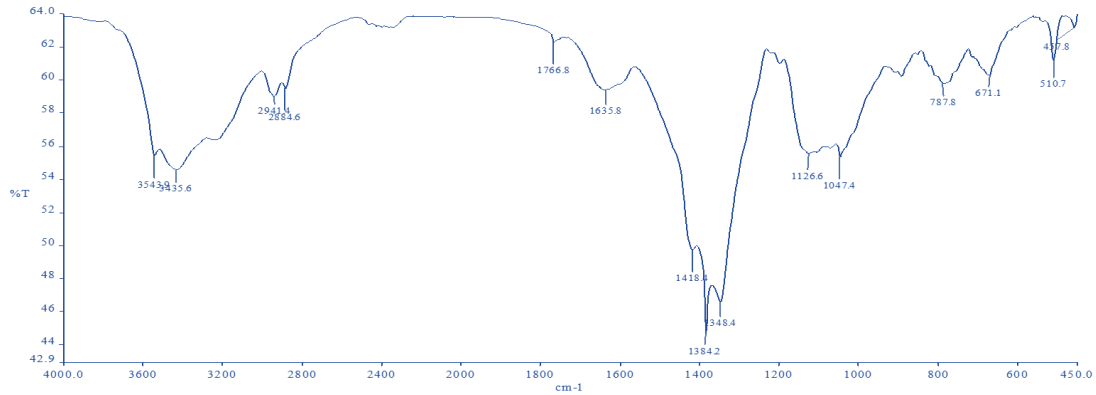

Figure 71. IR spectrum of $[(NO_3)_2Cu\text{-}pTMSPDT]$.

Although microanalytical data found for $[(NO_3)_2Cu\text{-}pTMSPDT]$ samples made using either mTMSPDT or pTMSPDT solids were different, the %C:%N ratios were quite similar (found using mTMSPDT: C 19.43%, H 4.69%, N 16.55%; %C:%N = 1.18:1: found using pTMSPDT: C 16.98%, H 4.03%, N 13.28%; %C:%N = 1.29:1). Theoretical calculations show that a ratio of one $Cu(NO_3)_2$ per one pendant $-(CH_2)_3NH(CH_2)_2NH(CH_2)_2NH_2$ moiety renders a %C:%N = 1.20:1, suggesting that each triamine functionality in the $[(NO_3)_2Cu\text{-}pTMSPDT]$ solid is coordinated to a Cu(II) centre giving two 5-membered chelate rings. A metal coordination number of four or five (as is usual for Cu^{2+} ions[140]) can be accomplished by the binding of water molecules. A schematic representation of one of a number of possible structural motifs for $[(NO_3)_2Cu\text{-}pTMSPDT]$ is shown in Figure 72.

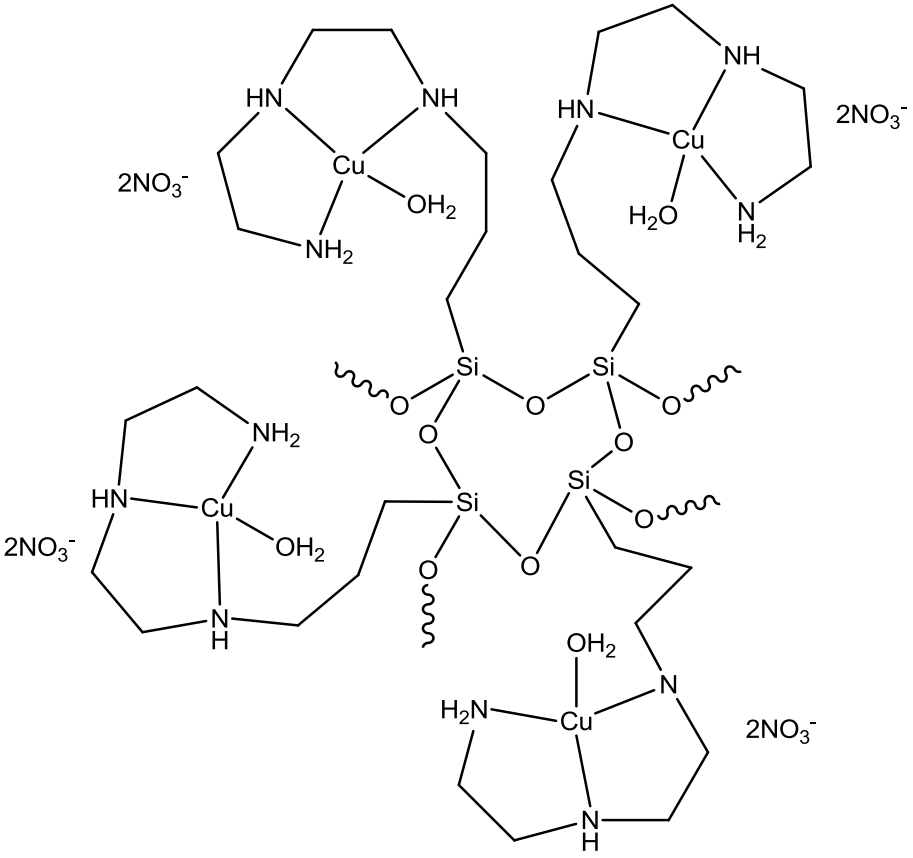

Figure 72. A schematic representation of one of the possible structural motifs for [$(NO_3)_2$Cu-pTMSPDT].

The surface topography of [$(NO_3)_2$Cu-pTMSPDT] made using mTMSPDT (Figure 73) showed smooth surfaces with some small bumps and ridges visible. The images of [$(NO_3)_2$Cu-pTMSPDT] made using pTMSPDT (Figure 74) showed globular formations on the surface under low magnification, which were very similar to those of [$(NO_3)_2$Cu-pTMSPDT] made using mTMSPDT (Figure 73).

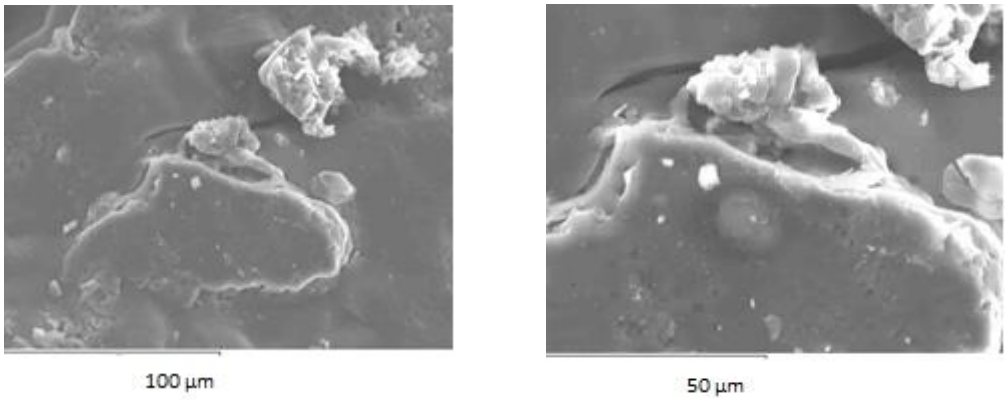

(a) (b)

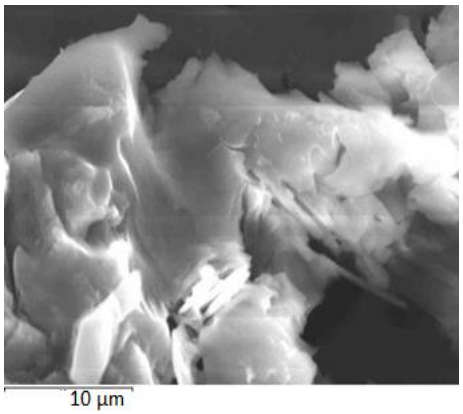

(c)

Figure 73. SEM images of [$(NO_3)_2$Cu-pTMSPDT] made using mTMSPDT.

Qualitative EDX spectra of [$(NO_3)_2$Cu-pTMSPDT] made using mTMSPDT (Figure 75 (a)) and pTMSPDT (Figure 75 (b)) confirmed the presence of carbon, copper, silicon and oxygen in both samples.

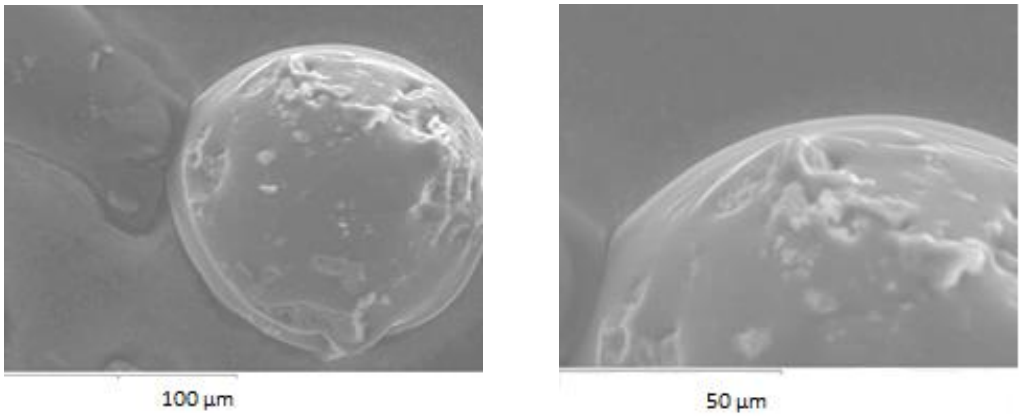

(a) (b)

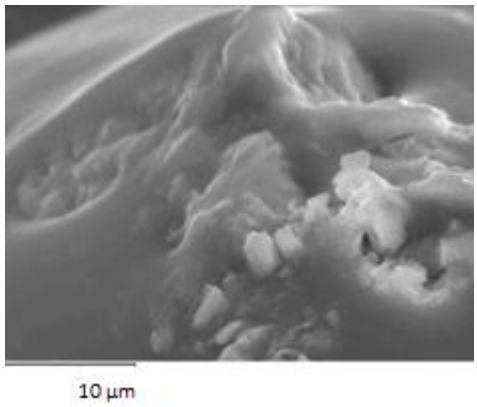

(c)

Figure 74. [$(NO_3)_2$Cu-pTMSPDT] made using pTMSPDT.

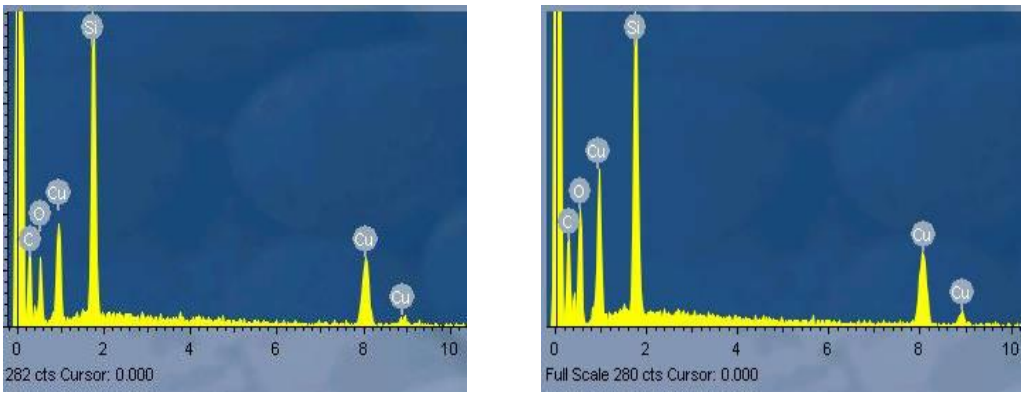

(a) (b)

Figure 75. EDX spectra of [$(NO_3)_2$Cu-pTMSPDT] made using (a) mTMSPDT and (b) pTMSPDT.

3.3.4 [$(OAc)_2$Cu-pTMSPDT-Fe_3O_4-MNPs]

Addition of $[Cu_2(OAc)_4(H_2O)_2]$ to a dispersion of pTMSPDT-Fe_3O_4-MNPs in methanol gave a moderate mass yield of black [$(OAc)_2$Cu-pTMSPDT-Fe_3O_4-MNPs]. The IR spectrum of the product (Figure 76) was almost identical to that of [$(OAc)_2$Cu-pAPTES-Fe_3O_4-MNPs] (Figure 48), with the strongest intensity bands being associated with H-O-H/ H-N-H/N-H stretches and Fe-O stretches (centred around 3420 and 580 cm^{-1}, respectively). The O-C-O asymmetric band is hidden under the broad H-O-H/H-N-H bending band (centred *ca.* 1632 cm^{-1}) whilst the weak, sharp band at 1385 cm^{-1} is believed to be the O-C-O symmetric stretching vibration. Very weak bands are present for the acetate C-H and silicone O-Si-O moieties (2918 and 1200-1000 cm^{-1}, respectively).

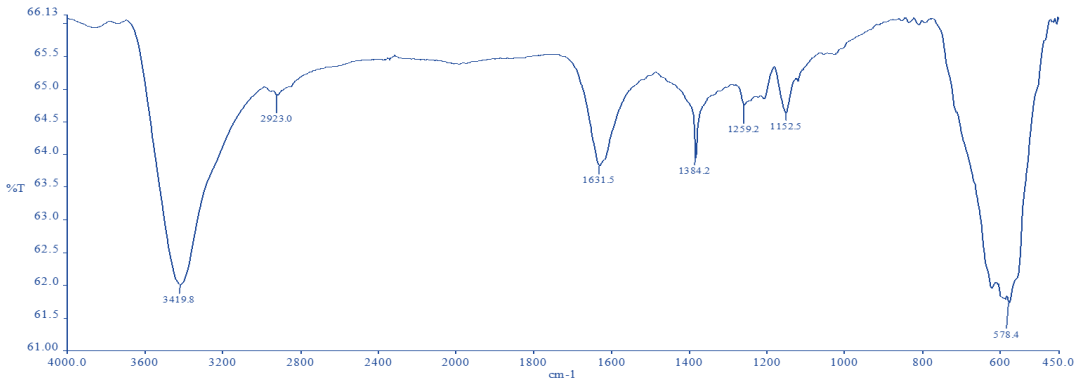

Figure 76. IR spectrum of [$(OAc)_2$Cu-pTMSPDT-Fe_3O_4-MNPs].

Microanalytical results for [$(OAc)_2$Cu-pTMSPDT-Fe_3O_4-MNPs] (found: C 10.42%, H 0.49%, N 0.43%; %C:%N = 24.23:1) indicated a very large %C:%N ratio, implying quite a high relative proportion of carbon in the material. A number of different formulations were tried in an attempt to match theoretical with found %C:%N figures.

If encapsulated solvent MeOH molecules are not factored into the formulation of [$(OAc)_2$Cu-pTMSPDT-Fe_3O_4-MNPs], then for each 1 pendant {-$(CH_2)_3NH(CH_2)_2NH(CH_2)_2NH_2$} moiety there would be a requirement of 20 $Cu(OAc)_2$ units to give gave a theoretical %C:%N value of 24.93:1, which is very close to the found value (24.23:1). This is in stark contrast to that found for [$(OAc)_2$Cu-pAPTES-Fe_3O_4-MNPs], where it was estimated that 1 $Cu(OAc)_2$ was associated with 1 pendant -$(CH_2)_3NH_2$ moiety. If solvent MeOH molecules are factored into the formulation of [$(OAc)_2$Cu-pTMSPDT-Fe_3O_4-MNPs] then a number of different (-$(CH_2)_3NH(CH_2)_2NH(CH_2)_2NH_2$ + $Cu(OAc)_2$ + MeOH) theoretical combinations could be used to match the found %C:%N ratio. For example, the combination of 1 -$(CH_2)_3NH(CH_2)_2NH(CH_2)_2NH_2$ + 12 $Cu(OAc)_2$ + 30 MeOH gives a theoretical %C:%N of 24.28:1, whilst 1 -$(CH_2)_3NH(CH_2)_2NH(CH_2)_2NH_2$ + 15 $Cu(OAc)_2$ + 20 MeOH gives a theoretical %C:%N of 24.86:1. Given that the product was not rigorously dried under vacuum, then it is a logical assumption that MeOH molecules are resident in the solid. Each -$(CH_2)_3NH(CH_2)_2NH(CH_2)_2NH_2$ functionality in [$(OAc)_2$Cu-pTMSPDT-Fe_3O_4-MNPs] is expected to coordinate to the Cu(II) centre to give two 5-membered chelate rings. In addition, there is the possibility for either one or both of the acetate anions to bind to the metal through the carboxylate oxygens (a large variety of carboxylate coordination modes are possible[141]). A schematic representation of one of a large number of possible structures for [$(OAc)_2$Cu-pAPTES-Fe_3O_4-MNPs] is shown in Figure 77.

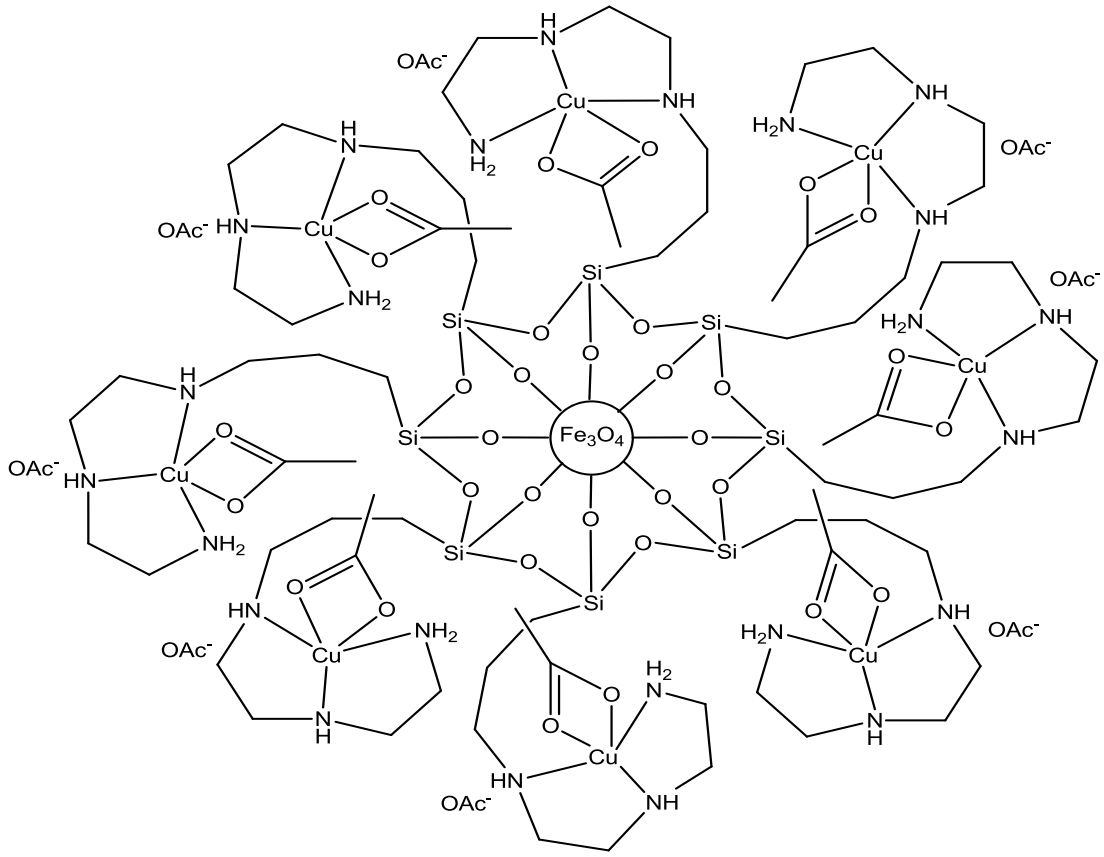

Figure 77. Schematic representation of one possible structure of [$(OAc)_2$Cu-pTMSPDT-Fe_3O_4-MNPs] (additional $Cu(OAc)_2$ and solvent MeOH molecules not shown).

SEM images of [$(OAc)_2$Cu-pTMSPDT-Fe_3O_4-MNPs] (Figure 78) reveal a smooth, flaky surface, and one which closely resemble that of its pAPTES analogue, [$(OAc)_2$Cu-pAPTES-Fe_3O_4-MNPs] (Figure 50). The EDX spectrum of [$(OAc)_2$Cu-pTMSPDT-Fe_3O_4-MNPs] (Figure 79) is also very similar to that of [$(OAc)_2$Cu-pAPTES-Fe_3O_4-MNPs] (Figure 51) and endorses the presence of a large quantity of surface iron and oxygen along with much smaller amounts of copper and silicon.

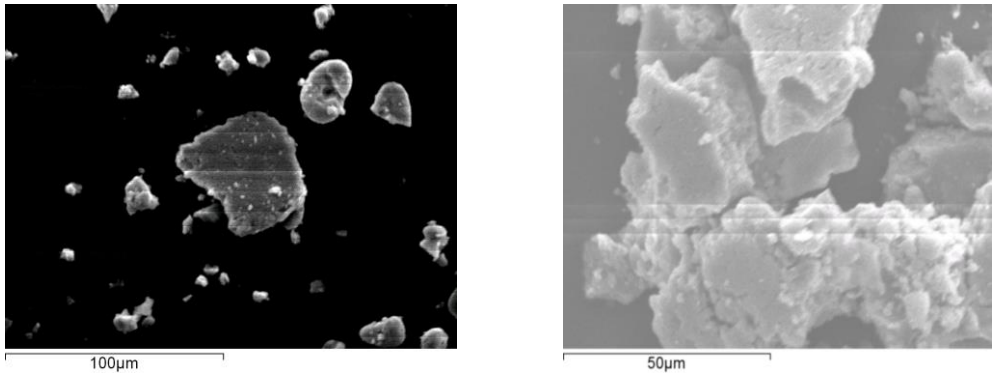

Figure 78. SEM images of [$(OAc)_2$Cu-pTMSPDT-Fe_3O_4-MNPs].

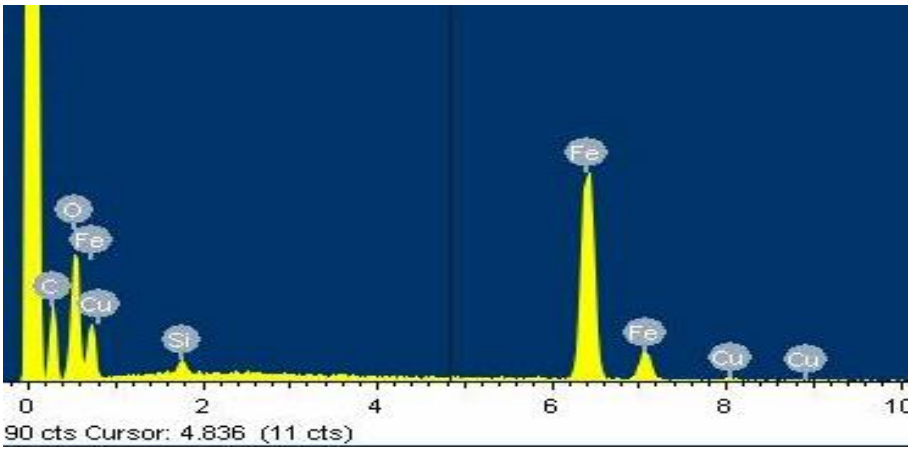

Figure 79. EDX spectrum of [$(OAc)_2$Cu-pTMSPDT-Fe_3O_4-MNPs].

3.3.5 SalH-pTMSPDT

By emulating a previously published procedure[129], yellow SalH-pTMSPDT was prepared in good yield by reacting salicylaldehyde with mTMSPDT (1:1 mole ratio) in water. The IR spectrum of the product (Figure 80) was very similar to that of yellow SalH-pAPTES (Figure 52), which was formed by the interaction of salicylaldehyde with pAPTES. Again, the prominent C=N band at 1634 cm^{-1} was verification of Schiff base

formation, whilst the broad O-Si-O band (1200-900 cm^{-1}) confirmed the creation of the silicone polymer.

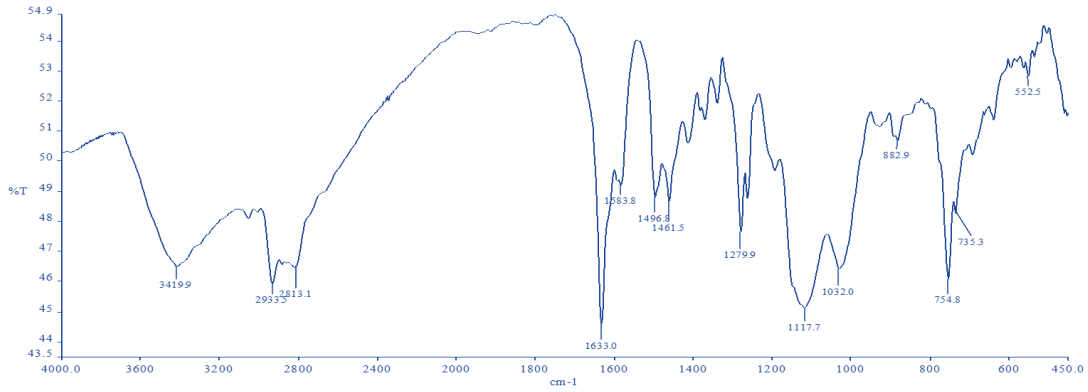

Figure 80. IR spectrum of SalH-pTMSPDT.

Microanalytical data for SalH-pTMSPDT (found: C 55.99%, H 6.82%, N 12.72%; %C:%N = 4.4:1) implies that each pendant $-(CH_2)_3NH(CH_2)_2NH(CH_2)_2NH_2$ moiety has reacted with a salicylaldehyde to form the corresponding Schiff base entity, $-(CH_2)_3NH(CH_2)_2NH(CH_2)_2N=CH(C_6H_3–OH)$. Inclusion of 1 MeOH molecule (formed during the hydrolysis of monomeric mTMSPDT molecules) along with each $-(CH_2)_3NH(CH_2)_2NH(CH_2)_2N=CH(C_6H_3–OH)$ entity gives a theoretical %C:%N ratio (4.29:1) which is close to that found for the sample. The fact that every pendant $-(CH_2)_3NH(CH_2)_2NH(CH_2)_2NH_2$ moiety in mTMSPDT gets converted to a Schiff base is in stark contrast to that found for mAPTES, where only one in every nine pendant $–CH_2CH_2CH_2NH_2$ functions forms the Schiff base entity.

A schematic representing the structure of SalH-pTMSPDT is given in Figure 81.

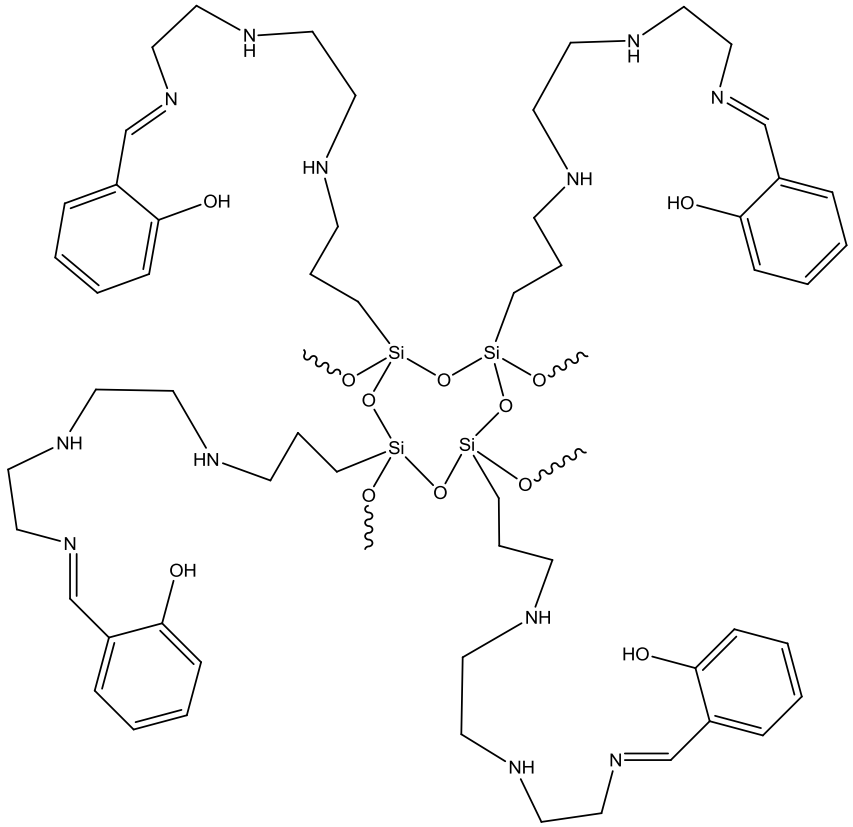

Figure 81. Schematic representation of the structure of SalH-pTMSPDT (encapsulated MeOH molecules not shown).

SEM images of SalH-pTMSPDT made using mTMSPDT reveal very smooth surfaces with some ridges visible (Figure 82).

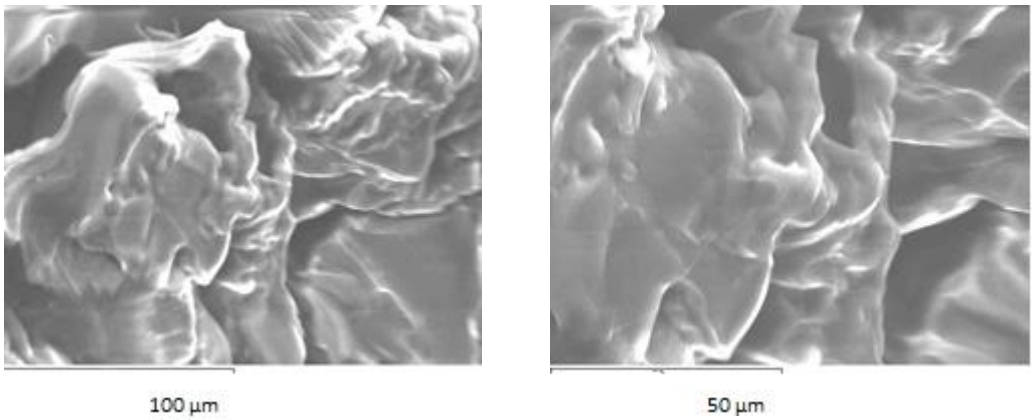

Figure 82. SEM images of SalH-pTMSPDT.

3.3.6 SalH-pTMSPDT-Fe_3O_4-MNPs

Addition of a methanolic solution of salicylaldehyde to pTMSPDT-Fe_3O_4-MNPs gave SalH-pTMSPDT-Fe_3O_4-MNPs as a brown powder. As anticipated, the IR spectrum of the product (Figure 83) closely resembled that of the pAPTES analogue, SalH-pAPTES-Fe_3O_4-MNPs (Figure 57), with the principal bands arising from the H-O-H/H-N-H/N-H and Fe-O vibrations (3434 and 790-450 cm^{-1}, respectively). Much weaker bands were evident for the aliphatic C-H and Si-O-Si stretches (2929 and 1350-1070 cm^{-1}, respectively) of the SalH-pAPTES moiety.

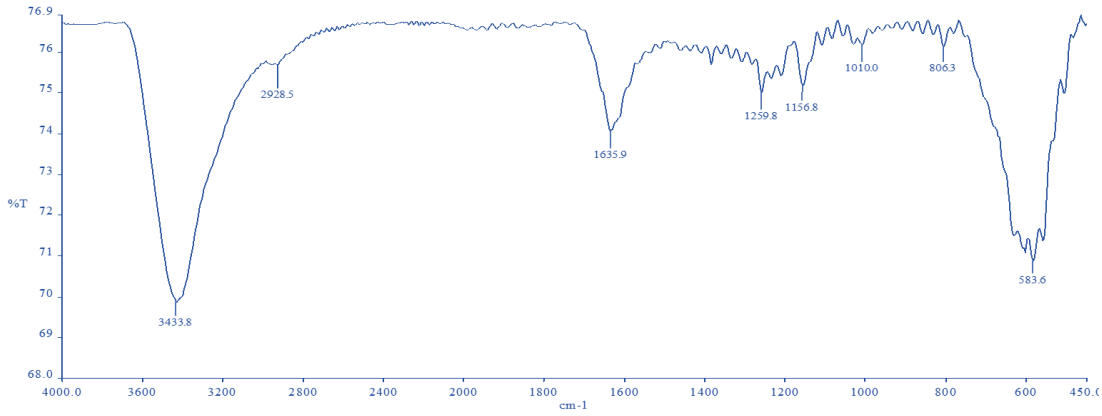

Figure 83. IR spectrum of SalH-pTMSPDT-Fe_3O_4-MNPs.

Microanalytical data for SalH-pTMSPDT-Fe_3O_4-MNPs (found: C 8.65%, H 0.53%, N 0.51%; %C:%N = 16.96:1) show that the solid contains a substantial quantity of extra carbon atoms. If it is accepted that all of the pendant $-(CH_2)_3NH(CH_2)_2NH(CH_2)_2NH_2$ functions on pTMSPDT-Fe_3O_4-MNPs have undergone a Schiff base condensation reaction, as was evidenced in the formation of SalH-pTMSPDT, then the theoretical %C:%N ratio should be 4:1. It is thought that the extra carbon content comes from encapsulated EtOH molecules (this assumes that the copious quantities of EtOH used

in the washing protocol has displaced any entrapped MeOH which was employed as the reaction solvent). Theoretical calculations show that, on average, for each pendant -$(CH_2)_3NH(CH_2)_2NH(CH_2)_2N{=}CH(C_6H_3{-}OH)$ moiety then 23 EtOH molecules must be added to give a %C:%N ratio of 17.1:1. This is a similar situation to that found in the case of SalH-pAPTES-Fe_3O_4-MNPs.

A schematic representation of the structure of SalH-pTMSPDT-Fe_3O_4-MNPs is shown in Figure 84.

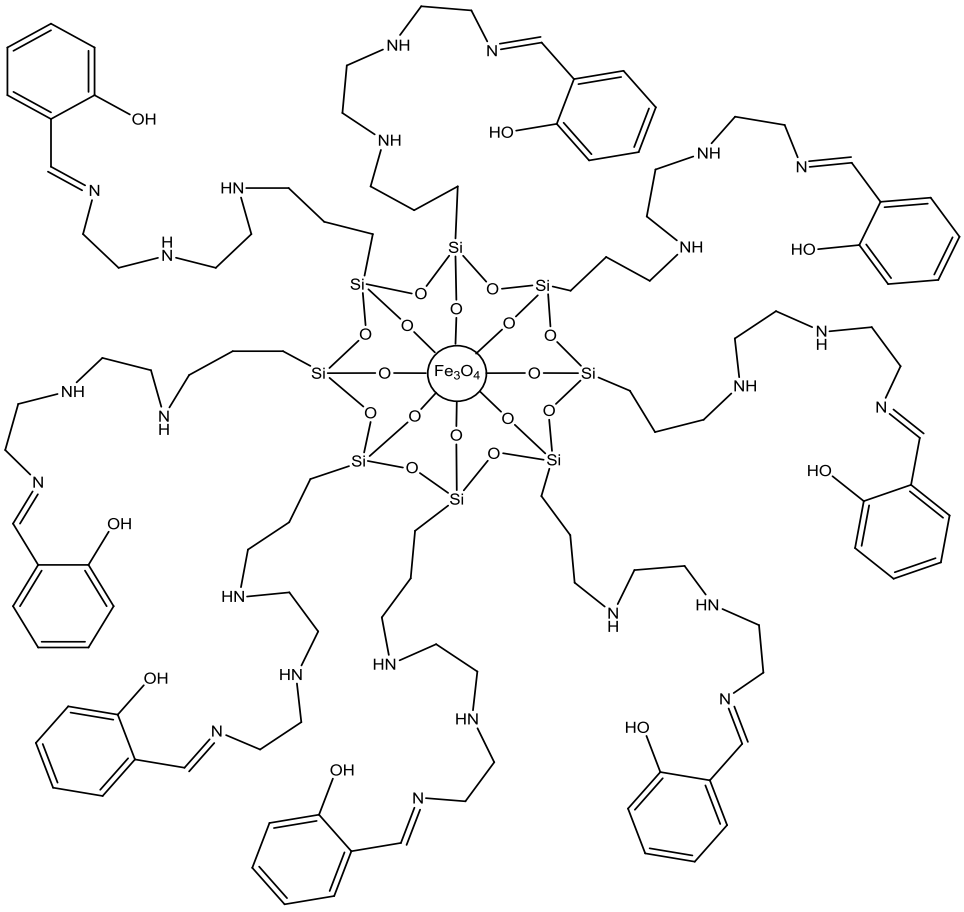

Figure 84. Schematic representation of the structure of SalH-pTMSPDT-Fe_3O_4-MNPs (trapped EtOH molecules not shown).

SEM images reveal that SalH-pTMSPDT-Fe_3O_4-MNPs (Figure 85) has a much smoother surface profile than the somewhat granular pAPTES analogue, SalH-pAPTES-Fe_3O_4-MNPs (Figure 59). The smooth surface of SalH-pTMSPDT-Fe_3O_4-MNPs was similar to that of SalH-pTMSPDT (Figure 82).

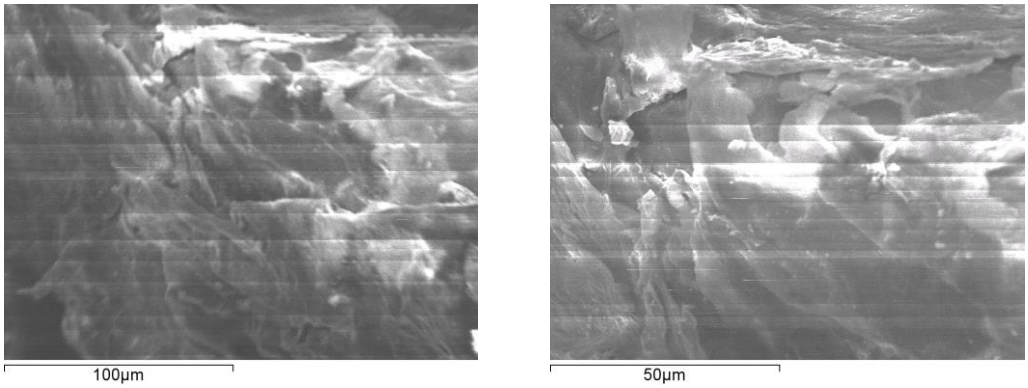

Figure 85. SEM images of SalH-pTMSPDT-Fe_3O_4-MNPs.

3.3.7 [Cu-Sal-pTMSPDT-Fe_3O_4-MNPs]

Treating a methanolic dispersion of SalH-pTMSPDT-Fe_3O_4-MNPs with $[Cu_2(OAc)_4(H_2O)_2]$ (2:1 mass ratio) affords the black powder, [Cu-Sal-pTMSPDT-Fe_3O_4-MNPs]. Not surprisingly, the IR spectrum of [Cu-Sal-pTMSPDT-Fe_3O_4-MNPs] (Figure 86) is almost identical to that of its precursor material, SalH-pTMSPDT-Fe_3O_4-MNPs (Figure 83). Although there are many similarities between the IR spectra of [Cu-Sal-pTMSPDT-Fe_3O_4-MNPs] and its pAPTES relative, [Cu-Sal-pAPTES-Fe_3O_4-MNPs] (Figure 60), the spectrum of the latter material has much more pronounced Si-O-Si bands.

As mentioned earlier (Section 3.2.7), in the cases of [Cu-Sal-$(mAPTES)_2$-Si-MCM 41][137] and [Cu-Sal-pAPTES-Fe_3O_4-MNPs], which were both synthesised using copper(II) acetate, charge balance for the encapsulated Cu^{2+} dications is provided by deprotonated phenolic oxygens from two salicylate residues, and not by acetate anions. This is also believed to be the case with [Cu-Sal-pTMSPDT-Fe_3O_4-MNPs], with the metal being chelated by the imine N and the phenolic O atoms as well as by amine N atoms. As with [Cu-Sal-pAPTES-Fe_3O_4-MNPs], acetate O-C-O bands were not apparent in the IR spectrum of [Cu-Sal-pTMSPDT-Fe_3O_4-MNPs].

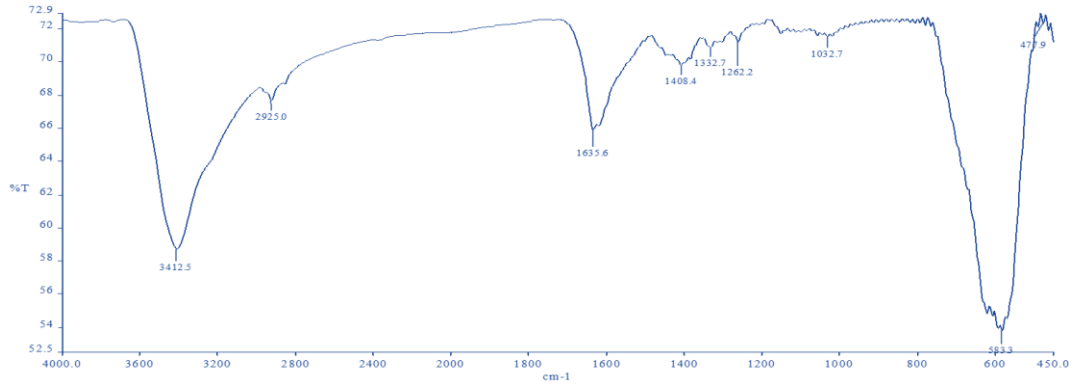

Figure 86. IR spectrum of [Cu-Sal-pTMSPDT-Fe_3O_4-MNPs].

Microanalytical data showed that for [Cu-Sal-pTMSPDT-Fe_3O_4-MNPs] (found: C 5.32%, H 0.52%, N 0.51%; %C:%N = 10.43:1) an average of 22 MeOH molecules must be added for each pendant $-(CH_2)_3NH(CH_2)_2NH(CH_2)_2N{=}CH(C_6H_3{-}OH)$ moiety (theoretical %C:%N ratio = 10.29:1).

A schematic illustrating one of a number of possible structures of [Cu-Sal-pTMSPDT-Fe_3O_4-MNPs] is given in Figure 87.

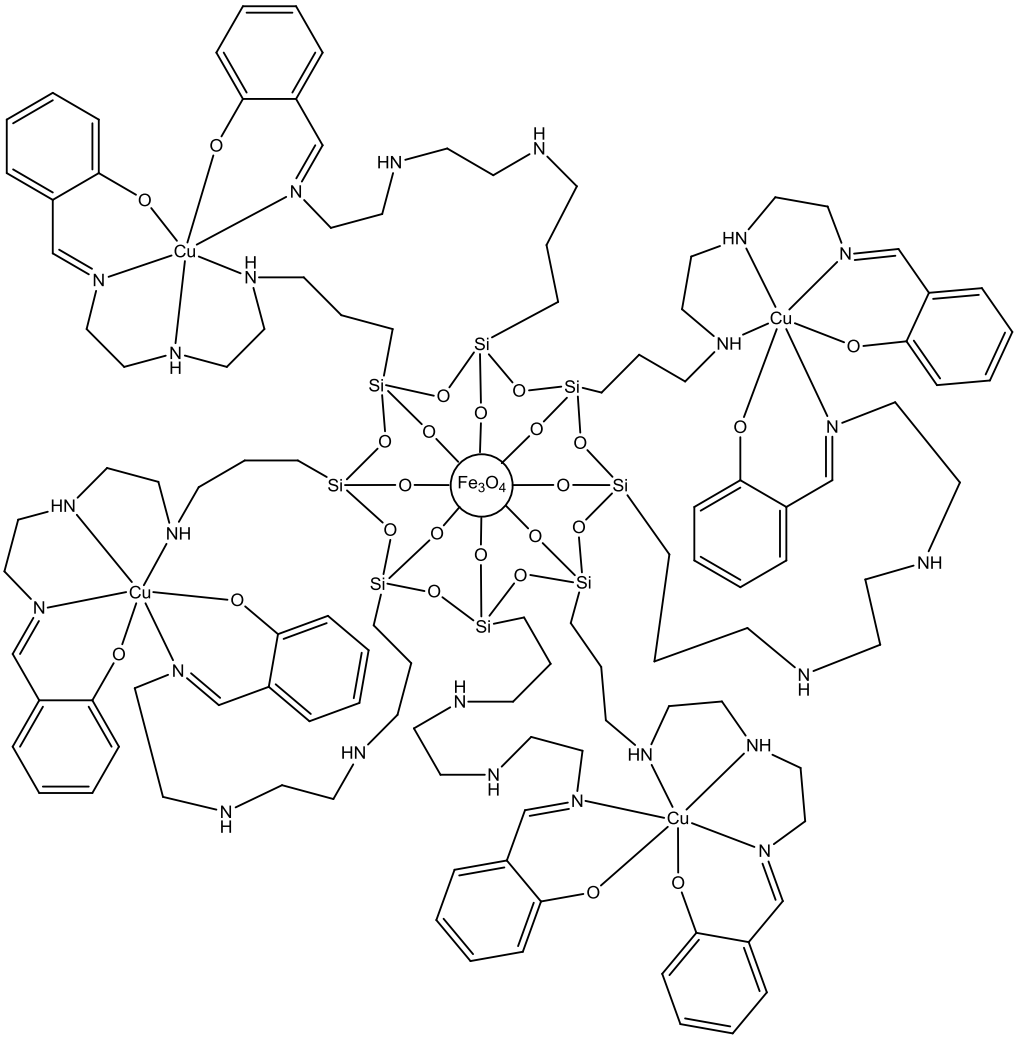

Figure 87. Schematic for one of a number of possible structures of [Cu-Sal-pTMSPDT-Fe_3O_4-MNPs] (MeOH molecules not shown). Note that two deprotonated phenolic oxygens from two salicylate residues are required for charge balance.

SEM images of [Cu-Sal-pTMSPDT-Fe_3O_4-MNPs] (Figure 88) show a relatively smooth underlying surface which is dashed with numerous small, coarse-textured eruptions. The latter features are absent in images of both the precursor material, SalH-pTMSPDT-Fe_3O_4-MNPs (Figure 85) and the pAPTES analogue, [Cu-Sal-pAPTES-Fe_3O_4-MNPs] (Figure 63). The EDX spectrum of [Cu-Sal-pTMSPDT-Fe_3O_4-MNPs] (Figure 89) is similar to that exhibited by [Cu-Sal-pAPTES-Fe_3O_4-MNPs] (Figure 63) and shows the

presence of copious quantities of surface iron, silicon and oxygen and a tiny amount of copper.

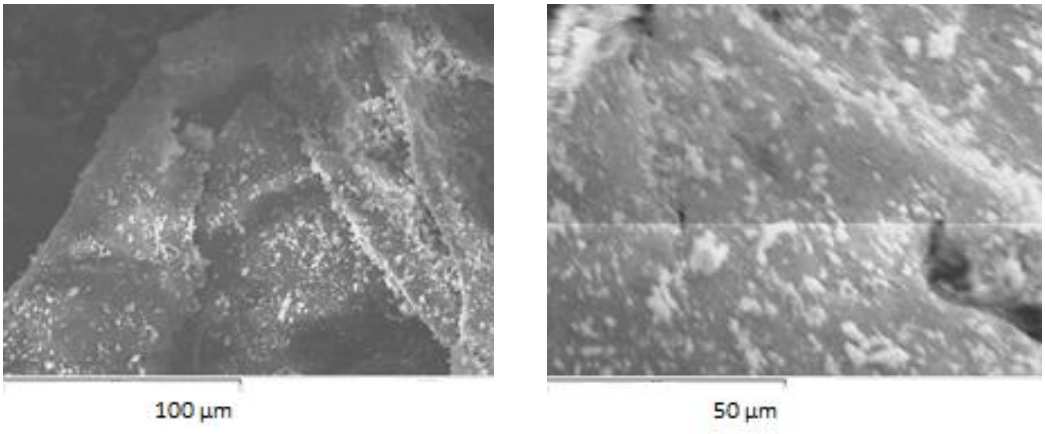

(a) (b)

Figure 88. SEM images of [Cu-Sal-pTMSPDT-Fe_3O_4-MNPs] under (a) low magnification and (b) high magnification.

The EDX spectrum of [Cu-Sal-pTMSPDT-Fe_3O_4-MNPs] (Figure 89) confirms the presence of carbon, oxygen, iron and copper.

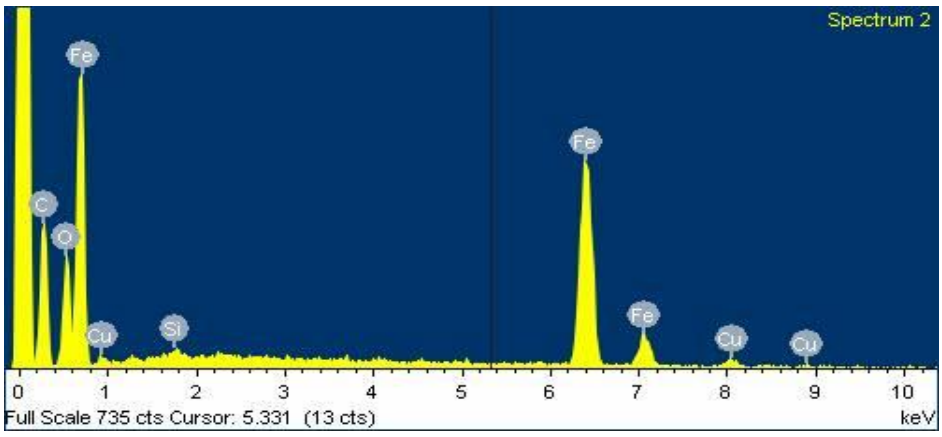

Figure 89. EDX spectrum of [Cu-Sal-pTMSPDT-Fe_3O_4-MNPs].

3.4 Anti-*Candida* Activity

The qualitative results of *in vitro* tests to determine the activity of the materials against the growth of the fungal pathogen, *C. albicans*, are given in Table 3. After seeding petri dishes with *Candida* cells, three samples of the same solid test material were added and the dishes incubated at 37 °C for 20 h. After this period, the dishes were visually inspected for signs of growth inhibition. Images of the actual culture dishes containing the test materials and the *C. albicans* cells are given in Figures 91-93.

As expected, uncoated Fe_3O_4-MNPs did not deter fungal cells reproduction (Figure 90 (a)). Indeed, it is possible that Fe_3O_4-MNPs may even have provided a convenient source of iron ions which are known to be essential for sustaining healthy cell growth[142]. The silicone polymers, pAPTES and pTMSPDT (Figures 90 (b) and 92 (a), respectively), both deterred the growth of *C. albicans* as was evidenced by the clear zones of inhibition around the sample areas. It is thought that the pendant amine moieties present in both of these amino-functionalised silicone polymers could be effectively sequestering transition metal ions from critical metalloenzymes present in the fungal cell which causes enzyme malfunction and the ultimate demise of the organism. A similar hypothesis has been used to account for the devastating effects on *C. albicans* induced by the metal-free chelating ligands, 1,10-phenanthroline[96 99] and 1,10-phenanthroline-5,6-dione[143].

Table 3. Results from visual inspection of petri dishes containing *C. albicans* and administered solid test materials.

Materials	**Inhibition of growth of *C. albicans***
Fe_3O_4-MNPs	no inhibition
pAPTES	Inhibition
pAPTES-Fe_3O_4-MNPs	no inhibition
[$(NO_3)_2$Cu-pAPTES]	Inhibition
[$(OAc)_2$Cu-pAPTES-Fe_3O_4-MNPs]	no inhibition
SalH-pAPTES	Inhibition
SalH-pAPTES-Fe_3O_4-MNPs	no inhibition
[Cu-Sal-pAPTES-Fe_3O_4-MNPs]	no inhibition
pTMSPDT	Inhibition
pTMSPDT-Fe_3O_4-MNPs	no inhibition
[$(NO_3)_2$Cu-pTMSPDT]	Inhibition
[$(NO_3)_2$Cu-pTMSPDT]	Inhibition
[$(OAc)_2$Cu-pTMSPDT-Fe_3O_4-MNPs]	no inhibition
SalH-pTMSPDT	Inhibition
SalH-pTMSPDT-Fe_3O_4-MNPs	no inhibition
[Cu-Sal-pTMSPDT-Fe_3O_4-MNPs]	no inhibition

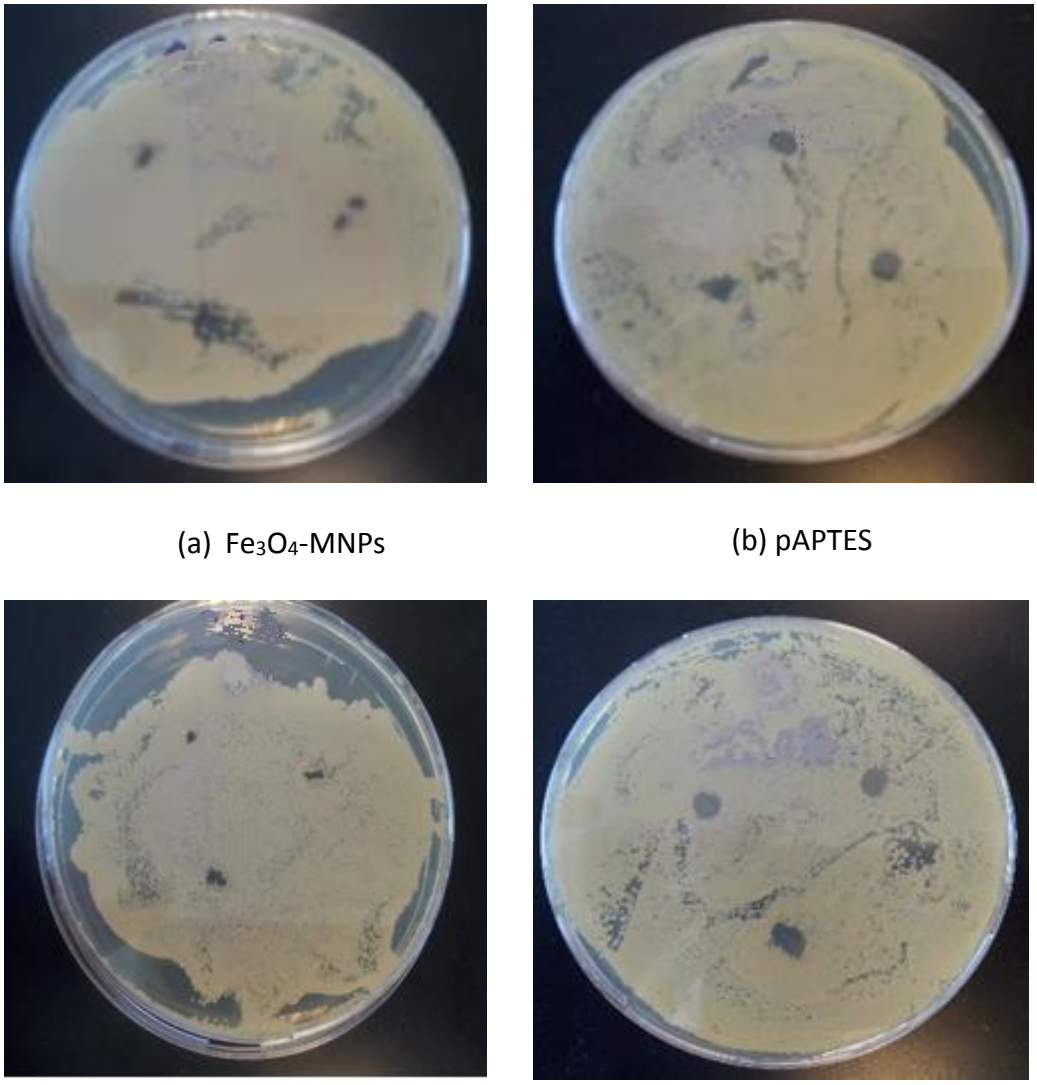

(a) Fe_3O_4-MNPs

(b) pAPTES

(c) pAPTES-Fe_3O_4-MNPs

(d) [$(NO_3)_2$Cu-pAPTES]

Figure 90. Petri dishes with growing *C. albicans* cells and administered test material. (a) Fe_3O_4-MNPs (no inhibition); (b) pAPTES (inhibition); (c) pAPTES-Fe_3O_4-MNPs (no inhibition); (d) [$(NO_3)_2$Cu-pAPTES] (inhibition).

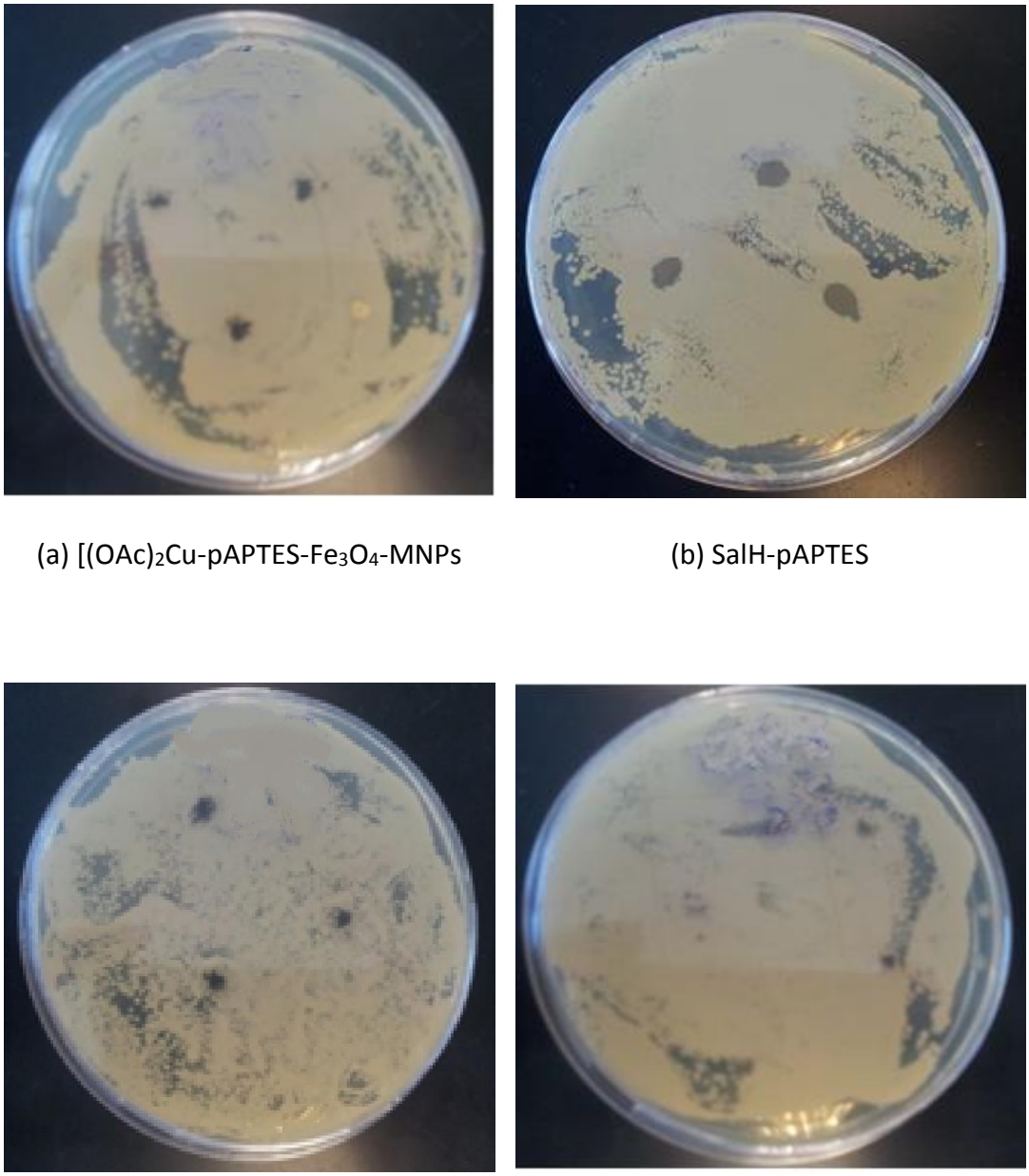

(a) [$(OAc)_2$Cu-pAPTES-Fe_3O_4-MNPs (b) SalH-pAPTES

(c) SalH-pAPTES-Fe_3O_4-MNPs (d) [Cu-Sal-pAPTES-Fe_3O_4-MNPs]

Figure 91. Petri dishes with growing *C. albicans* cells and administered test material. (a) [$(OAc)_2$Cu-pAPTES-Fe_3O_4-MNPs] (no inhibition); (b) Sal-pAPTES (inhibition); (c) SalH-pAPTES-Fe_3O_4-MNPs (no inhibition); (d) [Cu-Sal-pAPTES-Fe_3O_4-MNPs] (no inhibition).

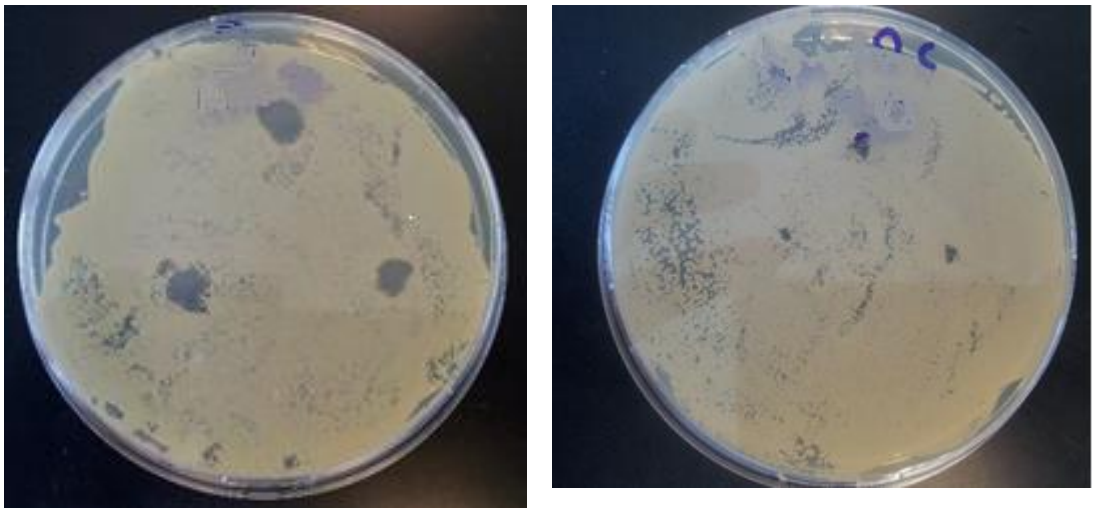

(a) pTMSPDT (b) pTMSPDT-Fe_3O_4-MNPs

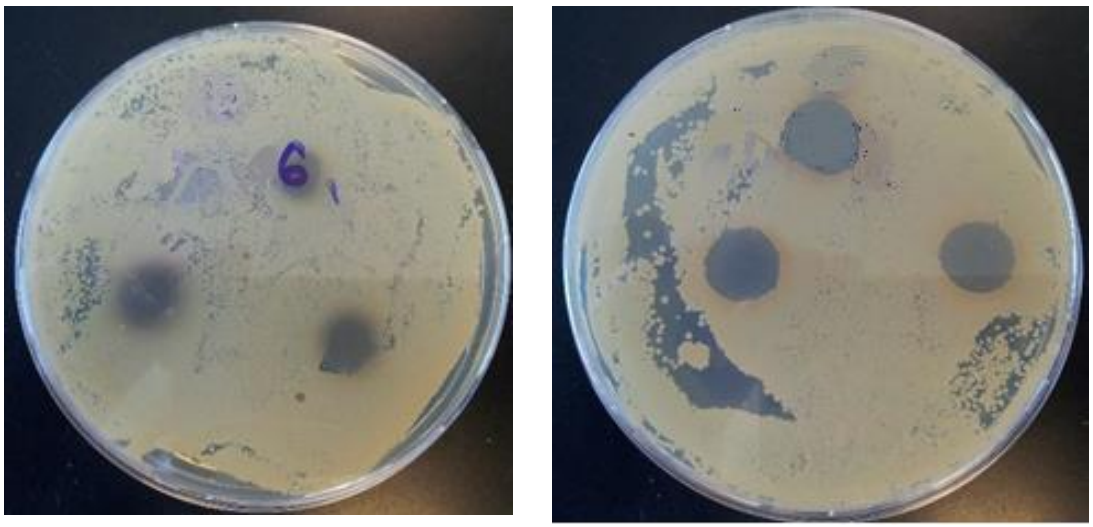

(c) [$(NO_3)_2$Cu-pTMSPDT] (d) [$(NO_3)_2$Cu-pTMSPDT]

Figure 92. Petri dishes with growing *C. albicans* cells and administered test material. (a) pTMSPDT (inhibition); (b) pTMSPDT-Fe_3O_4-MNPs (no inhibition); (c) [$(NO_3)_2$Cu-pTMSPDT] (inhibition); (d) [$(NO_3)_2$Cu-pTMSPDT] (inhibition).

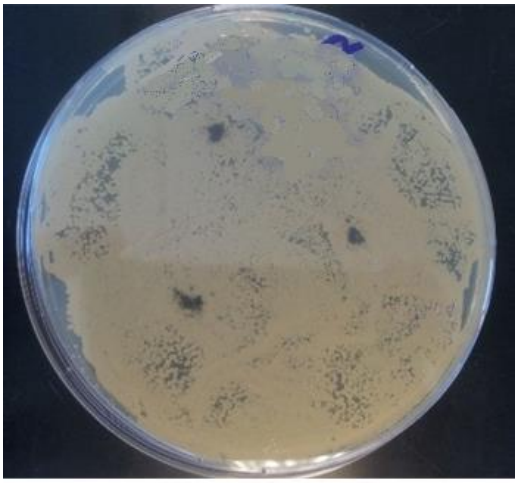

(a) [$(OAc)_2$Cu-pTMSPDT-Fe_3O_4-MNPs]

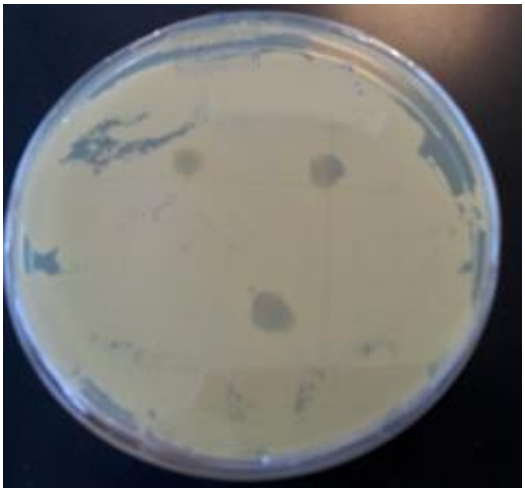

(b) SalH-pTMSPDT

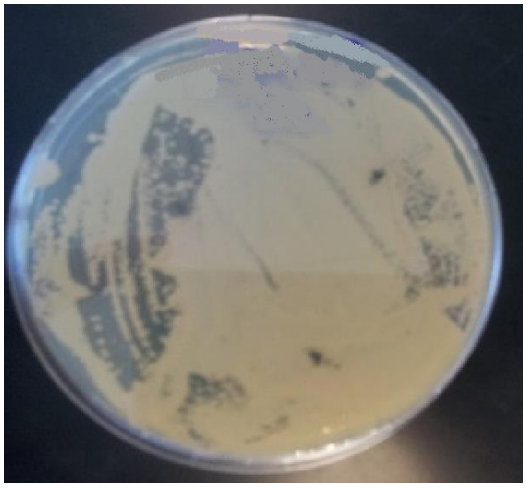

(c) SalH-pTMSPDT-Fe_3O_4-MNPs

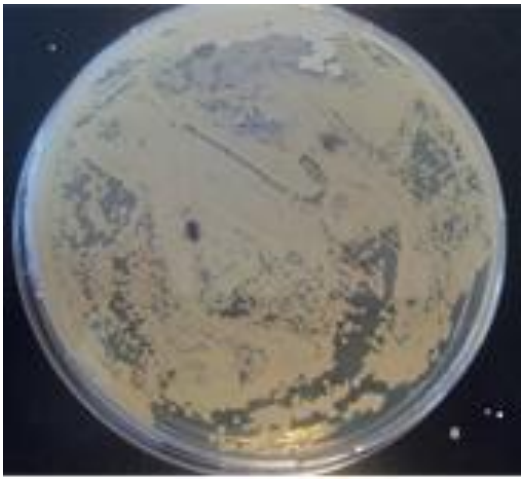

(d) [Cu-Sal-pTMSPDT-Fe_3O_4-MNPs]

Figure 93. Petri dishes with growing *C. albicans* cells and administered test material. (a) [$(OAc)_2$Cu-pTMSPDT-Fe_3O_4-MNPs] (no inhibition); (b) SalH-pTMSPDT (inhibition); (c) SalH-pTMSPDT-Fe_3O_4-MNPs (no inhibition); (d) [Cu-Sal-pTMSPDT-Fe_3O_4-MNPs] (no inhibition).

The Schiff base salicylates, SalH-pAPTES and SalH-pTMSPDT (Figures 94 (b) and 96 (b), respectively), also promoted cell death and again this is being attributed to their ability to requisition metals from vital cellular enzymes.

The Cu(II)-containing silicone polymers which were not surface bonded to Fe_3O_4-MNPs i.e. [$(NO_3)_2$Cu-pAPTES] and [$(NO_3)_2$Cu-pTMSPDT] (Figures 93 (d) and 95 (c) and (d), respectively), were also lethal to the fungal cells. A combination of released toxic Cu(II) ions and deactivation of metalloezymes by the now free pendant amine functionalities is thought to be responsible for the fate of the cell.

In contrast to the good activity demonstrated by the silicone polymers, their salicylate Schiff base derivatives and their Cu(II) complexes, all of these materials were inactive when coated onto the surface of Fe_3O_4-MNPs. It is believed that there are insufficient quantities of the silicones (with or without Cu(II) ions) present on the surface of the nanoparticles to enable an antimicrobial effect.

Conclusion

The replication of literature procedures for the polymerisation of monomeric (3-aminopropyl)triethoxysilane (APTES) and (3-trimethoxysilylpropyl)diethylene triamine (TMSPDT) affords the colourless, amine-functionalised silicone polymers (pAPTES and pTMSPDT) in good yield. Subsequent condensation reactions of the silicones with salicylaldehyde gives the corresponding yellow, Schiff base derivatives. In the case of pAPTES, only 10% of the pendant 3-aminopropyl groups condense with the aldehyde, whilst all of the terminal amine groups of pTMSPDT transformed to imines. Increasing the concentration of added salicylaldehyde and/or prolonging the reaction time might enhance the extent of Schiff base conversion for pAPTES.

Magnetic nanoparticles (Fe_3O_4-MNPs) are readily procured using a standardised synthetic protocol involving a specific molar combination of simple Fe(II) and Fe(III) salts. Surface coating of the Fe_3O_4-MNPs with pAPTES and pTMSPDT is achieved by interaction of the nanoparticles with the appropriate aminosilane monomer. Again, the Schiff base adducts are obtained upon reaction with salicylaldehyde. Whereas the naked, highly aggregated Fe_3O_4-MNPs can readily be recovered from suspension using a strong permanent magnet, the silicone-coated Fe_3O_4-MNPs are much less aggregated and require high-speed centrifugation for product recovery (which is usually incomplete and results in low mass yields).

Coordination of Cu(II) ions to the pendant amine functionalities of the silicone materials occurs upon treatment with simple copper(II) salts.

A combination of microanalytical and IR spectral data are used to characterize the solid polymers which, with the exception of pAPTES and pTMSPDT are insoluble. Most of the materials retain large quantities of trapped water or alcohol, even after vacuum desiccation at ca. 50 °C. Given that the polymeric products are likely to be inhomogeneous it is not possible to offer 'exact' chemical structures for the materials, and only 'possible' structural entities can be inferred. Unsurprisingly, a wide variation in surface morphologies is seen across the various polymers with some consistencies being observed between pAPTES and pTMSPDT analogues.

Only pAPTES, pTMSPDT, their Cu(II) complexes and the Schiff base derivatives of the aminosilanes deter the growth of the fungal pathogen, *Candida albicans*. Disappointingly, none of the coated Fe_3O_4-MNPs were active. It is thought that there are only minimal amounts of bioactive amine groups and Cu(II) ions present on the nanoparticle surfaces, presumed to arise from the relatively large particle sizes (which translates to a small surface area). Decreasing particle size (with consequent increases in surface area), through possible modification of the Fe_3O_4-MNPs synthesis protocol, may enhance the antimicrobial performance. Coordination of alternative transition metals with known high antifungal activity (e.g. Ag(I), Mn(II)) could also improve the bioactivity.

References

(1) Curtis, J.; Klykken, P. A comparative assessment of three common catheter materials. *Dow Corning Corporation.* **2008**.

(2) Global Supplier of Medical devices. http://74.53.161.98/~surgime/?page_id=239 (accessed 11 April **2015**).

(3) Silicone Scar Sheet. http://cavyl.hubpages.com/hub/siliconescarsheet (accessed 11 April **2015**).

(4) Kulig, J.; Jefferies, V.; Schwamm, D.; Litt, M.; Sheats, J.; Carraher Jr, C. E.; Pittman Jr, C. U.; Zeldin, M.; Currell, B. Inorganic and Metal Containing Polymeric Materials. *Plenum Press, New York.* **1990**, 225.

(5) Stevens, M. P.: *Polymer Chemistry: An Introduction*; 2nd ed.; Oxford University Press. **1990.**

(6) Jones, R.; Ando, W.; Chojnowski, J.: *Silicon-Containing Polymers: The Science and Technology of Their Synthesis and Applications* Kluwer Academic Publishers. **2000**.

(7) Mayer, H. The chemistry and properties of silicone resins: network formers (in paints and renders). *Pigm. Resin Technol.* **1998**, *27*, 364-373.

(8) Colas, A.; Curtis, J. Silicone biomaterials: history and chemistry. *Biomater. Sci. (2nd Ed.).* **2004**, 80-86.

(9) Chauhan, B. P. S.; Rathore, J.; Sardar, R.; Tewari, P.; Latif, U. Synthesis, stabilization, and applications of nanoscopic siloxane–metal particle conjugates. *J. Organomet. Chem.* **2003**, *686*, 24-31.

(10) Goldman, J. A.; Greenblatt, J.; Joines, R.; White, L.; Aylward, B.; Lamm, S. H. Breast implants, rheumatoid arthritis, and connective tissue diseases in a clinical practice. *J. Chronic Dis.* **1995**, *48*, 571-582.

(11) Scientific Committee on Emerging and Newly Identified Health Risks. *The Safety of PIP Silicone Breast Implants.* **2012.**

(12) Bistričić, L.; Volovšek, V.; Dananić, V.; Šapić, I. M. Conformational stability and vibrations of aminopropylsilanol molecule. *Spectrochimica Acta Part A: Molecular and Biomolecular Spectroscopy*. **2006**, *64*, 327-337.

(13) Clayden, J.; Greeves, N.; Warren, S.; Wothers, P.: *Organic Chemistry*; Oxford University Press. **2001**.

(14) Blanco-Brieva, G.; Capel-Sanchez, M. C.; Campos-Martin, J. M.; Fierro, J. L. G. Effect of precursor nature on the behavior of titanium-polysiloxane homogeneous catalysts in primary alkene epoxidation. *J. Mol. Catal. A: Chem.* **2007**, *269*, 133-140.

(15) Brochier Salon, M.-C.; Belgacem, M. N. Competition between hydrolysis and condensation reactions of trialkoxysilanes, as a function of the amount of water and the nature of the organic group. *Colloids Surf., A.* **2010**, *366*, 147-154.

(16) Brochier Salon, M.-C.; Belgacem, M. N. Hydrolysis-Condensation Kinetics of Different Silane Coupling Agents. *Phosphorus, Sulfur Silicon Relat. Elem.* **2011**, *186*, 240-254.

(17) Spruell, J. M.; Wolfs, M.; Leibfarth, F. A.; Dimitriou, M. D.; Connal, L. A.; Hawker, C. J. Simple, yet powerful reactions for polymer crosslinking and functionalization. *243rd ACS National Meeting & Exposition.* **2012**.

(18) Brann, J. E.; Hughes, M. M.; Cree, S. H.; Penfold, J. Silane-crosslinkable elastomer-polyolefin polymer blends, their preparation and properties, and use as crosslinked moldings. Application: US Patent 1996-657926 5741858.

(19) Satti, A. J.; Nador, F.; Vitale, C.; Radivoy, G.; Andreucetti, N. A.; Ciolino, A. E.; Valles, E. M. Synthesis, characterization, and gamma radiation effects over well-defined poly(vinylsiloxanes) copolymers. *J. Appl. Polym. Sci.* **2012**, *124*, 832-839.

(20) Takeyama, A.; Sugimoto, M.; Yoshikawa, M. Gas permeation property of SiC membrane using curing of polymer precursor film by electron beam irradiation in helium atmosphere. *Materials Transactions* **2011**, *52*, 1276-1280.

(21) Taylor, A. Defined hybrid building blocks. *Eur. Coat. J.* **2007**, 28-33.

(22) Hsueh, H.-B.; Chen, C.-Y.; Wang, C.-C.; Chu, T.-J. Preparation and properties of APPSSQ-like/polyimide hybrid composites. *J. Appl. Polym. Sci.* **2003**, *89*, 2865-2874.

(23) Schütz, M. R.; Sattler, K.; Deeken, S.; Klein, O.; Adasch, V.; Liebscher, C. H.; Glatzel, U.; Senker, J.; Breu, J. Improvement of thermal and mechanical properties of a phenolic resin nanocomposite by in situformation of silsesquioxanes from a molecular precursor. *J. Appl. Polym. Sci.* **2010**, *117*, 2272-2277.

(24) Steinmetz, J. R.; Arkles, B. C. Preparation of stable water-borne silane compositions. Application: EP Patent 94-302373 675128.

(25) Brochier Salon, M.-C.; Bayle, P.-A.; Abdelmouleh, M.; Boufi, S.; Belgacem, M. N. Kinetics of hydrolysis and self condensation reactions of silanes by NMR spectroscopy. *Colloids Surf., A.* **2008**, *312*, 83-91.

(26) Bois, L.; Bonhommé, A.; Ribes, A.; Pais, B.; Raffin, G.; Tessier, F. Functionalized silica for heavy metal ions adsorption. *Colloids Surf., A.* **2003**, *221*, 221-230.

(27) Suzuki, T. M.; Nakamura, T.; Fukumoto, K.; Yamamoto, M.; Akimoto, Y.; Yano, K. Direct synthesis of amino-functionalized monodispersed mesoporous silica spheres and their catalytic activity for nitroaldol condensation. *J. Mol. Catal. A: Chem.* **2008**, *280*, 224-232.

(28) Huh, S.; Wiench, J. W.; Yoo, J.-C.; Pruski, M.; Lin, V. S. Y. Organic Functionalization and Morphology Control of Mesoporous Silicas via a Co-Condensation Synthesis Method. *Chem. Mater.* **2003**, *15*, 4247-4256.

(29) Su, D.; Li, Y.; Zhai, H.; Wang, B. Preparation of fireproofing single component dealcoholized silicone rubber sealant vulcanizable at room temperature. Application: CN Patent 2010-10265693 101942201.

(30) Chan, C. C. P.; Choudhury, N. R.; Majewski, P. Fabrication and characterisation of self-assembled monolayers of N-[3-(trimethoxysilyl)propyl]diethylenetriamine on silica particles. *Colloids Surf., A.* **2011**, *377*, 20-27.

(31) Mdoe, J. E. G. Preparation, characterization and application of polyamine-silica hybrids in the epoxidation of α,β-unsaturated olefins. *Bull. Chem. Soc. Ethiop.* **2002**, *16*, 103-112.

(32) SiSiB: *SiSiB PC1300 Silane*; Power Chemical Corporation Ltd. **2009**.

(33) Tripathi, I.; Kumar, M. M.; Arti, K.; Chinmayi, M.; Ruchita, T.; Kant, S. L.; Bihari, P. K. Synthesis, Characterization of some Antidiabetic Copper Complexes with Ethylenediamine. *Res. J. Chem. Sci.* **2013**, 12,54-59.

(34) Chauhan, B. P.; Rathore, J.; Sardar, R.; Tewari, P.; Latif, U. Synthesis, stabilization, and applications of nanoscopic siloxane–metal particle conjugates. *J. organomet. Chem.* **2003**, *686*, 24-31.

(35) Issa, B.; Obaidat, I. M.; Albiss, B. A.; Haik, Y. Magnetic nanoparticles: surface effects and properties related to biomedicine applications. *Int. J.Mol.Sci.* **2013**, *14*, 21266-21305.

(36) Marzke, R. Quantum Size Effects in Small Metallic Particles. *Cat. Rev. Sci. Eng.* **1979**, *19*, 43-65.

(37) Roduner, E. Size matters: why nanomaterials are different. *Chem. Soc. Rev.* **2006**, *35*, 583-592.

(38) Medina, C.; Santos-Martinez, M.; Radomski, A.; Corrigan, O.; Radomski, M. Nanoparticles: pharmacological and toxicological significance. *Br. J.Pharmacol.* **2007**, *150*, 552-558.

(39) Skumryev, V.; Stoyanov, S.; Zhang, Y.; Hadjipanayis, G.; Givord, D.; Nogués, J. Beating the superparamagnetic limit with exchange bias. *Nature,* **2003**, *423*, 850-853.

(40) Gleeson, O.; Tekoriute, R.; Gun'ko, Y. K.; Connon, S. J. The First Magnetic Nanoparticle-Supported Chiral DMAP Analogue: Highly Enantioselective Acylation and Excellent Recyclability. *Chem. Eur. J.* **2009**, *15*, 5669-5673.

(41) National Institute of Allergy and Infectious Diseases. http://www.niaid.nih.gov/topics/emerging/pages/introduction.aspx (accessed 8 April 2015).

(42) Images for DNA helix cartoon. http://imgkid.com/dna-helix-cartoon.shtml (accessed 08 April 2015).

(43) Liu, X.; Ma, Z.; Xing, J.; Liu, H. Preparation and characterization of amino–silane modified superparamagnetic silica nanospheres. *J. Magn. Mater.* **2004**, *270*, 1-6.

(44) Sahoo, S. K.; Panyam, J.; Prabha, S.; Labhasetwar, V. Residual polyvinyl alcohol associated with poly (D,L-lactide-co-glycolide) nanoparticles affects their physical properties and cellular uptake. *J. Controlled Release.* **2002**, *82*, 105-114.

(45) What is ferrofluid? Trippy microphotographs illustrate magnetic phenomenon. http://www.mnn.com/green-tech/research-innovations/blogs/what-is-ferrofluid-trippy-microphotographs-illustrate-magnetic (accessed 08 April 2015).

(46) Fierro, J. L. G.: *Metal Oxides: chemistry and applications*; CRC press, **2005**.

(47) Taglietti, A.; Arciola, C. R.; D'Agostino, A.; Dacarro, G.; Montanaro, L.; Campoccia, D.; Cucca, L.; Vercellino, M.; Poggi, A.; Pallavicini, P. Antibiofilm activity of a monolayer of silver nanoparticles anchored to an amino-silanized glass surface. *Biomaterials* **2014**, *35*, 1779-1788.

(48) Häfeli, U.: The mystery and history of magnetism. In *Scientific and clinical applications of magnetic carriers*; Springer. **1997**; pp 1-10.

(49) Cao, H.; He, J.; Deng, L.; Gao, X. Fabrication of cyclodextrin-functionalized superparamagnetic Fe_3O_4 amino-silane core–shell nanoparticles via layer-by-layer method. *Appl. Surf. Sci.* **2009**, *255*, 7974-7980.

(50) Meledandri, C. J.; Stolarczyk, J. K.; Ghosh, S.; Brougham, D. F. Nonaqueous magnetic nanoparticle suspensions with controlled particle size and nuclear magnetic resonance properties. *Langmuir* **2008**, *24*, 14159-14165.

(51) Wei, L.; Hervé, M.; Edouard, P. Use of different rapid mixing devices for controlling the properties of magnetite nanoparticles produced by precipitation. *J. Cryst. Growth.* **2012**, *342*, 21-27.

(52) Ma, M.; Zhang, Y.; Yu, W.; Shen, H.-y.; Zhang, H.-q.; Gu, N. Preparation and characterization of magnetite nanoparticles coated by amino silane. *Colloids Surf. A.* **2003**, *212*, 219-226.

(53) Thanh, N. T.; Green, L. A. Functionalisation of nanoparticles for biomedical applications. *Nano Today.* **2010**, *5*, 213-230.

(54) Li, J.; Zeng, H.; Sun, S.; Liu, J. P.; Wang, Z. L. Analyzing the structure of CoFe-Fe_3O_4 core-shell nanoparticles by electron imaging and diffraction. *J. Phys. Chem. B.* **2004**, *108*, 14005-14008.

(55) Massart, R. Preparation of aqueous magnetic liquids in alkaline and acidic media. *IEEE Trans. Magn.,* **1981**, *17*, 1247-1248.

(56) Sun, Y.-k.; Ma, M.; Zhang, Y.; Gu, N. Synthesis of nanometer-size maghemite particles from magnetite. *Colloid. Surfaces A.* **2004**, *245*, 15-19.

(57) Magnetite Ferric and Ferrous Oxides, Oxide Mineral Class. http://www.esci.umn.edu/courses/1001/minerals/magnetite.shtml (accessed 8 April 2015).

(58) Alpha Chemicals. http://alphachemicals.com/black_iron_oxide (accessed 08 April 2015).

(59) Trang, N. T.; Thuy, T. T.; Mott, D. M.; Koyano, M.; Maenosono, S. Attenuation of surface-enhanced Raman scattering of magnetic–plasmonic FePtAg core–shell nanoparticles due to an external magnetic field. *Chem. Phys. Lett.* **2013**, *574*, 94-99.

(60) Manceau, A.; Gorshkov, A. I.; Drits, V. A. Structural chemistry of Mn, Fe, Co, and Ni in manganese hydrous oxides; Part I, information from XANES spectroscopy. *Am. Min.* **1992**, *77*, 1133-1143.

(61) Goya, G.; Berquo, T.; Fonseca, F.; Morales, M. Static and dynamic magnetic properties of spherical magnetite nanoparticles. *J. Appl.Phys.* **2003**, *94*, 3520-3528.

(62) Sun, S.; Zeng, H. Size-controlled synthesis of magnetite nanoparticles. *J. Am. Chem. Soc.* **2002**, *124*, 8204-8205.

(63) Hitchhiker's Guide to Magnetism. http://www.irm.umn.edu/hg2m/hg2m_b/hg2m_b.html (accessed 9 April 2015).

(64) Fe_3O_4 gif. http://www.tdk.co.jp/techmag/ferrite/grain_3/Fe_3O_4fini.gif (accessed 09 April 2015).

(65) Pankhurst, Q. A.; Connolly, J.; Jones, S.; Dobson, J. Applications of magnetic nanoparticles in biomedicine. *J.Phys. D. Appl. Phys.* **2003**, *36*, R167.

(66) Kennedy, A. Radioembolization of hepatic tumors. *J. Gastrointest. Oncol.* **2014**, *5*, 178.

(67) He, Y.; Wang, S.; Li, C.; Miao, Y.; Wu, Z.; Zou, B. Synthesis and characterization of functionalized silica-coated Fe_3O_4 superparamagnetic nanocrystals for biological applications. *J. Phys. D: Appl. Phys.* **2005**, *38*, 1342.

(68) Chertok, B.; David, A. E.; Yang, V. C. Brain tumor targeting of magnetic nanoparticles for potential drug delivery: effect of administration route and magnetic field topography. *J. Controlled Rel.*. **2011**, *155*, 393-399.

(69) Janzer, R. C.; Raff, M. C. Astrocytes induce blood–brain barrier properties in endothelial cells. *Nature.* **1987**, *325*, 253-257.

(70) Sheikov, N.; McDannold, N.; Vykhodtseva, N.; Jolesz, F.; Hynynen, K. Cellular mechanisms of the blood-brain barrier opening induced by ultrasound in presence of microbubbles. *Ultrasound Med. Biol.* **2004**, *30*, 979-989.

(71) Cole, A. J.; David, A. E.; Wang, J.; Galbán, C. J.; Yang, V. C. Magnetic brain tumor targeting and biodistribution of long-circulating PEG-modified, cross-linked starch-coated iron oxide nanoparticles. *Biomaterials.* **2011**, *32*, 6291-6301.

(72) Chertok, B.; Moffat, B. A.; David, A. E.; Yu, F.; Bergemann, C.; Ross, B. D.; Yang, V. C. Iron oxide nanoparticles as a drug delivery vehicle for MRI monitored magnetic targeting of brain tumors. *Biomaterials.,* **2008**, *29*, 487-496.

(73) Xie, J.; Liu, G.; Eden, H. S.; Ai, H.; Chen, X. Surface-engineered magnetic nanoparticle platforms for cancer imaging and therapy. *Acc. Chem. Res.* **2011**, *44*, 883-892.

(74) Ninjbadgar, T.; Brougham, D. F. Epoxy ring opening phase transfer as a general route to water dispersible superparamagnetic Fe_3O_4 nanoparticles and their application as positive MRI contrast agents. *Adv. Funct. Mater.* **2011**, *21*, 4769-4775.

(75) Diseases and Conditions Infectious Diseases. http://www.mayoclinic.org/diseases-conditions/infectious-diseases/basics/causes/con-20033534 (accessed 7 April 2015).

(76) Healthline. http://www.healthline.com/health/strep-throat#Overview1 (accessed 7 April 2015).

(77) Dermatologist on Call Skin Hair and Nail Conditions. https://www.dermatologistoncall.com/conditions (accessed 7 April 2015).

(78) What Does Shingles Look Like? http://www.healthline.com/health-slideshow/shingles-pictures (accessed 7 April 2015).

(79) Your Doctor - Dermatology Atlas,. http://www.your-doctor.net/dermatology_atlas/rwx/rwx/Mucocutaneous_Leishmaniasis.jpg (accessed 7 April 2015).

(80) *Understanding Microbes in Sickness and in Health;* SERVICES, U. S. D. O. H. A. H., Health, N. I. o., NIH Publication, **2009**.

(81) Organization, W. H.: *The evolving threat of antimicrobial resistance: options for action*; World Health Organization, **2012**.

(82) McCullough, M.; Ross, B.; Reade, P. *Candida albicans*: a review of its history, taxonomy, epidemiology, virulence attributes, and methods of strain differentiation. *Int. J. Oral and Maxillofac. Surg.* **1996**, *25*, 136-144.

(83) Villar, C.; Kashleva, H.; Dongari-Bagtzoglou, A. Role of *Candida albicans* polymorphism in interactions with oral epithelial cells. *Oral Microbiol. Immun.* **2004**, *19*, 262-269.

(84) Biology Kaminiski Images. http://www.usask.ca/biology/kaminskyj/images/BachewichCandida.jpg (accessed 7 April 2015).

(85) Ruhnke, M. Skin and mucous membrane infections. *Candida and candidiasis.* ASM Press, Washington, DC. **2002**, 307-325.

(86) Tobudic, S.; Kratzer, C.; Lassnigg, A.; Presterl, E. Antifungal susceptibility of *Candida albicans* in biofilms. *Mycoses*. **2012**, *55*, 199-204.

(87) *Candida* Conquered Naturally. https://careman.wordpress.com/category/candida-2/ (accessed 8 April 2015).

(88) Ghannoum, M. A.; Rice, L. B. Antifungal agents: mode of action, mechanisms of resistance, and correlation of these mechanisms with bacterial resistance. *Clin. Microbiol. Rev.* **1999**, *12*, 501-517.

(89) de Irala-Estévez, J.; Martínez-Concha, D.; Díaz-Molina, C.; Masa-Calles, J.; del Castillo, A. S.; Navajas, R. F.-C. Comparison of different methodological approaches to identify risk factors of nosocomial infection in intensive care units. *J. Intensive Care Med.* **2001**, *27*, 1254-1262.

(90) Borgers, M. Mechanism of action of antifungal drugs, with special reference to the imidazole derivatives. *Rev. Infect. Dis.* **1980**, *2*, 520-534.

(91) Brajtburg, J.; Powderly, W. G.; Kobayashi, G. S.; Medoff, G. Amphotericin B: current understanding of mechanisms of action. *Antimicrob. Agents Chemother.* **1990**, *34*, 183.

(92) Albengres, E.; Le Louët, H.; Tillement, J.-P. Systemic antifungal agents. *Drug Saf.* **1998**, *18*, 83-97.

(93) Wood, A. J.; Como, J. A.; Dismukes, W. E. Oral azole drugs as systemic antifungal therapy. *N. Eng. J. Med.* **1994**, *330*, 263-272.

(94) Harrison, J. J.; Ceri, H.; Yerly, J.; Rabiei, M.; Hu, Y.; Martinuzzi, R.; Turner, R. J. Metal ions may suppress or enhance cellular differentiation in *Candida albicans* and *Candida tropicalis* biofilms. *Appl. Environ. Microbiol.* **2007**, *73*, 4940-4949.

(95) Harrison, J. J.; Rabiei, M.; Turner, R. J.; Badry, E. A.; Sproule, K. M.; Ceri, H. Metal resistance in *Candida* biofilms. *FEMS Microbiol. Ecol.* **2006**, *55*, 479-491.

(96) Coyle, B.; Kavanagh, K.; McCann, M.; Devereux, M.; Geraghty, M. Mode of anti-fungal activity of 1,10-phenanthroline and its Cu (II), Mn (II) and Ag (I) complexes. *Biometals.* **2003**, *16*, 321-329.

(97) McCann, M.; Geraghty, M.; Devereux, M.; O'Shea, D.; Mason, J.; O'Sullivan, L. Insights into the mode of action of the anti-*Candida* activity of 1,10-phenanthroline and its metal chelates. *Metal-Based Drugs.* **2000**, *7*, 185.

(98) Viles, J. H.; Cohen, F. E.; Prusiner, S. B.; Goodin, D. B.; Wright, P. E.; Dyson, H. J. Copper binding to the prion protein: structural implications of four identical cooperative binding sites. *PNAS.* **1999**, *96*, 2042-2047.

(99) Coyle, B.; Kinsella, P.; McCann, M.; Devereux, M.; O'Connor, R.; Clynes, M.; Kavanagh, K. Induction of apoptosis in yeast and mammalian cells by exposure to 1,10-phenanthroline metal complexes. *Toxicol. in Vitro.* **2004**, *18*, 63-70.

(100) MacLeod, R. A. The toxicity of o-phenanthroline for lactic acid bacteria. *J. Biol. Chem.* **1952**, *197*, 751-761.

(101) Devereux, M.; McCann, M.; O Shea, D.; Kelly, R.; Egan, D.; Deegan, C.; Kavanagh, K.; McKee, V.; Finn, G. S., Synthesis, antimicrobial activity and chemotherapeutic potential of inorganic derivatives of 2-(4-thiazolyl) benzimidazole{thiabendazole}: X-ray crystal structures of $[Cu(THZH)_2Cl].H_20.EtOH$ and $TBZH_2NO_3$(TBZH=thiabendazole). *J. Inorg. Biochem.* **2004**, *98*, 1023-1031.

(102) Stellman, J. M.: *Encyclopaedia of Occupational Health and Safety: Chemical, industries and occupations*; 4th ed.; International Labour Office, **1998**; Vol. 3.

(103) Cotton, F. A.; Wilkinson, G.; Bochmann, M.; Murillo, C.: *Advanced Inorganic Chemistry*; 5th ed., **1998**.

(104) Hart, E.; Steenbock, H.; Waddell, J.; Elvehjem, C. Iron in nutrition VII. Copper as a supplement to iron for hemoglobin building in the rat. *J. Biol. Chem.* **1928**, *77*, 797-833.

(105) Corradi, M.; Mutti, A. Metal ions affecting the pulmonary and cardiovascular systems. *Met. Ions Life Sci.* **2011**, *8*, 81-105.

(106) Blower, P. J.; Lewis, J. S.; Zweit, J. Copper radionuclides and radiopharmaceuticals in nuclear medicine. *Nucl. Med. Biol.* **1996**, *23*, 957-980.

(107) Shorrocks, V. M. *Copper and the Human Health: A Review;* Copper Development Assosciation, **1992**.

(108) Borkow, G.; Gabbay, J.; Zatcoff, R. C. Could chronic wounds not heal due to too low local copper levels? *Med. Hypotheses.* **2008**, *70*, 610-613.

(109) Linder, M. C.; Hazegh-Azam, M. Copper biochemistry and molecular biology. *Am. J. Clin. Nutr.* **1996**, *63*, 797S-811S.

(110) Unleashing the Healing Energy of Nature with Beautiful and Elegant Jewelry,. http://www.healingcrystaljewelry.ca/search?term=bracelets (accessed 8 April 2015).

(111) Body and Soul Weleda Skincare Anthroposophic Medicines. http://www.worldwideshoppingmall.co.uk/body-soul/copper-ointment.asp (accessed 8 April 2015).

(112) Borkow, G.; Gabbay, J. Copper, An Ancient Remedy Returning to Fight Microbial, Fungal and Viral Infections. *Curr. Chem. Biol.* **2009**, *3*, 272-278.

(113) The power of copper. http://www.copperandhealth.com/the-power-of-copper/ (accessed 8 May 2015).

(114) Medical Uses of Copper in Antiquity, Copper Applications in Health & Environment. http://www.copper.org/publications/newsletters/innovations/2000/06/medicine-chest.html (accessed 8 May 2015).

(115) Gabbay, J.; Borkow, G.; Mishal, J.; Magen, E.; Zatcoff, R.; Shemer-Avni, Y. Copper oxide impregnated textiles with potent biocidal activities. *J. Ind. Text.* **2006**, *35*, 323-335.

(116) Yadav, A. K.; Kumar, R.; Saikia, R.; Bora, T. C.; Arora, D. K. Novel copper resistant and antimicrobial Streptomyces isolated from Bay of Bengal, India. *J. Med. Mycol.* **2009**, *19*, 234-240.

(117) Sorenson, J. R. J. Anti-inflammatory and anti-ulcer compounds. Application: US Patent 1978-910421 4221785.

(118) Maurer, G. L. Methods and compositions for treating inflammation or arthritis. Application: CA Patent 1983-440749 1218600.

(119) Weder, J. E.; Dillon, C. T.; Hambley, T. W.; Kennedy, B. J.; Lay, P. A.; Biffin, J. R.; Regtop, H. L.; Davies, N. M. Copper complexes of non-steroidal anti-inflammatory drugs: an opportunity yet to be realized. *Coord. Chem. Rev.* **2002**, *232*, 95-126.

(120) KOPERTOX®. http://datasheets.scbt.com/sc-360868_mfr.pdf (accessed 8 May 2015).

(121) Methods to prevent copper deficiency in cattle. http://www.vetmed.ucdavis.edu/vetext/local-assets/pdfs/pdfs_beef/cca0710-copper-defic.pdf (accessed 8 May 2015).

(122) Jurij J. Hostynek: Copper and the Skin. In *DERMCUSAL ®*; Howard I. Maibach, Ed.; Informa Healthcare, USA, Inc., 270 Madison Avenue, New York, NY 10016., **2006**; pp 200.

(123) Ibrahim, M.; Wang, F.; Lou, M. M.; Xie, G. L.; Li, B.; Bo, Z.; Zhang, G. Q.; Liu, H.; Wareth, A. Copper as an antibacterial agent for human pathogenic multidrug resistant Burkholderia cepacia complex bacteria. *J. Biosci. Bioeng.* **2011**, *112*, 570-576.

(124) Espirito Santo, C.; Taudte, N.; Nies, D. H.; Grass, G. Contribution of copper ion resistance to survival of Escherichia coli on metallic copper surfaces. *Appl. Environ. Microbiol.* **2008**, *74*, 977-986.

(125) Uriu-Adams, J. Y.; Keen, C. L. Copper, oxidative stress, and human health. *Mol. Aspects Med.* **2005**, *26*, 268-298.

(126) Crisponi, G.; Nurchi, V. M.; Fanni, D.; Gerosa, C.; Nemolato, S.; Faa, G. Copper-related diseases: From chemistry to molecular pathology. *Coord. Chem. Rev.* **2010**, *254*, 876-889.

(127) Cooper, G. J. Therapeutic potential of copper chelation with triethylenetetramine in managing diabetes mellitus and Alzheimer's disease. *Drugs* **2011**, *71*, 1281-1320.

(128) Brewer, G. J. Copper in medicine. *Curr. Opin. Chem. Biol.* **2003**, *7*, 207-212.

(129) Owens, P. E. Synthesis, Physical Characterisation and Antifungal Activity of Silver(I)- and Copper(II)-Containing Silicones. PhD Thesis, Maynooth University, **2013**.

(130) Lelis, M. d. F. F.; Fabris, J. D.; Mussel, W. d. N.; Takeuchi, A. Y. Preparation and characterization of Nickel-and cobalt-doped magnetites. *Mater. Res.* **2003**, *6*, 145-150.

(131) Iwasaki, T. Mechanochemical Synthesis of Magnetite/Hydroxyapatite Nanocomposites for Hyperthermia. *Mater. Sci.* **2013**, 175-194.

(132) Mahdavi, M.; Ahmad, M. B.; Haron, M. J.; Namvar, F.; Nadi, B.; Rahman, M. Z. A.; Amin, J. Synthesis, surface modification and characterisation of biocompatible magnetic iron oxide nanoparticles for biomedical applications. *Molecules*. **2013**, *18*, 7533-7548.

(133) Shen, L.; Laibinis, P. E.; Hatton, T. A. Bilayer surfactant stabilized magnetic fluids: synthesis and interactions at interfaces. *Langmuir* **1999**, *15*, 447-453.

(134) Nanocomposix, E.: 20 nm Magnetite Nanoparticles. **2015**.

(135) Chojnowski, J.; Fortuniak, W.; Rościszewski, P.; Werel, W.; Łukasiak, J.; Kamysz, W.; Hałasa, R. Polysilsesquioxanes and oligosilsesquioxanes substituted by alkylammonium salts as antibacterial biocides. *J. Inorg. Organomet. Polym. Mater.* **2006**, *16*, 219-230.

(136) Zhang, Z.; Liang, G.; Lu, T. Synthesis and characterization of cage octa (aminopropylsilsesquioxane). *J. Appl. Polymer Sc.* **2007**, *103*, 2608-2614.

(137) Singh, U. G.; Williams, R. T.; Hallam, K. R.; Allen, G. C. Exploring the distribution of copper–Schiff base complex covalently anchored onto the surface of mesoporous MCM 41 silica. *J. Solid State Chem.* **2005**, *178*, 3405-3413.

(138) Mdoe, J. Preparation, characterisation and application of polyamine-silica hybrids in the epoxidation of α,β-unsaturated olefins. *Bull. Chem. Soc. Ethiop.* **2002**, *16*, 103-112.

(139) Salon, M.-C. B.; Bayle, P.-A.; Abdelmouleh, M.; Boufi, S.; Belgacem, M. N. Kinetics of hydrolysis and self condensation reactions of silanes by NMR spectroscopy. *Colloids and Surf. A.* **2008**, *312*, 83-91.

(140) Cotton, F. A.; Wilkinson, G.; Murillo, C. A.; Bochmann, M.; Grimes, R.: *Advanced Inorganic Chemistry*; Wiley New York, **1999**; Vol. 5.

(141) Deacon, G.; Phillips, R. Relationships between the carbon-oxygen stretching frequencies of carboxylato complexes and the type of carboxylate coordination. *Coordination Chemistry Reviews* **1980**, *33*, 227-250.

(142) Elin, R. J.; Wolff, S. M. Effect of pH and iron concentration on growth of Candida albicans in human serum. *J. Infect. Dis.* **1973**, *127*, 705-708.

(143) McCann, M.; Coyle, B.; McKay, S.; McCormack, P.; Kavanagh, K.; Devereux, M.; McKee, V.; Kinsella, P.; O'Connor, R.; Clynes, M. Synthesis and X-ray crystal structure of [Ag (phendio)$_2$]ClO_4 (phendio=1,10-phenanthroline-5,6-dione) and its effects on fungal and mammalian cells. *Biometals* **2004**, *17*, 635-645.